Buckling at the Fluid - Soft Solid Interface;

A Means for Advanced Functionality within Soft Materials

Behrouz Tavakol

Dissertation submitted to the Faculty of the
Virginia Polytechnic Institute and State University
in partial fulfillment of the requirements for the degree of

Doctor of Philosophy
in
Engineering Mechanics

Douglas P. Holmes, Chair
Sunghwan Jung
Masoud Agah
Rafael Davalos
Mark A. Stremler
Howard A. Stone

August 4th, 2015
Blacksburg, Virginia

Keywords: Soft Materials, Fluid-Soft Solid Interface, Buckling, Snapping, Thin Plates

Buckling at the Fluid - Soft Solid Interface;

A Means for Advanced Functionality within Soft Materials

Behrouz Tavakol

(ABSTRACT)

Soft materials and compliant structures often undergo significant deformation without failure, a unique feature making them distinct from classical rigid materials. These substantial deformations provide a means for faster or more energy efficient deformations, which can be achieved by taking advantage of elastic instabilities. We intend to utilize structural instabilities to generate advanced functionality within soft materials. In particular, we use the buckling of thin, flexible plates to control or enhance the flow of fluid in a micro channel. The buckling deformation is created or altered via two different stimuli, first a mechanical strain and then an electrical signal. We investigate the behavior of each system under different conditions experimentally, numerically, or theoretically. We also show that the coupled interaction between fluid and the soft film plays a critical role in the shape of deformation and consequently in the functionality of the mechanism.

We first embed a buckled thin film in a fluid channel within a soft device. By applying a mechanical strain to the device, we show both experimentally and numerically that the height of the buckled film changes accordingly as does the flow rate. We then offer an analytical solution by extending the classical lubrication theory to higher-order terms as a means to more accurately describe the flow in a channel with a buckled thin film, and in general, the flow in channels with any constrictions provided the Reynolds number is low.

Next, we use an electrical signal to make a confined dielectric film undergo out-of-plane buckling deformation. The thin film is sandwiched between two flexible electrodes and the mechanism is implemented in a microfluidic device to pump the fluid into a micro channel. We show that the critical buckling voltage at which the thin film buckles out of the plane is mainly a function of voltage while the shape of deformation and so the functionality of this mechanism depend considerably on the applied boundary conditions. Finally, we enhance the fluid-soft structure response of the actuating mechanism by substituting flexible electrodes with fluid electrodes, resulting in a significant increase in the actuation frequency as well as a reduction in the critical buckling voltage.

... to my dad, who sacrificed his life for my success ...

... to my mom, who has spent her life for my comfort ...

... to my wife, who has encouraged me to be my best ...

... to my little daughter, who makes me laugh whenever she gets a chance ...

Acknowledgments

Writing this section was one of the most difficult parts of my dissertation. It is definitely challenging to truly thank all of my supporters but the best I can do is to briefly describe how much I owe my mentors, family, and friends.

I would like to first and foremost thank my PhD advisor and my mentor, Dr. Douglas P. Holmes, for his continuous support, guidance, motivation, and encouragement during every moment of my PhD program. Research has always lots of ups and downs and Doug has been a perfect mentor during these turbulences. I received a lot of encouragements when everything was going smoothly and I knew I was not left alone when everything was up in the air. Beyond being a unique advisor, Doug has also been a great friend who provided me with a lot of moral support, advice, and trust. I wish him the best in his future endeavors.

I would also like to sincerely thank my PhD committee members, Dr. Howard A. Stone, Dr. Sunghwan Jung, Dr. Rafael Davalos, Dr. Mark A. Stremler, and Dr. Masoud Agah for their outstanding technical and moral support during my PhD program. I am very lucky to have such a supportive, knowledgeable, kind, and collaborative committee. In particular, it was an honor for me to have a close collaboration with Dr. Howard Stone and to receive a lot of constructive suggestions and advice from him, resulting in three publications and several conference proceedings. He has been and will be my role model in academia. I also like to appreciate Dr. Sunny Jung for his extraordinary technical and lab support. Whenever we needed an equipment or a lab supply, the first thing we had in mind was to stop by his office or his lab and check whether they have it; If so, the rest was easy. His office door was also always open for any questions we had. The same thanks goes to Dr. Rafael Davalos for his phenomenal support on the lab supply and technical advice. I spend a couple of months in his lab to run a part of my experiments. We have also had long term, ongoing collaborations on several projects. I am very thankful to Dr. Mark Stremler for his kind support from the first day of my PhD program. I very well remember that he supported me for changing my program to Engineering Mechanics, and later for the NASA-VSGC and the Liviu Librescu Memorial Fellowships. I would also like to thank Dr. Masoud Agah for his spiritual and technical support. I could not imagine how our initial perspective student/advisory relation changed to a very close friendship.

I am also very thankful to Dr. James Hanna (VT), Dr. Norman Dowling (VT), Dr. Jake Socha (VT), Dr. Katia Bertoldi (Harvard), Dr. Pedro Reis (MIT), and Dr. Ilhan Aksay (Princeton) for variety of moral, technical, and financial support. A special thanks also goes to Mohammad Amin Ali Bakhshi of Boston University and Mohammad Bonakdar of Virginia Tech for their great advice and help on the micro fabrication processes.

I also like to acknowledge my colleagues, Dr. Michael Bozlar (Princeton), Ahmad Mojdehi (VT), Wes Royston (VT), Sarah Beauchamp (VT), Brendan Ondra (VT), Matthew Libuit (VT), John Hochgraf (VT), and Erin Chang (BU) for great collaborations, resulting in several conferences and publications. I also like to thank my former and current lab mates, in particular Anupam Pandey (VT), Trey Moore (VT), Callan Gillespie (VT), Matteo Pezzulla (Sapienza Roma), and Xin Jiang (BU) who made a lot of fun and joyful moments. I also thank my friends, especially Ehsan Rashedi, Dr. Saied Dehghani, Dr. Hodjat Pendar, Dr. Alireza Karimi, Dr. Arash Bahrami, Ali Nematpoor, and many others for making valuable friendship. I would also like to acknowledge all the staffs of former Engineering Science and Mechanics department, in particular, Lisa Smith, Melissa Nipper, Norma Guynn, Paul Siburt, Danny Reed, and Mac McCord for providing exceptional help with all paperwork in a friendly environment.

Finally, I would like to sincerely thank my family; my late father who always inspired me with his perseverance, my mother who has always endorsed me with her kindness, my brother and sister who have always made me laugh, and last but not least, my wife, Hoda, who has been my classmate, lab mate, and soul mate in the past ten years.

Thank you all!

Contents

List of Figures

Chapter 1

Introduction

1.1 Instability and Functionality

Mechanicians, mathematicians, architects, and engineers have a long history of familiarity with the buckling of structures. Public safety and structural integrity may be compromised if a mechanical structure undergoes a buckling instability, therefore, it is believed that the occurrence of an instability will only serve to interrupt the functionality of the system. This is generally true for rigid or stiff materials, where a buckled system often experiences large, irreversible or plastic deformation. This is, however, not true for compliant or soft systems, which can undergo large, reversible deformations without failure.

In this work, the main focus will be on first exposing a soft material or system to conditions that cause buckling instabilities, and then using such instabilities for advanced functionality. We use different stimuli to bring a system to an instable condition and then provide examples to demonstrate potential applications. A model will be offered for each type of actuation and the results will be compared with experimental and simulation results. In particular, an extension to lubrication theory will be offered to estimate the pressure drop within a channel with a significant change in geometry, e.g. a channel with a buckled arch on one side. We also show that buckling instability can be used to enhance the nearby flow and pump fluid into a microchannel.

1.2 Buckling

We describe the buckling instability phenomenon first via a simple buckling example. We consider a vertical beam or column that is pinned from both ends. The bottom of the beam cannot move while the top end moves only in the vertical direction (Figure 1.1a). The beam remains straight and deforms only in the axial direction under a compressive axial load, P, that is less than a *critical load* [1]. The beam is thus in a *stable* state until the load reaches the critical value at which a small increase in the axial loading causes a noticeable lateral deformation (Figure 1.1b) [2–4]. This *instable* condition is referred to as bifurcation buckling [4], meaning that the mathematical solution bifurcates and the deformation can occur on either sides of the lateral direction (Figure 1.1b). We note that snap-through buckling is another type of buckling in which the geometry undergoes a rapid deformation directly from one stable state to another one [5, 6]. To estimate the critical load for a bifurcation buckling, we first write the governing differential equation for the vertical beam [2]:

$$E\,I\frac{d^2w}{dy^2} + Pw = 0, \tag{1.1}$$

where E is the elastic modulus, I is the moment of inertia, P is the compressive load, and w is the lateral deformation. The first term of the governing equation stabilizes the system while the second term moves the system away from stability when load is compressive (positive in the provided coordinates). The general solution for the homogeneous, linear differential equation of (1.1) takes the form of $w = A\sin\left(\sqrt{P/EI}x\right) + B\cos\left(\sqrt{P/EI}x\right)$ where A and B are constant coefficients determined by boundary conditions. Considering pinned conditions at both ends, we find that $B = 0$ and $A\sin\left(\sqrt{P/EI}\,L\right) = 0$. Since A cannot be zero, $\sin\left(\sqrt{P/EI}\,L\right) = 0$ or equivalently [3]:

$$P_{cr} = n^2\pi^2\,\frac{EI}{L^2} \tag{1.2}$$

where L is the length of the beam and $n = 1, 2, 3, ...$ corresponds to different buckling modes (Figure 1.1a).

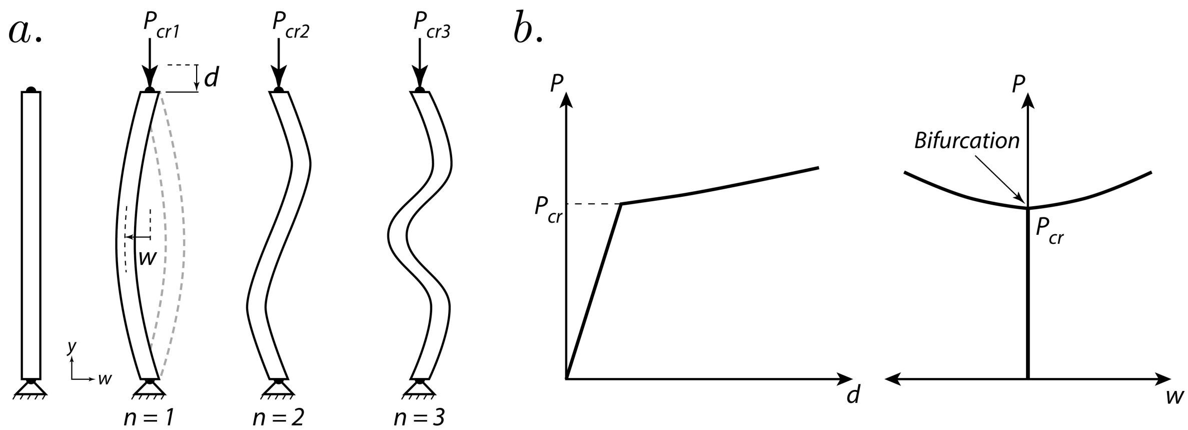

Figure 1.1: *a.* Schematics of buckling of a pinned column under a compressive load. Based on different conditions and parameters, a column or beam may experience different modes of buckling (n). *b.* axial (d) and lateral (w) deflections of a beam under comprehensive loading. Large deformations are associated with loads that exceed P_{cr}.

When the compressive load exceeds the critical buckling load, large post-buckling deformations may lead to a failure in stiff structures while more compliant structures may withstand large deformations. We therefore intend to utilize the large buckling deformations within soft structures towards advanced functionality.

Plates and shells tend to buckle similarly under compressive loading although the buckling modes might be different in each direction. We consider a circular plate that is hinged at its circular edge 1.2a. The plate undergoes buckling if the in-plane compressive loading exceeds the critical buckling load [7]. Since the plate is treated as a surface, *i.e.* a 2D geometry, we have a pair of buckling modes, each is associated with one direction (Figure 1.2). For example, the plate may undergo (1,2) buckling modes, *i.e.* the first buckling mode in the radial direction and the second buckling mode in the circumferential direction. Here we focus on the buckling deformation of circular plates as the actuators we use in this study are circular. To estimate the critical buckling loads and the associated buckling modes, we start with the general governing differential equation of equilibrium for a circular plate in the cylindrical coordinates [3, 7, 8]:

$$\left(\frac{\partial^2}{\partial r^2}+\frac{1}{r}\frac{\partial}{\partial r}+\frac{1}{r^2}\frac{\partial^2}{\partial \theta^2}\right)\left(\frac{\partial^2}{\partial r^2}+\frac{1}{r}\frac{\partial}{\partial r}+\frac{1}{r^2}\frac{\partial^2}{\partial \theta^2}+\frac{N_r}{D}\right)w(r,\theta)=0, \tag{1.3}$$

where w is the out-of-plane deflection, N_r is the radial compressive load per unit length,

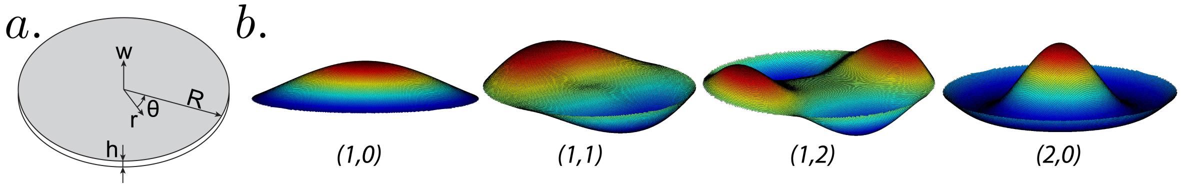

Figure 1.2: *a.* A schematic of a thin, circular plate that is flat before buckling. *b.* Different buckling modes of the circular plate. The (n_r, n_θ) pair corresponds respectively to the number of circumferential lines and the number of diametrical lines with zero displacement.

$D = \frac{E\,h^3}{12(1-\nu^2)}$ is the flexural rigidity of the plate, E is the elastic modulus, ν is the Poisson's ratio, and h is the plate thickness. If we look for the axisymmetric modes, *e.g.* the pair of (1,0) in Figure 1.2b, all derivatives with respect to θ are zero and Equation (1.3) reduces to:

$$\frac{d^2\phi}{dr^2} + \frac{1}{r}\frac{d\phi}{dr} + \left(\frac{N_r}{D} - \frac{1}{r^2}\right)\phi = 0, \tag{1.4}$$

where $\phi = \frac{dw}{dr}$ [3, 7]. Multiplied by r^2, the above equation becomes a Bessel's differential equation and the general solution will be $w(r) = A\,J_p(r) + B\,Y_p(r)$, where A and B are constant coefficients, and J_p and Y_p are Bessel functions of the first and the second kind of order p, respectively. Similar to the previous buckling example, we then apply boundary conditions and the only non-trivial solution is when $J_0(R) = 0$. As a result,

$$(\sigma_r)_{cr} = \frac{4.2D}{R^2h}, \tag{1.5}$$

where R is the plate radius and $(\sigma_r)_{cr}$ is the critical compressive stress in the radial direction [7]. If we are however interested in non-symmetrical modes, we must use Equation (1.3). By assuming $w = \sum_{n=1}^{\infty} A_n(r) sin\, n\theta$ and substituting it into Equation (1.3), we find an expression for $w(r,\theta)$, which can then be substituted into two equations satisfying the boundary conditions [3]. As we look for a nontrivial solution, the determinant of the coefficients of the two linear, homogeneous equations should vanish [1], proving that a buckled mode exists. By setting $n = 1$ to obtain the critical radial stress for the first asymmetric mode [3], *i.e.* the buckling mode of (1,1) where half of the plate deforms upward and the other half deforms downward, we have:

$$(\sigma_r)_{cr} = \frac{13.2D}{R^2h}. \tag{1.6}$$

A similar approach can be used to obtain critical buckling loads for other boundary conditions, which in general take the form of $(\sigma_r)_{cr} = k\, D/R^2\, h$, where k is a coefficient determined by the type of boundary conditions. We note that unless experiments are conducted under vacuum, the surrounding media play a critical role in the buckling shape of thin plates, which will be discussed in detail in chapter 4.

1.3 Fluid Flow

Fluids that are being used in this study are Newtonian fluids, *i.e.* shear stresses due to the flow are linearly proportional to the strain rate [9]. We also assume that these fluids are isotropic and incompressible, *i.e.* fluid properties are independent of directions, and the volume change due to applied pressure is negligible [9]. To describe the fluid flow within a channel, we start with the continuity and Navier-Stokes equations for an incompressible Newtonian fluid [10]:

$$\nabla \cdot \mathbf{u} = 0 \tag{1.7a}$$

$$\rho \left(\frac{\partial \mathbf{u}}{\partial t} + \mathbf{u} \cdot \nabla \mathbf{u} \right) = -\nabla p + \mu \nabla^2 \mathbf{u} + \rho\, \mathbf{g}, \tag{1.7b}$$

where ρ is the fluid density, $\mathbf{u} = (u, v)$ is the velocity field, p is the applied pressure, μ is the fluid viscosity, and $\rho\, \mathbf{g}$ represents body forces. By assuming a steady-state flow and neglecting the body forces, the first and the last terms of Equation (1.7b) vanish. We then choose dimensionless variables $X = x/L$, $Y = y/L$, $U = uL/q$, $V = vL/q$, and $P = pL^2/\mu q$ to nondimensionalize the above equations:

$$\frac{\partial U}{\partial X} + \frac{\partial V}{\partial Y} = 0 \tag{1.8a}$$

$$\mathcal{R}e \left(U \frac{\partial U}{\partial X} + V \frac{\partial U}{\partial Y} \right) = -\frac{\partial P}{\partial X} + \frac{\partial^2 U}{\partial X^2} + \frac{\partial^2 U}{\partial Y^2} \tag{1.8b}$$

$$\mathcal{R}e \left(U \frac{\partial V}{\partial X} + V \frac{\partial V}{\partial Y} \right) = -\frac{\partial P}{\partial Y} + \frac{\partial^2 V}{\partial X^2} + \frac{\partial^2 V}{\partial Y^2}, \tag{1.8c}$$

where L is a characteristic length, q is the flow rate per unit length, and $\mathcal{R}e = \rho\, q / \mu$ is the dimensionless Reynolds number, expressing the ratio of the inertia convective force to the viscous force.

For small Reynolds numbers, where the viscous forces are dominant, we neglect the left sides of Equations (1.8b) and (1.8c). Going back to the dimensional variables, we find that the flow is governed by the Stokes equation [10, 11]:

$$\mu \nabla^2 \mathbf{u} = \nabla p. \tag{1.9}$$

The linearity of the above governing equations enables us to obtain analytical solutions by a variety of methods, *e.g.* perturbation expansion [12–14], and study the physical structure of the flow.

1.4 Outline

This dissertation contains 4 major studies, each will be discussed in one chapter in detail and the associated literature review will be presented in the beginning of that chapter.

- **Chapter 2:** fluid flow within a micro channel is going to be controlled via the buckling deformation of an arch that is embedded into the channel. With no external forces, the arch is fully buckled, and therefore the flow is zero. We then use mechanical stimulus, such as stretching or bending the device, to reduce the buckling deformation and thus increase the flow rate. We provide a model to describe the buckling deformation of the flexible arch as a function of externally applied strain. We then develop a second model to analytically describe the flow within the channel as a function of buckling deformation that was estimated from the first model. Since the derivation of the second model is long and also the model can be used for variety of applications, we present the detailed derivation in next chapter while we compare the analytical solutions to the experimental and simulation results of the buckled arch in this chapter. Finally, we show that these flexible arches can be used in series/parallel for further functionality, e.g. for directing fluid flow toward region of high stress.

- **Chapter 3:** we develop an extension to lubrication theory by considering higher-order terms of the analytical approximation to describe the fluid flow within a channel that has a constriction or convexity. We show that this approach can be used for any channel with a constriction on the order of the channel height as long as the constriction geometry is known and piece-wise differentiable. This is also true for a channel with a convex shape. Experimental results qualitatively confirm the higher-order analytical solutions. We also perform non-dimensional numerical analyses and obtain the deviation of different orders of the analytical solutions from the simulation results, providing a threshold for considering higher-order terms in the solution.

- **Chapter 4:** We look for the use of buckling instability of thin plates for pumping fluids within micochannels. The plate consists of a dielectric film that is sandwiched between two flexible, solid electrodes. Not only are these electrodes compatible with fluids, they also undergo large deformation without failure. Unlike the first study in which the buckling deformation is altered via mechanical stimulus, we use an electrical signal to bring this system to a buckling instability condition. We determine the onset of these voltage-induced buckling instabilities, and present a model to estimate the critical buckling voltage. We also measure the flow generated by these pumps as a function of voltage for different boundary conditions. Finally, by coupling/combining these pumps in series and parallel, we provide a means for further functionalities, such as bidirectional or vacuum pumps with enhanced flow rates.

- **Chapter 5:** Flexible, solid electrodes provide a robust tool for making high-flow pumps that are embeddable into a microfluidic device and compatible with variety of applications; however, the thickness of electrodes and therefore the total thickness of the actuating plate cannot significantly be reduced; resulting in two limitations. First, the actuating plate is not embeddable directly into a micro channel. Second, the buckling deformation occurs at relatively low frequencies, making it physically infeasible to be used for high speed applications. In this chapter, We address the two limitations by introducing fluidic electrodes, which have outstanding features. First, microfabrication of a micro actuator with fluid electrodes is much easier and faster than the one with flexible electrodes. In addition, the thickness of actuating plate can be reduced to the limit of the dielectric film thickness, enabling the plate to undergo the buckling deformation at lower voltages and much higher frequencies. Experimental results show that these micro actuators are capable of buckling at high frequencies. We characterize the interaction between the film and the fluid by obtaining the buckling shape of the micro actuator and by measuring the volume of fluid disturbed by the film deformation.

References

[1] R. M. Rivello. *Theory and analysis of flight structures*. McGraw-Hill College, 1969.

[2] S. P. Timoshenko and J. M. Gere. *Theory of elastic stability*. McGraw-Hill Book Company Inc., New York, 1961.

[3] P. S. Bulson. *The stability of flat plates*. Elsevier Publishing Company, 1969.

[4] S. S. Antman. *Nonlinear problems of elasticity, volume 107 of Applied Mathematical Sciences*. Springer, New York, 2005.

[5] N. Akkas. "Bifurcation and snap-through phenomena in asymmetric dynamic analysis of shallow spherical shells". In: *Computers & Structures* 6.3 (1976), pp. 241–251.

[6] C. E. Riley. "Elastic buckling loads of slender columns with variable cross section by the newmark method". MA thesis. Colorado State University, 2003.

[7] S. Timoshenko, S. Woinowsky-Krieger, and S. Woinowsky-Krieger. *Theory of plates and shells*. Vol. 2. McGraw-hill New York, 1959.

[8] E. Yamaguchi and W. Chen. "Basic theory of plates and elastic stability". In: *Structural Engineering Handbook, Boca Raton, CRC Press LLC* (1999).

[9] F. White. *Fluid mechanics*. McGraw-Hill Higher Education, 2015.

[10] C. Pozrikidis. *Introduction to theoretical and computational fluid dynamics, 2nd Edition*. Oxford University Press, 2011.

[11] P. Kundu and I. Cohen. *Fluid Mechanics, 4th Edition*. Elsevier Academic Press, 2008.

[12] A. H. Nayfeh. *Perturbation methods*. John Wiley & Sons, 2008.

[13] J. Kevorkian and J. D. Cole. *Perturbation methods in applied mathematics*. Vol. 34. Springer Science & Business Media, 2013.

[14] E. J. Hinch. *Perturbation methods*. Cambridge university press, 1991.

Chapter 2

Buckling Instability as a Means to Control Fluid Flow

This work has been published in *Soft Matter*. Here it is reproduced by permission of The Royal Society of Chemistry.

2.1 Abstract

In this chapter, we demonstrate how to utilize buckling instability of a flexible arch to control the fluid within a channel. This buckling deformation is caused via mechanical stimulus applied to a soft device or system. To better elaborate this idea, we make a soft device with a channel that has a buckled arch on one side. Upon applying a proper mechanical loading, e.g. stretching or bending, the buckling deformation is reduced, and consequently, the flow increases. After releasing the load, the device comes back to its initial conditions and so does the flow. We present an analytical approach to estimate the flow as a function of applied strain (the analytical solution will be derived in detail in the next chapter). We also perform experiments and simulations to support our analytical approach. We then combine these flexible valves to expand the use of buckling instabilities in directing the flow toward regions of externally applied mechanical stress. The simplicity of this approach enables a general design for advanced functionality.

2.2 Introduction

As variety of biological systems use flexible tubes and vessels to carry blood and other biofluids, there should be superior advantages of soft tubes over rigid channels in such environments. The interactions between the internal flow, external system pressure, and tube deformation, though nonlinear, often play a significant role in flow regulation within those tubes [1, 2]. For example, as a giraffe changes its posture from standing and moves the head down for drinking water, a pressure-regulated collapse of its jugular vein reduces the blood flow to the head to maintain the brain's blood pressure within normal ranges [2, 3]. In addition, flow in the majority of fluidic systems is from high stress toward low stress regions, causing the fluid moving away from the external force. There exist, however, some cases where the fluid moves toward regions of external high stress, as observed in bones' porosity in which mechanical strains induce mechanotransduction for rheotaxis [4–6].

We make a device with internal flexible valves that can control and direct fluid flow via external mechanical actuation for advanced functionalities, e.g. *in situ* mixing, chemical reactions, and rapid, portable chemical analysis. In particular, we fabricate internal flexible valves so that macroscopic deformation leads to valve function that regulates fluid flow and so can direct flow from low to high regions of external stress. Creating a bio-inspired method for internal flow regulation will be useful for controlling fluid flow within multifunctional devices[7] and these fluid networks can approach the complexity found in integrated circuits [8–10]. Fluid can be transported actively using variety of methods, e.g. external mechanical pumps and electrical signals [11, 12], or passively via surface tension [13] and swelling [14, 15]. While significant advances in controlling fluid flow continue to be made using externally actuated valves, the presence of external power and hardware limit a device's range of use [16]. The development of a fully internally controlled device will enable portable or embeddable devices for controlling and manipulating flow, for example, within self-healing and self-strengthening materials.

2.3 Design of Experiment

2.3.1 Approach

Here we utilize elastic deformations within a flexible device, driven by mechanical actuation, to control and direct fluid flow internal to a soft material. In particular, a fluid confined to one compartment of a channel will flow through a channel when a pressure drop is created by stretching or bending the material (Figure 2.1). The basis of our approach is a flexible arch within a milli- or microfluidic channel, which is designed to prevent fluid flow in its initial, strain-free state. Upon deforming the device, the arch's curvature decreases and acts like a valve allowing fluid to flow. The design represents a fluid-control analogue to the use of a buckled conducting wire in the design of flexible electronic devices.[17, 18] We use a mathematical model based on the buckling of an Euler column to predict the deformation of the arch and a perturbation analysis based upon lubrication theory to predict the corresponding flow rate within the channel for varying degrees of arch deformation. By extending this design to include multiple arches within a channel, we illustrate how local material deformations will cause fluid flow towards a region of high applied stress, which, with appropriate choice of liquids, can serve as the basis for self-healing and active-sensing materials, as well as metamaterials capable of exhibiting "negative" poroelastic fluid flow.

2.3.2 Fabrication

The device consists of three parts: substrate, superstrate, and a thin film in between (Figure 2.1); each was fabricated with polydimethylsiloxane (PDMS) (Dow Corning Sylgard 184^{TM}) mixed at a 20:1 ratio of prepolymer to crosslinker, and degassed in a vacuum chamber. This mixture was then molded against a glass template of a channel to form the substrate and superstrate while the thin film was prepared by spin-coating PDMS on a petri dish, with the spin speed and time varied to control film thickness ($h = \mathcal{O}(50\ \mu m)$). The three parts were thermally cured in an oven at 100°C for 45 minutes.

The substrate, with a channel of length $L_0 = \mathcal{O}(1mm)$, was clamped at its edges and uniaxially stretched by length $\Delta L = \mathcal{O}(100\mu m)$ in the direction orthogonal to the channel, and the thin film was bonded to it using oxygen plasma treatment (Electro-Technic BD-

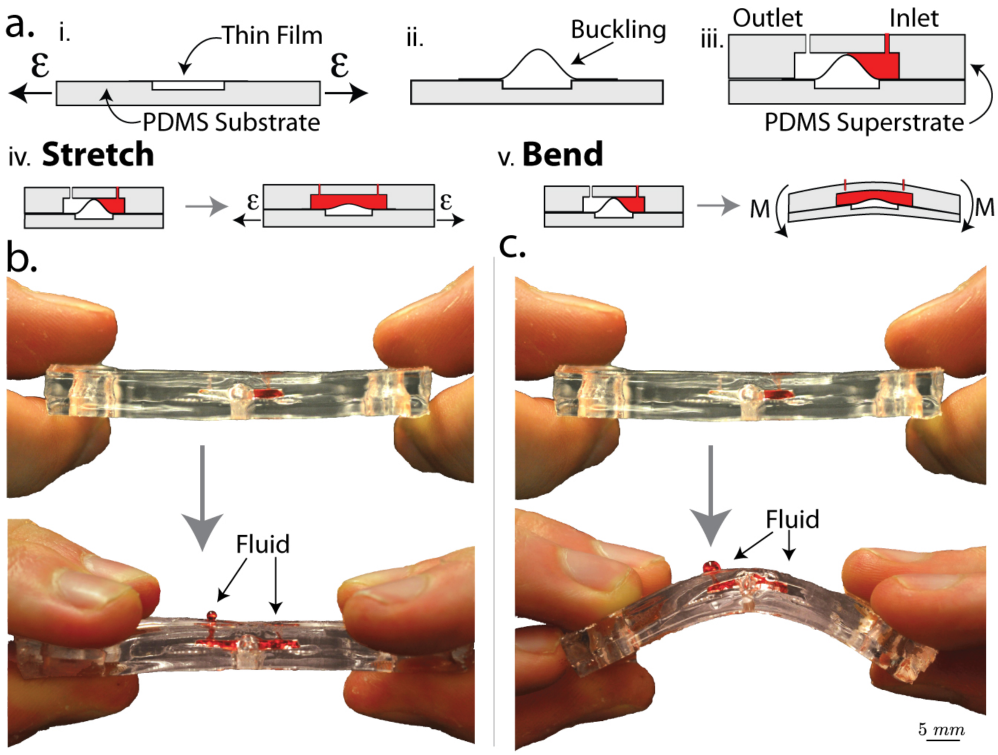

Figure 2.1: *a.* Schematics illustrating the fabrication and functionality of a device with an internal flexible valve. *i.* The substrate is stretched and then a thin film is bonded to it. *ii.* Upon releasing the initial strain, the thin film buckles to an arch, and *iii.* the substrate is fabricated into a microfluidic device, and the arch closes the channel. Applying an external mechanical loads such as *iv.* stretching and *v.* bending, partially opens the valve and allows fluid flow. *b.* & *c.* Images of the fabricated device that allows the fluid flow upon stretching and bending.

20AC Laboratory Corona Treater) for 30 s and incubated at 60°C for 5 min to enhance the bond strength (Figure 2.1a-i.). Upon release of the uniaxial strain ($\varepsilon_0 = 0.54$), the thin film buckles to form an arch of height $\widetilde{w}(x)$ along the length of the channel (Figure 2.1a-ii.). We measured the deflection $w(x)$, the length between the two points of contact L, and the extensions ΔL using an optical microscope (Leica DMI4000 B). Finally, the superstrate was bonded to the other side of the thin film using same oxygen plasma procedure in a way that the buckled film closes the top channel (Figure 2.1a-iii.). The two ends of the arch orthogonal to the length of the fluid channel were sealed using PDMS, and the width of the arch D in the z direction was chosen to be greater than the arch length ($D/L \gg 1$) in order to reduce the effect of boundaries on the shape of the arch.

2.3.3 Test Setup

For the flow rate experiments, we made inlet and outlet holes in the superstrate layer with a biopsy punch. To create a pressure drop ΔP from $-L/2$ to $L/2$, the inlet was connected to a water source at a fixed height ($1\ mm \leq H \leq 10\ mm$) controlled by a vertical micrometer. This generates a pressure drop across the entire channel of $10\ Pa \leq \Delta P \leq 100\ Pa$. Since precise measurement of the pressure drop across the flexible arch was unknown, we calculated the flow rate at a constant ΔP relative to an open channel, *i.e.* Q/Q_c where Q_c refers to $b/W = 1$. We determined the flow rate Q by measuring the weight of the water at the outlet as a function of time. Numerical simulations described below show negligible differences in flow rate over this range of pressure drops. Based on the channel dimensions and measured flow rate, the Reynolds number in these experiments was $\mathcal{R} \approx 0.1 - 1$. The range of experimental data was limited to small values of b/W because of the stiffness of the device (Figure 2.2a).

Since this buckled arch is embedded within a microfluidic device, there is a finite volume below the arch defined by the channel depth d. The ratio of final volume to initial volume cannot be neglected as this leads to a change in pressure below the arch that is enough to significantly deform the arch, and change the gap within the channel. The final pressure P_f compared to the initial atmospheric pressure P_{atm} was calculated by a simple integration of the geometry before and after fabrication, in conjunction with the ideal gas law. We chose the strain during fabrication to be $\Delta L/L \approx 0.5$ with $d/L \approx 1$ for the devices described in this paper, as these values correspond to $P_f/P_{atm} \approx 1.15$, which will have a negligible effect on the arch's shape.

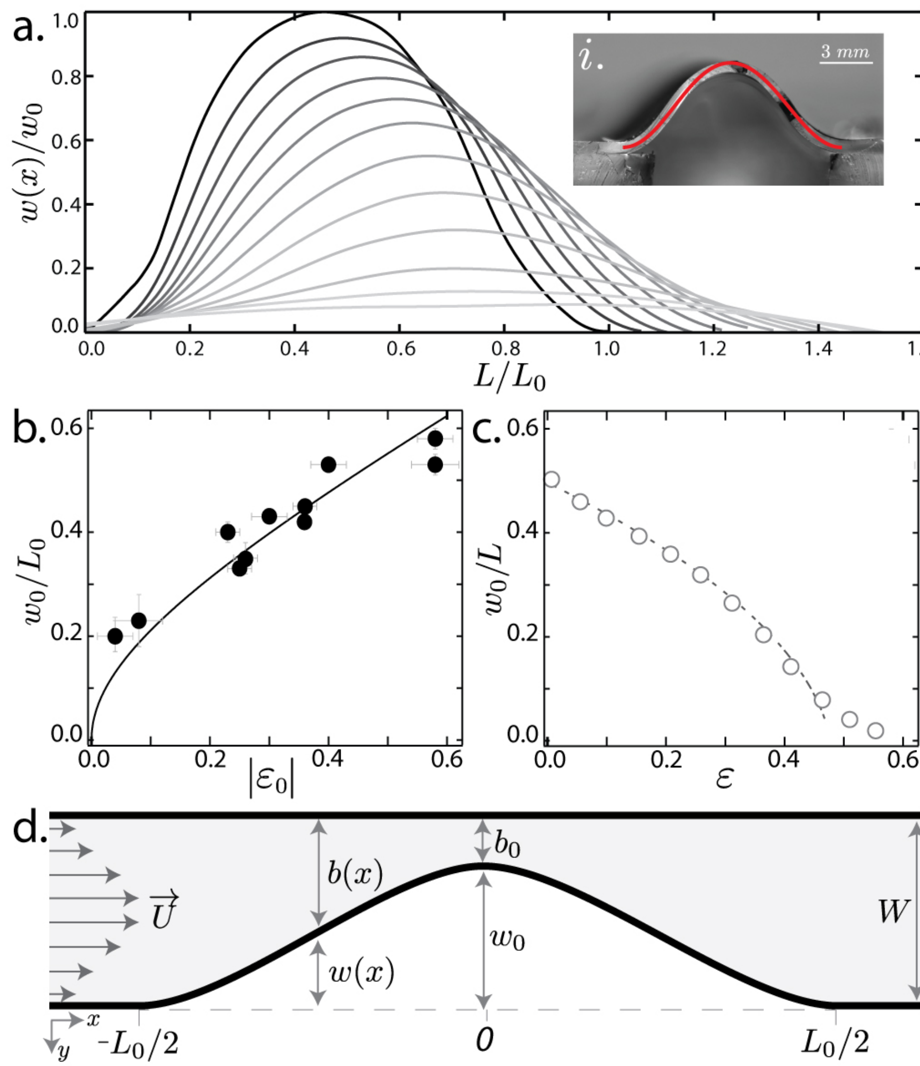

Figure 2.2: *a.* Experimentally measured profiles[†] of buckled thin films as each structure is stretched from its initial length $L_0 = 1.2$ mm to a new length L. *b.* The initial deflection of the center of the arch w_0/L_0 after fabrication is plotted as a function of the strain and equation 2.1, and the inset *i.* shows the cross section of an arch overlaid with the theoretical curve. *c.* The height of the arch at its center w/L is plotted as a function of strain with equation 2.2 and the identity $W = w+b$. *d.* A schematic of fluid flow within the microfluidic device. A fluid with velocity $\vec{U}$ flows from $-L/2$ to $L/2$ over an elastic arch with the shape $w(x)$. The height of the gap is described by the compliment of the arch's height, $b(x)$, that spans the channel height W.

2.4 Modeling

2.4.1 Flexible Valve

To develop the general construct for an internally controlled fluid flow device, we first consider the fabrication of a mechanically actuated valve, after which we determine a relationship between the geometry of the channel, the pressure drop, and the fluid flow rate. For the mechanically controlled valve, a thin elastomeric film is partially bonded to a uniaxially strained elastic substrate (Figure 2.1*a. i.*). Release of the strain on the substrate induces a uniaxial compressive strain ε_0, which buckles the thin film into an arch with a deflection w_0 at its center (Figure 2.1*a. ii.*). If we consider the symmetric buckling of a beam, the profile of the thin film will adopt a cosine shape [19], such that the arch height along its length is $\widetilde{w}(x) = \frac{w(x)}{L_0} = \frac{1}{\pi}\sqrt{\varepsilon_0\left(\varepsilon_0 - 1\right)}\left(1 + \cos\frac{2\pi x}{L_0}\right)$, where L_0 is the original length of the beam (Figure 2.2a). Therefore, after fabrication the height of the arch at its center, $w_0 = \widetilde{w}(0)$, is:

$$\frac{w_0}{L_0} = \frac{2}{\pi}\sqrt{\varepsilon_0\left(\varepsilon_0 - 1\right)}. \tag{2.1}$$

To confirm this relation, the arch height after fabrication w_0 was measured as a function of compressive strain ε_0, and we found good agreement between theory and our experimental results (Figure 2.2b).

With an accurate model of the arch height, we prepared a superstrate with a channel height $W = w_0$ for a specific ε_0, and bonded it to the flexible device substrate (Figure 2.1*a. iii.*), such that the minimum gap height within the channel is initially $b = 0$. Since the arch is deformable, uniaxial tension from stretching (Figure 2.1b) or bending (Figure 2.1c) the material by a strain ε will increase $L > L_0$, thereby decreasing the arch height $w \equiv \widetilde{w}(0)$, and increasing the gap height within the channel (Figure 2.2a). To develop a relationship between the channel geometry and mechanical strain, it is convenient to rewrite equation (2.1) in terms of the gap between arch's center and the top wall $b = W - w$, where w and b are the maximum arch height and minimum gap height for a given strain ε, respectively.

[†]Experimental profiles have to be shifted so that the maximum of the profile occurs at $x = 0$ to compare with $\widetilde{w}(x)$

By neglecting higher-order terms in ε, the minimum gap within the channel is:

$$\frac{b}{W} = 1 - \frac{2}{\pi}\frac{L_0}{W}\sqrt{\left(\frac{\pi}{2}\frac{w_0}{L_0}\right)^2 - \varepsilon}. \tag{2.2}$$

Figure 2.2c shows the change in arch height at its center as a function of uniaxially applied strain. The theoretical line (dashed) is in good agreement with our experimental results.

2.4.2 Fluid Flow

From equation (2.2), we know the geometry within the channel as an applied uniaxial strain ε causes the gap to go from closed, $b/W = 0$, to open, $b/W = 1$ (Figure 2.2d). Using this relationship between ε and b, we can now determine by a perturbation calculation the flow rate Q through the channel for a given pressure drop ΔP. We consider a two-dimensional flow in a rectangular channel, with a flow rate $Q_c = \frac{W^3 \Delta P}{12\mu L}$, and assume that the aspect ratio $\delta = b/L$ and the Reynolds number $\mathcal{R} = \rho b u_c/\mu$ satisfy $\delta \ll 1$ and $\mathcal{R}\delta \ll 1$, where $u_c = \frac{Q_c}{b}$ is the characteristic fluid velocity, μ is the fluid viscosity, and ρ is the fluid density. We have solved this problem numerically and also developed analytical approximations useful for prediction and design. From the momentum balance, we have two differential equations for the pressure change in the x and y directions, such that, in dimensionless form, $\partial_x p = \partial^2_{yy} u + \delta^2 \partial^2_{xx} u$ and $\partial_y p = \delta^2 \partial^2_{yy} v + \delta^4 \partial^2_{xx} v$, where x is normalized by the length L_0, and y is normalized by the width W. In these equations, δ only exists as even powers, suggesting that the dimensionless velocities $u = \frac{U}{q_0/W}$, $v = \frac{V}{q_0/L_0}$, and dimensionless pressure $p = \frac{Pb^2}{\mu u_c L}$ can be determined by a series expansion in even powers of δ, *e.g.* $u(x, y) = \sum_{n=0}^{\infty} \delta^{2n} u_{2n}$. We assume no-slip boundary conditions along the walls and along the arch, and at zeroth order, we obtain:

$$\Delta p_0 = \frac{3\left(8 - 8\lambda + 3\lambda^2\right)}{\left(1 - \lambda\right)^{5/2}}, \tag{2.3}$$

where $\lambda = 1 - \frac{b}{W}$. By replacing u_0 and p_0 into the equations for momentum balance at the second order and solving for the velocities u_2, and v_2, we determine for the pressure drop at the second order,

$$\Delta p_2 = \frac{12\pi^2\lambda^2}{5\left(1 - \lambda\right)^{3/2}}. \tag{2.4}$$

The fourth-order term, Δp_4, can be determined in the same manner (see Chapter 3). With the normalized pressure drop at each order of the expansion, we can return these terms to dimensional quantities by knowing the gap within the channel, and calculate the total pressure drop $\Delta P = \sum_{n=0}^{\infty} \delta^{2n} \Delta P_{2n}$.

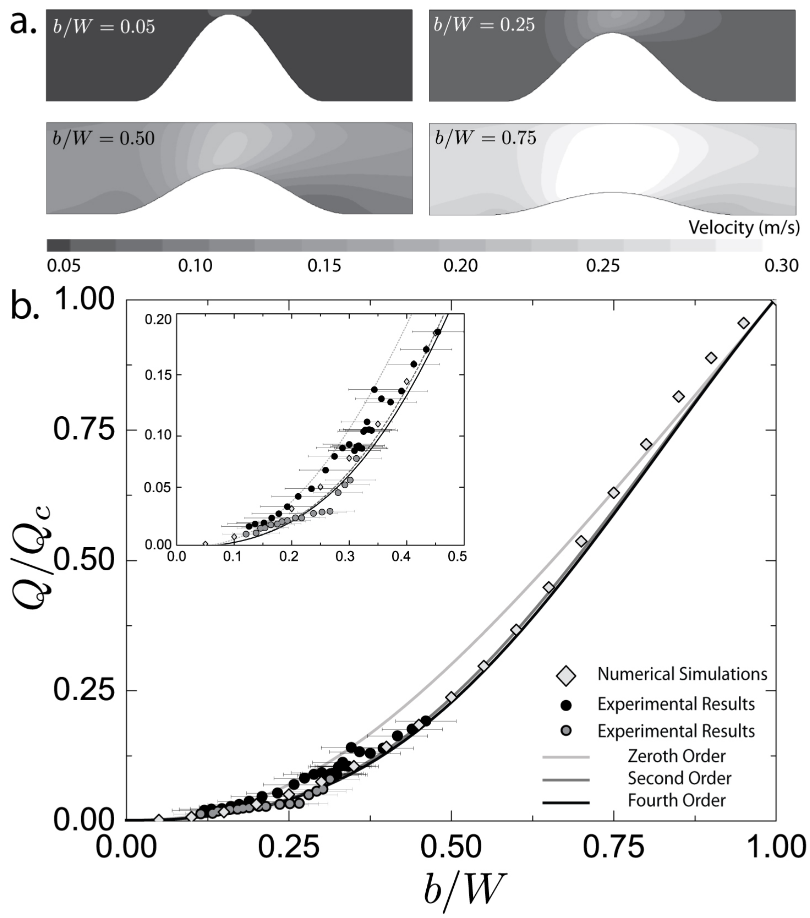

Figure 2.3: *a.* Numerical simulations of pressure-driven flow for several channels with different gap heights b/W. *b.* The flow rate Q normalized by the two-dimensional flow in a rectangular channel Q_c and plotted versus b/W. The solid lines represent the zeroth, second, and fourth order solutions to the perturbation approach in lubrication theory.

2.5 Results and Discussion

Using the total pressure drop and normalizing it by the pressure drop in an empty rectangular channel, $\Delta P_c = 12\mu Q L W^{-3}$, we can calculate the flow rate $Q = \sum_{n=0}^{\infty} \delta^{2n} Q_{2n}$ normalized by the flow rate in an empty channel Q_c. To confirm this perturbation calculation experimentally, we applied a constant pressure between the inlet and outlet of the device, and measured the flow rate at the outlet. In addition to the experimental study, we used computational analysis to verify the analytical solution. The channel was modeled in COMSOL 4.2 with the geometry and boundary conditions identical to the experimental conditions within the fabricated microfluidic device. The channel was assumed to be filled with water at the beginning while the flow was driven by a constant pressure of $\Delta P = 10\ Pa$ and $\Delta P = 100\ Pa$. The deformation of the arch was neglected. The Navier-Stokes equation was used in its full form for incompressible flow to include the role of inertial effects as the valves open and the flow speeds increase. We performed numerical simulations across the entire range of microfluidic gap heights (Figure 2.3a). The theory, numerical simulations, and experimental results are plotted in Figure 2.3b and are in very good agreement. The higher-order expansions appear to better describe the fluid flow as the gap between the arch and the wall increases. In this way, we can now predict the magnitude of internal flow within the deformed microstructured material for a given applied internal pressure difference and a given opening of the arch.

The above experiments and model provide an approach to have external mechanical stresses induce internal fluid flow. A primary advantage to this design is that more complex microfluidic architecture leads to advanced functionality. Internally structured materials often exhibit unexpected mechanical behavior, such as the strength and stiffness of cellular solids [20], and the negative Poisson behavior [21] of foams [22] and periodically microstructured materials [23, 24]. We demonstrate the ability to direct fluid flow towards regions of high mechanical stress by preparing two arches in series and applying a high pressure in the channel between them (Figure 2.4a). Both valves are initially closed and the applied fluid pressure in the middle cannot cause the valves to open, i.e. the pressure is not high enough to deform the valves; otherwise, the system may behave differently. With this configuration, locally applied mechanical stress to one end of the device, in this case the right side, will cause one arch to deform, *i.e.* $b/W > 0$, creating a pressure gradient in the direction of the mechanically applied load. Therefore, opening of a single valve, as seen experimentally and numerically in Figure 2.4a-c, causes fluid flow from left to right, in the direction of the applied load. It should be noted that without these internal valves, the fluid can go to either sides since we have high fluid pressure in the middle and low fluid pressure in both sides. Therefore, the fluid pressure only helps to have flow but the direction of the flow is determined by the externally mechanical stress. In this simple demonstration, the fluid flows from regions of high fluid pressure to low fluid pressure, yet because of the material's internal microstructure, this pressure drop occurs in the direction of the externally applied mechanical stress.

It is clear that a wide variety of functionality can be attained when the flexible microfluidic architecture is increased in complexity. Internally directing fluid flow with these structural valves provides compelling opportunities for moving fluid within microstructured materials. For example, embedding multiple arrays of flexible valves and microchannels within a porous material will enable external loads to move fluid in a gradient controlled by the internal microstructure. Structuring the porosity of a material, and therefore the deformation of its microstructure, could enable a material to exhibit "negative" poroelasticity, where the gradient of fluid flow is opposite of a normal poroelastic material, such that the fluid flows towards the externally applied stress.

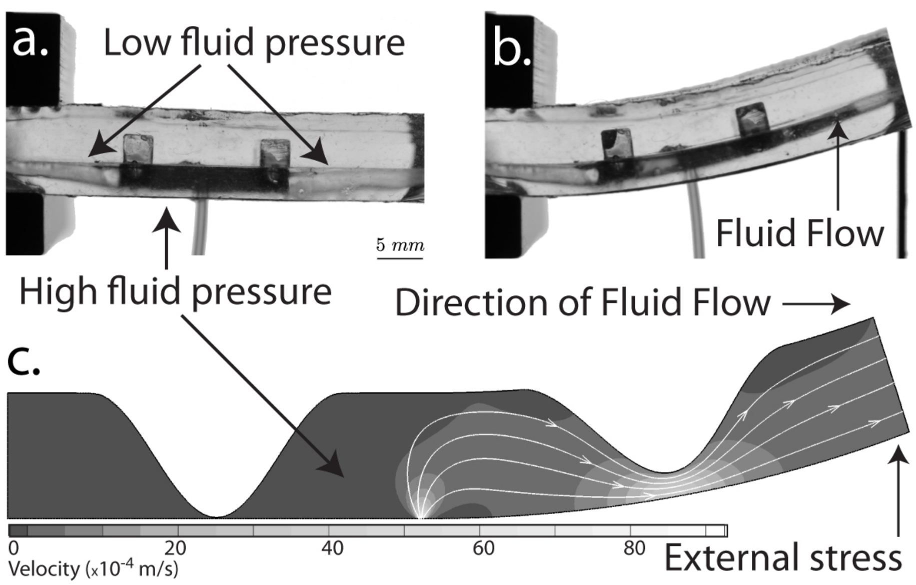

Figure 2.4: *a*. A microfluidic device with two flexible arches in series is clamped at one end and a line load applied to the opposite end. *b*. The localized deformation causes the arch closest to the applied load to deform and allow fluid to flow towards the region of high stress. *c*. A numerical simulation of the multichannel arch illustrates the directed fluid flow.

2.6 Conclusions

We have demonstrated the ability to direct and control fluid flow within a microstructured device by adjusting the microfluidic architecture. The general experimental and theoretical framework provides new capabilities for directed fluid flow using internally controlled structural deformations. By taking advantage of the inherent flexibility of typical microfluidic devices, advances can be made in microchannels for *in situ* mixing, chemical reactions, or rapid, portable chemical analysis. Additionally, proper tuning of material properties will allow directed fluid flow to be actuated by a variety of triggers, including electrical, thermal, and osmotic actuation.

References

[1] T. J. Pedley and X. Y. Luo. “Modelling Flow and Oscillations in Collapsible Tubes”. In: *Theoretical and Computational Fluid Dynamics* 10.1-4 (1998), pp. 277–294.

[2] J. B. Grotberg and O. E. Jensen. “Biofluid mechanics in flexible tubes”. In: *Annual Review of Fluid Mechanics* 36 (2004), pp. 121–147.

[3] T. J. Pedley, B. S. Brook, and R. S. Seymour. “Blood Pressure and Flow Rate in the Giraffe Jugular Vein”. In: *Philosophical Transactions of the Royal Society of London. Series B: Biological Sciences* 351.1342 (1996), pp. 855–866.

[4] T. S. Gross, J. L. Edwards, K. J. McLeod, and C. T. Rubin. “Strain Gradients Correlate with Sites of Periosteal Bone Formation”. In: *Journal of Bone and Mineral Research* 12.6 (1997), pp. 982–988.

[5] S. Judex, T. S. Gross, and R. F. Zernicke. “Strain Gradients Correlate with Sites of Exercise-Induced Bone-Forming Surfaces in the Adult Skeleton”. In: *Journal of Bone and Mineral Research* 12.10 (1997), pp. 1737–1745.

[6] S. P. Fritton and S. Weinbaum. “Fluid and Solute Transport in Bone: Flow-Induced Mechanotransduction”. In: *Annual review of fluid mechanics* 41 (2009), pp. 347–374.

[7] H. A. Stone, A. D. Stroock, and A. Ajdari. "Engineering flows in small devices: Microfluidics toward a lab-on-a-chip". In: *Annual Review of Fluid Mechanics* 36 (2004), pp. 381–411.

[8] T. Thorsen, S. J. Maerkl, and S. R. Quake. "Microfluidic large-scale integration". In: *Science* 298.5593 (2002), pp. 580–584.

[9] D. C. Leslie, C. J. Easley, E. Seker, J. M. Karlinsey, M. Utz, M. R. Begley, and J. P. Landers. "Frequency-specific flow control in microfluidic circuits with passive elastomeric features". In: *Nature Physics* 5.3 (2009), pp. 231–235.

[10] W. Wu, A. DeConinck, and J. A. Lewis. "Omnidirectional Printing of 3D Microvascular Networks". In: *Advanced Materials* 23.24 (2011), H178–H183.

[11] M. A. Burns et al. "An Integrated Nanoliter DNA Analysis Device". In: *Science* 282.5388 (1998), pp. 484–487.

[12] P. Tabeling. *Introduction to microfluidics*. Oxford University Press, 2005. ISBN: 0198568649.

[13] E. Berthier and D. J. Beebe. "Flow rate analysis of a surface tension driven passive micropump". In: *Lab on a Chip* 7.11 (2007), pp. 1475–1478.

[14] G. W. Scherer, J. H. Prevost, and Z.-H. Wang. "Bending of a poroelastic beam with lateral diffusion". In: *International Journal of Solids and Structures* 46 (2009), pp. 3451–3462.

[15] H. S. Kim and A. J. Crosby. "Solvent-Responsive Surface via Wrinkling Instability". In: *Advanced Materials* 23.36 (2011), pp. 4188–4192.

[16] G. M. Whitesides. "What Comes Next?" In: *Lab on a Chip* 11.2 (2011), pp. 191–193.

[17] Y. Sun, W. M. Choi, H. Jiang, Y. Y. Huang, and J. A. Rogers. "Controlled buckling of semiconductor nanoribbons for stretchable electronics". In: *Nat Nano* 1.3 (2006), pp. 201–207.

[18] D.-Y. Khang, H. Jiang, Y. Huang, and J. A. Rogers. "A Stretchable Form of Single-Crystal Silicon for High-Performance Electronics on Rubber Substrates". In: *Science* 311.5758 (2006), pp. 208–212.

[19] D. Vella, J. Bico, A. Boudaoud, B. Roman, and P. M. Reis. "The macroscopic delamination of thin films from elastic substrates". In: *Proceedings of the National Academy of Sciences* 106.27 (2009), pp. 10901–10906.

[20] L. J. Gibson and M. F. Ashby. “The Mechanics of Three-Dimensional Cellular Materials”. In: *Proceedings of the Royal Society of London A: Mathematical, Physical and Engineering Sciences* 382.1782 (1982), pp. 43–59.

[21] R. F. Almgren. “An isotropic three-dimensional structure with Poisson’s ratio–1”. In: *Journal of Elasticity* 15 (1985), pp. 427–430.

[22] R. Lakes. “Foam Structures with a Negative Poisson’s Ratio”. In: *Science* 235.4792 (1987), pp. 1038–1040.

[23] K. Bertoldi, P. M. Reis, S. Willshaw, and T. Mullin. “Negative Poisson’s Ratio Behavior Induced by an Elastic Instability”. In: *Advanced Materials* 22.3 (2010), pp. 361–366.

[24] Z. G. Nicolaou and A. E. Motter. “Mechanical metamaterials with negative compressibility transitions”. In: *Nat Mater* 11.7 (2012), pp. 608–613.

Chapter 3

Extended Lubrication Theory: Improved Estimates of Flow in Channels with Variable Geometry

3.1 Abstract

Any constriction or change in geometry of a channel affects the fluid flow within that channel. This constriction might be due to the buckling of a flexible arch (as discussed in the previous chapter), swelling of the channel walls, or even any sediment or colloids partially blocking the channel. In this chapter, we offer an extension to lubrication theory by considering higher-order terms of the analytical approximation to describe the fluid flow in a channel with features of a modest aspect ratio. We perform experiments and simulations to verify the analytical solutions. We show that the extended lubrication theory is a robust tool for an accurate estimation of pressure drop in channels with constrictions, as long as the constrictions' geometries are known, on the order of the channel height, and piece-wise differentiable.

3.2 Introduction

Lubrication theory is an approximation to the Navier-Stokes and continuity equations at low Reynolds numbers for narrow geometries with slow changes in curvature [1–3]. The approach is used regularly to describe the velocity field and pressure gradient in fluid film lubricants [4, 5], the motion of particles within a fluid and near boundaries [6, 7], the fluid flow passing through a microchannel with a known geometry [8–11], flow driven by the contracting walls of a soft channel, *e.g.*, an insect's trachea [12, 13], and the flow of thin liquid films with free-surfaces [14], e.g., when a droplet wets a solid surface [15, 16]. Classical lubrication theory (CLT) is suitable for all of the above cases provided that the ratio of thickness to the axial length scale is on the order of $\mathcal{O}\left(10^{-1}\right)$ or less. Due to its simplicity and versatile applications, lubrication theory is widely applied. Earlier work on flows in sinusoidally constricted pipe with radial variations comparable to axial variations was studied numerically, e.g. Tilton and Payatakes [17], where we note that our higher-order approach below effectively gives an analytical solution to the problem. A similar higher-order expansion was also used recently in a study of an electrokinetic flow in a channel of nonuniform shape [18].

In this study, we obtain higher-order terms of the lubrication approximation and present an extension to lubrication theory, which we refer to as extended lubrication theory (ELT), to address two limitations of CLT. First, the use of ELT is no longer limited to small gaps and thin films. Second, the boundaries can be described by any mathematical shape function with arbitrary curvatures as long as they are continuous and differentiable. In addition, we show how the differentiability condition may be relaxed at low Reynolds numbers, at least in practice, by considering geometries that are piece-wise differentiable. We compare the results of different orders of the analytical solutions with experimental results and also with direct numerical solutions of the Navier-Stokes equations to define a threshold for considering higher-order terms in the solution. Accuracy of the analytical solutions are examined for channels with a differentiable constriction or convexity as well as for channels with shapes with finite non-differentiable points.

3.3 Theoretical Approximation

We consider working to higher order in traditional lubrication theory to describe fluid flow in nonuniform channel shapes with modest aspect ratios. Thus, we consider incompressible, steady, two-dimensional pressure-driven flow in a channel with shape $y = h(x) = h_0 H(X)$, where $X = x/L_0$, L_0 is the channel length, h_0 is a characteristic channel height, $H(X)$ is a normalized shape function, and $\delta = h_0/L_0 \ll 1$. A typical geometry in the form of a constriction is shown in Fig. 3.1a. We assume that the Reynolds number is small and so consider the continuity and Stokes equations

$$\nabla \cdot \mathbf{u} = 0 \qquad \text{and} \qquad \mu \nabla^2 \mathbf{u} = \nabla p, \tag{3.1}$$

where $\mathbf{u} = (u, v)$ is the velocity field and μ is the fluid viscosity. We denote the constant flow rate (per unit width) as q_0. Consistent with the traditional lubrication approximation we choose to introduce dimensionless variables according to

$$X = \frac{x}{L_0}, \quad Y = \frac{y}{h_0}, \quad U = \frac{u}{q_0/h_0}, \quad V = \frac{v}{q_0/L_0}, \quad P = \frac{p}{\Delta p} = \frac{p}{\mu q_0 L_0/h_0^3}. \tag{3.2}$$

Note that the scaling for the transverse velocity component v is $\mathcal{O}(h_0/L_0) \ll 1$ smaller than the scaling for u, which is the component of flow along the channel axis. The dimensionless equations corresponding to (3.1) for a two-dimensional flow are

$$\frac{\partial U}{\partial X} + \frac{\partial V}{\partial Y} = 0 \tag{3.3a}$$

$$\delta^2 \frac{\partial^2 U}{\partial X^2} + \frac{\partial^2 U}{\partial Y^2} = \frac{\partial P}{\partial X} \tag{3.3b}$$

$$\delta^4 \frac{\partial^2 V}{\partial X^2} + \delta^2 \frac{\partial^2 V}{\partial Y^2} = \frac{\partial P}{\partial Y}. \tag{3.3c}$$

These equations are to be solved with boundary conditions

$$U = 0, \; V = 0 \quad \text{at } Y = 0, H(X), \quad \text{and} \quad \int_0^{H(X)} U(X,Y)\,\mathrm{d}Y = 1, \tag{3.4}$$

where the integral constraint states that the total flow rate is prescribed. We will determine the corresponding pressure drop across the constriction such that the pressure gradient tends to a constant as $X \to \pm 1$. Note that the problem statement only involves one dimensionless parameter δ^2.

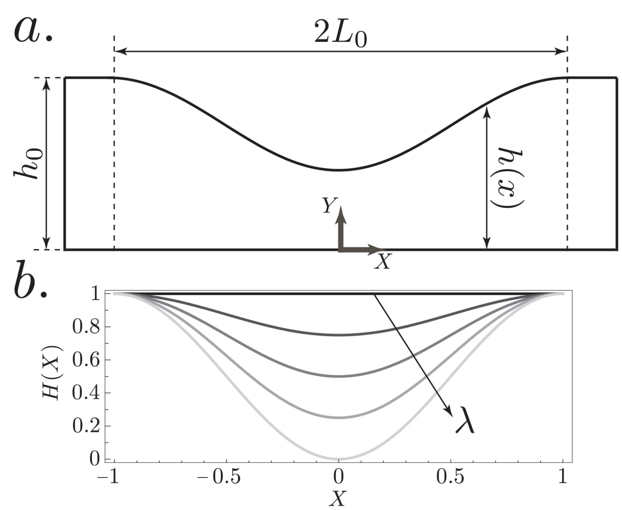

Figure 3.1: *(a)* A schematic of the channel with shape $y = h(x) = h_0 H(x)$. *(b)* Shape function of $H(X) = 1 - \frac{\lambda}{2}(1 + \cos(\pi X))$ for different λ.

3.3.1 Perturbation expansion and the leading-order results

Our first steps follow standard discussions in textbooks, e.g. Leal [2]. Because the problem statement only involves δ^2, which is assumed to be small, we seek a solution to (3.3) of the form

$$U(X,Y;\delta) = U_0(X,Y) + \delta^2 U_2(X,Y) + \delta^4 U_4(X,Y) + \cdots \tag{3.5a}$$

$$V(X,Y;\delta) = V_0(X,Y) + \delta^2 V_2(X,Y) + \delta^4 V_4(X,Y) + \cdots \tag{3.5b}$$

$$P(X,Y;\delta) = P_0(X,Y) + \delta^2 P_2(X,Y) + \delta^4 P_4(X,Y) + \cdots \tag{3.5c}$$

At leading order, we have the familiar classical lubrication problem

$$\frac{\partial U_0}{\partial X} + \frac{\partial V_0}{\partial Y} = 0 \tag{3.6a}$$

$$\frac{\partial^2 U_0}{\partial Y^2} = \frac{\partial P_0}{\partial X} \tag{3.6b}$$

$$\frac{\partial P_0}{\partial Y} = 0, \tag{3.6c}$$

with $U_0 = 0$ at $Y = 0$ and $H(X)$. The solution is

$$U_0(X,Y) = \frac{1}{2}\frac{dP_0}{dX}\left(Y^2 - YH(X)\right) \tag{3.7}$$

and the pressure gradient, which only depends on X, follows from applying the integral constraint
$\left(\int_0^{H(X)} U_0(X,Y)\ \mathrm{d}Y = 1\right)$

$$\frac{dP_0}{dX} = -\frac{12}{H(X)^3}. \tag{3.8}$$

The corresponding velocity distribution is then

$$U_0(X,Y) = \frac{6}{H(X)^3}\left(YH(X) - Y^2\right). \tag{3.9}$$

To provide an example, we consider the shape function

$$H(X) = 1 - \frac{\lambda}{2}\left(1 + \cos\left(\pi X\right)\right) \quad (1 > \lambda \geq 0), \tag{3.10}$$

as sketched in Fig. 3.1b. The leading-order pressure drop ΔP_0 is then calculated to be (the integration was accomplished with Mathematica)

$$\begin{aligned} P_0(-1) - P_0(1) = \Delta P_0 = -\int_{-1}^{1} \frac{dP_0}{dX}\ \mathrm{d}X = 12\int_{-1}^{1} \frac{1}{\left(1 - \frac{\lambda}{2} - \frac{\lambda}{2}\cos\left(\pi X\right)\right)^3}\ \mathrm{d}X \\ = \frac{3\left(3\lambda^2 - 8\lambda + 8\right)}{\left(1-\lambda\right)^{5/2}}. \end{aligned} \tag{3.11}$$

Before proceeding further, we determine the velocity component $V_0(X,Y)$ using the continuity equation. Although equation (3.6) is first order in Y, we expect it to satisfy two boundary conditions, as $V_0(X,0) = V_0(X,H(X)) = 0$. Using the continuity equation, and imposing $V_0\left(X,0\right) = 0$, we have

$$V_0(X,Y) = -\int_0^Y \frac{\partial U_0\left(X,S\right)}{\partial X}\ \mathrm{d}S, \tag{3.12}$$

which yields

$$V_0(X,Y) = 2Y^3\left(H^{-3}\right)' - 3Y^2\left(H^{-2}\right)', \tag{3.13}$$

where primes denotes X derivatives. We then note that at $Y = H(X)$ direct differentiation shows that (3.13) yields $V_0(X,H(X)) = 0$. Alternatively, we can write

$$V_0(X,H(X)) = -\int_0^{H(X)} \frac{\partial U_0}{\partial X}\ \mathrm{d}Y = -\frac{d}{dX}\int_0^{H(X)} U_0\ \mathrm{d}Y + U_0(X,H(X))\frac{dH}{dX} = 0, \tag{3.14}$$

as the second term on the right-hand side vanishes owing to the no-slip condition and the first term on the right-hand side vanishes since the flow rate is constant. The same idea applies for evaluating the Y-component of velocity at every order in the analysis below and the no-slip boundary condition is satisfied for both velocity components of $\mathbf{u}$.

3.3.2 The $\mathcal{O}\left(\delta^2\right)$ term in the perturbation expansion

In most calculations utilizing lubrication theory the development is truncated with the leading-order term calculated in the preceding section. Here our interest is to improve the approximation by including additional terms in the perturbation solution. At the next order, $\mathcal{O}\left(\delta^2\right)$, the perturbation expansion yields

$$\frac{\partial U_2}{\partial X} + \frac{\partial V_2}{\partial Y} = 0 \tag{3.15a}$$

$$\frac{\partial^2 U_2}{\partial Y^2} - \frac{\partial P_2}{\partial X} = -\frac{\partial^2 U_0}{\partial X^2} \tag{3.15b}$$

$$\frac{\partial P_2}{\partial Y} = \frac{\partial^2 V_0}{\partial Y^2}, \tag{3.15c}$$

with boundary conditions $U_2 = 0$ at $Y = 0$ and $H(X)$, and $\int_0^{H(X)} U_2(X,Y)\ \mathrm{d}Y = 0$. This last integral constraint follows since all of the fluid flux is specified in the scaling used to establish the leading-order problem. We seek the velocity distribution and pressure drop $\Delta P_2 = P_2\left(-1\right) - P_2\left(1\right)$ needed to enforce the constraint on the flux.

We can integrate the last equation of (3.15), and use continuity, to obtain

$$P_2(X,Y) = -\frac{\partial U_0}{\partial X} + c_3(X), \tag{3.16}$$

where the function $c_3(X)$ is allowed by the integration. With this pressure distribution, we use the X-momentum equation to find

$$\frac{\partial^2 U_2}{\partial Y^2} = \frac{dc_3}{dX} - 2\frac{\partial^2 U_0}{\partial X^2} \tag{3.17}$$

where U_0 is given by equation (3.9). Upon integration, and application of the boundary conditions, we find

$$\begin{aligned} U_2(X,Y) = {} & -2\left(H(X)^{-2}\right)''\left(Y^3 - H(X)^2 Y\right) + \left(H(X)^{-3}\right)''\left(Y^4 - H(X)^3 Y\right) \\ & + \frac{1}{2}\frac{dc_3}{dX}\left(Y^2 - H(X)Y\right). \end{aligned} \tag{3.18}$$

Since we have accounted for the specified dimensionless flow rate at leading order, then we now require
$\int_0^{H(X)} U_2(X,Y)\ \mathrm{d}Y = 0$, which leads to

$$\frac{dc_3}{dX} = 6\left(H(X)^{-2}\right)'' H(X) - \frac{18}{5}\left(H(X)^{-3}\right)'' H(X)^2. \tag{3.19}$$

Equations (3.18) and (3.19) give the second-order X-component of the velocity $U_2(X,Y)$ for any shape function $H(X)$. To continue with the example of Fig. 3.1, we again use the shape function in equation (3.10). Integrating (3.16), taking into account that $\frac{\partial U_0}{\partial X}$ vanishes as $X \to -1$ and 1, and using (3.19), we obtain the pressure drop ΔP_2 at this order as

$$P_2(-1) - P_2(1) = \Delta P_2 = -\int_{-1}^{1} \frac{\partial P_2}{\partial X}\,\mathrm{d}X = -\int_{-1}^{1} \frac{dc_3}{dX}\,\mathrm{d}X = \frac{12\pi^2\lambda^2}{5\,(1-\lambda)^{3/2}}. \tag{3.20}$$

We determine $V_2(X,Y)$ using the continuity equation and imposing $V_2(X,0) = 0$, which leads to the expression

$$\begin{aligned} V_2(X,Y) = {} & \left(H(X)^{-2}\right)''' \left(\frac{1}{2}Y^4 - H(X)^2Y^2\right) - 2\left(H(X)^{-2}\right)'' H'(X)Y^2 \\ & - \left(H(X)^{-3}\right)''' \left(\frac{1}{5}Y^5 - H(X)^3Y^2\right) + \frac{3}{2}\left(H(X)^{-3}\right)'' \left(H'(X)\right)^2 Y^2 \\ & - \frac{d^2c_3}{dX^2}\left(\frac{1}{6}Y^3 - \frac{1}{4}HY^2\right) + \frac{1}{4}\frac{dc_3}{dX}H'(X)Y^2. \end{aligned} \tag{3.21}$$

This equation only involves the shape function $H(X)$, since $\frac{dc_3}{dX}$ is given in (3.19). As in the previous section, it can be verified that $V_2(X,H(X)) = 0$.

3.3.3 The perturbation expansion at $\mathcal{O}\left(\delta^4\right)$

It is useful to go one step further simply to illustrate that the basic analytical steps carry through at every order. The higher-order terms help to provide a better representation of flows in geometries with more rapid shape variations. We can continue these basic steps at $\mathcal{O}\left(\delta^4\right)$, where we have the equations

$$\frac{\partial U_4}{\partial X} + \frac{\partial V_4}{\partial Y} = 0 \tag{3.22a}$$

$$\frac{\partial^2 U_4}{\partial Y^2} - \frac{\partial P_4}{\partial X} = -\frac{\partial^2 U_2}{\partial X^2} \tag{3.22b}$$

$$\frac{\partial P_4}{\partial Y} = \frac{\partial^2 V_2}{\partial Y^2} + \frac{\partial^2 V_0}{\partial X^2}, \tag{3.22c}$$

with $U_4 = 0$ at $Y = 0$ and $H(X)$, and $\int_0^{H(X)} U_4(X,Y)\,\mathrm{d}Y = 0$. Using the results obtained above, these equations can be solved, though the algebraic manipulations involved become progressively more cumbersome. We outline the main steps below. First, the Y-momentum equation can be integrated, which, after using the continuity equation, yields

$$P_4(X,Y) = -\frac{\partial U_2}{\partial X} + \frac{\partial^2}{\partial X^2}\int_0^Y V_0(X,S)\ \mathrm{d}S + c_5\left(X\right). \tag{3.23}$$

Second, from the X-momentum equation we have

$$\frac{\partial^2 U_4}{\partial Y^2} = -2\frac{\partial^2 U_2}{\partial X^2} + \frac{\partial^3}{\partial X^3}\int_0^Y V_0(X,S)\ \mathrm{d}S + \frac{dc_5}{dX}. \tag{3.24}$$

Since $U_2(X,Y)$ is known from equation (3.18), then we calculate

$$\begin{aligned}\frac{\partial^2 U_2}{\partial X^2} &= \left(H^{-3}\right)'''' Y^4 - 2\left(H^{-2}\right)'''' Y^3 + \left[-\left(H^3\left(H^{-3}\right)''\right)'' + 2\left(H^2\left(H^{-2}\right)''\right)''\right] Y \\ &+ \frac{1}{2}\frac{d^3c_3}{dX^3}Y^2 - \frac{1}{2}\left(H\frac{dc_3}{dX}\right)'' Y.\end{aligned} \tag{3.25}$$

Combining the last two results, we find

$$\begin{aligned}\frac{\partial^2 U_4}{\partial Y^2} &= -\frac{3}{2}\left(H^{-3}\right)'''' Y^4 + 3\left(H^{-2}\right)'''' Y^3 + \left[2\left(H^3\left(H^{-3}\right)''\right)'' - 4\left(H^2\left(H^{-2}\right)''\right)''\right] Y \\ &- \frac{d^3c_3}{dX^3}Y^2 + \left(H\frac{dc_3}{dX}\right)'' Y + \frac{dc_5}{dX}.\end{aligned} \tag{3.26}$$

It is straightforward to integrate twice and apply $U_4 = 0$ at $Y = 0$ and $H(X)$ to arrive at

$$\begin{aligned}U_4(X,Y) &= -\frac{1}{20}\left(H^{-3}\right)''''\left(Y^6 - H^5 Y\right) + \frac{3}{20}\left(H^{-2}\right)''''\left(Y^5 - H^4 Y\right) \\ &+ \frac{1}{3}\left[\left(H^3\left(H^{-3}\right)''\right)'' - 2\left(H^2\left(H^{-2}\right)''\right)''\right]\left(Y^3 - H^2 Y\right) \\ &- \frac{1}{12}\frac{d^3c_3}{dX^3}\left(Y^4 - H^3 Y\right) + \frac{1}{6}\left(H\frac{dc_3}{dX}\right)''\left(Y^3 - H^2 Y\right) + \frac{1}{2}\frac{dc_5}{dX}\left(Y^2 - HY\right).\end{aligned} \tag{3.27}$$

Since $\int_0^{H(X)} U_4(X,Y)\ \mathrm{d}Y = 0$, we obtain $\frac{dc_5}{dX}$

$$\begin{aligned}\frac{dc_5}{dX} &= \frac{3}{14}\left(H^{-3}\right)'''' H^4 - \frac{3}{5}\left(H^{-2}\right)'''' H^3 - \left[\left(H^3\left(H^{-3}\right)''\right)'' - 2\left(H^2\left(H^{-2}\right)''\right)''\right] H \\ &+ \frac{3}{10}\frac{d^3c_3}{dX^3}H^2 - \frac{1}{2}\left(H\frac{dc_3}{dX}\right)'' H.\end{aligned} \tag{3.28}$$

The equations (3.18), (3.27), and (3.28) give the $X-$component velocity at this order for any choice of the shape function $H(X)$. We determine the correction to the pressure drop as

$$P_4(-1) - P_4(1) = \Delta P_4 = -\int_{-1}^{1} \frac{\partial P_4}{\partial X}\,\mathrm{d}X = -\int_{-1}^{1} \frac{dc_5}{dX}\,\mathrm{d}X$$
$$= \frac{8\pi^4\left(-428\left(-1+\sqrt{1-\lambda}\right)+214\left(-2+\sqrt{1-\lambda}\right)\lambda+53\lambda^2\right)}{175\sqrt{1-\lambda}}, \qquad (3.29)$$

where we have used Mathematica to accomplish the final integration for the shape function (3.10).

For a given flow rate (q_0), we have determined the dimensionless pressure drop $\Delta P = (\Delta p_{measured}) \,/\, (\mu\, q_0 L_0/h_0^3)$ as a function of δ, where $\Delta p_{measured}$ is the difference in pressure measured at the two ends of the constriction. In particular, $\Delta P = \Delta P_0(\lambda) + \delta^2 \Delta P_2(\lambda) + \delta^4 \Delta P_4(\lambda) + \mathcal{O}(\delta^6)$, where λ is defined by the given shape function (3.10).

We next describe experiments and numerical simulations to confirm the improved description offered by these additional terms in the lubrication approximation.

3.4 Experimental Verification

Our experimental setup consists of a long channel (200 mm) with a rectangular cross section (5 mm by 5 mm) and an obstruction in the middle (Fig. 3.2a). The sides of the channel were cut from acrylic sheets (8560K211, McMaster-Carr) using a laser cutter (Epilog Mini Laser 24, 60 Watts) and bonded together using an acrylic capillary cement (10705, TAP Plastics). We varied the arch size and shape, similar to Fig. 3.1, while keeping all other geometrical parameters constant between different tests. We recognize that our theory is two-dimensional and the experimental geometry is three-dimensional. However, as the arch amplitude increases, the flow through the narrow gap better approximates a two-dimensional flow.

The pressure drop within the channel between two fixed points, symmetrically located on each side of the arch, was measured using a sensitive differential pressure sensor (CPCL04D, Honeywell). By keeping the flow rate constant for different tests, the pressure drop across the arch was then obtained by subtracting the pressure drop within the flat part of the channel from the total pressure drop between those fixed points. The fluid was chosen to be a standard viscosity oil (N1000, Cannon Instrument) and the temperature was kept at

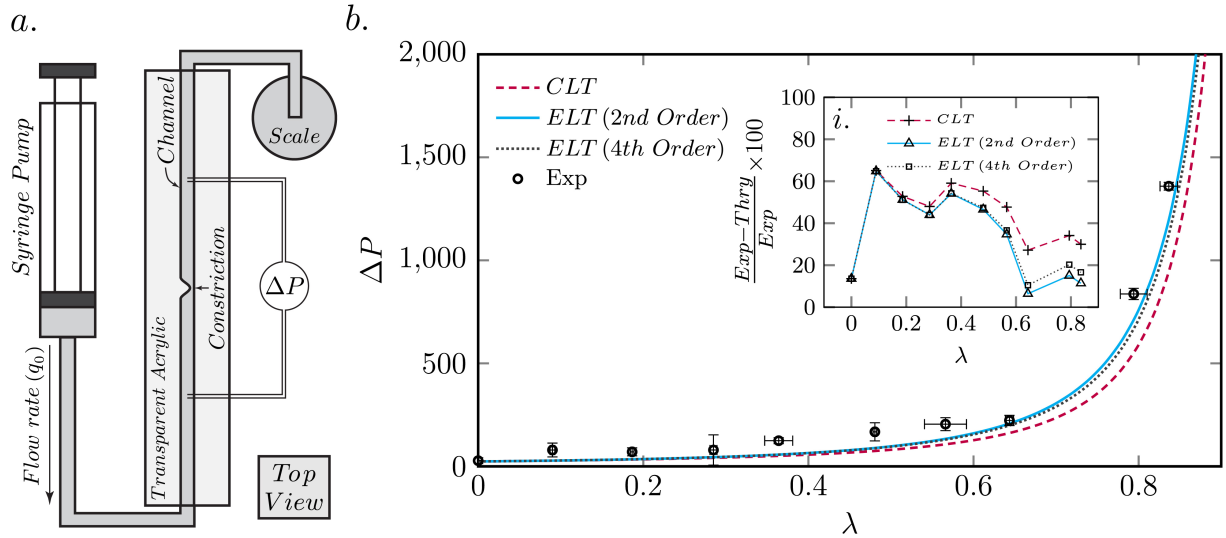

Figure 3.2: *a.* A schematic of the experimental setup from the top view. A constant flow rate was applied using a syringe pump and the pressure drop was measured using a sensitive pressure sensor. A scale was also used to verify the applied flow rate. For all of the experiments, $L_0 \approx h_0 \approx 5\,\mathrm{mm}$. *b.* Comparison of the dimensionless pressure drop across the arch showing the analytical solutions and experimental results ($\delta \approx 1$). The inset shows the difference between the experiment and the theory, suggesting that higher orders of the analytical solutions are in better agreement with the experimental results.

22.5 ± 0.5^oC, resulting in a viscosity of 2.45 Pa.s and density of 848 Kg/m^3. We used a syringe pump (PHD Ultra CP, Harvard Apparatus) to apply a fixed flow at a rate of 14.4 mm^3/s so that $\mathcal{R}e \approx 0.001$ for all the tests. The arch height was measured by taking images of the setup using a camera (FASTCAM Mini UX100) and then processing those images using a MATLAB code.

We repeated each test at least three times and the average measured pressure drops along with their associated standard deviations are shown in Fig. 3.2b. We note that higher orders of the analytical solutions are in better agreement with the experimental results while the CLT (red dotted line) underestimates the results by about 40 %. We also note that the analytical solutions are obtained in a two-dimensional channel while the experimental results are from a three-dimensional channel, and this is one of the reasons for the difference between the analytical and experimental results. Although the experimental results confirm the trend in the analytical solutions, it may not be feasible to conduct experiments for every case to verify the higher orders of the analytical solutions due to the sensitivity and the difficulty of such experiments. So we performed numerical simulations for variety of cases and compared those results with the analytical solutions in the next section.

3.5 Numerical Simulations

We seek to numerically solve the Navier-Stokes equation in its full form for incompressible, steady two-dimensional flow. The same scalings and dimensionless parameters introduced in equation (3.2) are used to obtain the dimensionless continuity and Navier-Stokes equations

$$\frac{\partial U}{\partial X} + \frac{\partial V}{\partial Y} = 0 \tag{3.30a}$$

$$\mathcal{R}e\ \delta \left(U\frac{\partial U}{\partial X} + V\frac{\partial U}{\partial Y} \right) = -\frac{\partial P}{\partial X} + \delta^2 \frac{\partial^2 U}{\partial X^2} + \frac{\partial^2 U}{\partial Y^2} \tag{3.30b}$$

$$\mathcal{R}e\ \delta^3 \left(U\frac{\partial V}{\partial X} + V\frac{\partial V}{\partial Y} \right) = -\frac{\partial P}{\partial Y} + \delta^4 \frac{\partial^2 V}{\partial X^2} + \delta^2 \frac{\partial^2 V}{\partial Y^2}, \tag{3.30c}$$

where $\mathcal{R}e = \rho\, q_0/\mu$ is the Reynolds number, ρ is the fluid density, and μ is the fluid viscosity. In the lubrication literature, it is common to define the reduced Reynolds number, $\mathcal{R}e^* = \mathcal{R}e\, \delta$, which also appears in (3.30). A numerical solver often uses the weak form of (3.30). To do so, we consider an arbitrary pair of P and $\mathbf{U} = (U, V)$ to be a solution to the dimensionless continuity and Navier-Stokes equations (3.30) for a steady and incompressible flow. If these equations are multiplied by any pressure and velocity basis functions, *i.e.* (q, ν_1, ν_2), and integrated over the domain Ω, the pair is still a solution, and satisfies the new equations. We then reduce all the second-order terms to first-order ones using Gauss's theorem and neglect the boundary integrals as they are usually handled separately in finite element packages. Therefore, we have the following weak form of the continuity and Navier-Stokes equations that can directly be used within numerical solvers:

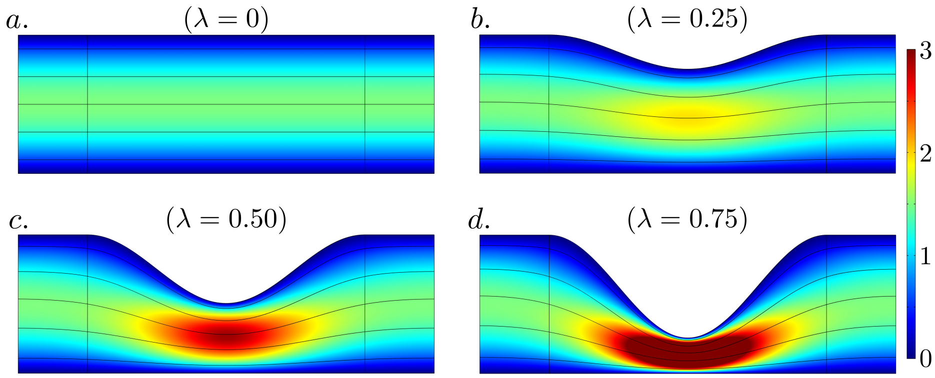

Figure 3.3: Velocity magnitude obtained using numerical simulations for $\mathcal{R}e = 1, \delta = 1$, and λ varied from 0 to 0.75 (*a*-*d*).

$$0 = \int_\Omega \left[\frac{\partial U}{\partial X} + \frac{\partial V}{\partial Y}\right] q \, \mathrm{d}\Omega \tag{3.31a}$$

$$0 = \int_\Omega \left[\nu_1 \left(\mathcal{R}e\, \delta \left(U\frac{\partial U}{\partial X} + V\frac{\partial U}{\partial Y}\right) + \frac{\partial P}{\partial X}\right) + \delta^2 \frac{\partial \nu_1}{\partial X}\frac{\partial U}{\partial X} + \frac{\partial \nu_1}{\partial Y}\frac{\partial U}{\partial Y}\right] \mathrm{d}\Omega \tag{3.31b}$$

$$0 = \int_\Omega \left[\nu_2 \left(\mathcal{R}e\, \delta^3 \left(U\frac{\partial V}{\partial X} + V\frac{\partial V}{\partial Y}\right) + \frac{\partial P}{\partial Y}\right) + \delta^4 \frac{\partial \nu_2}{\partial X}\frac{\partial V}{\partial X} + \delta^2\frac{\partial \nu_2}{\partial Y}\frac{\partial V}{\partial Y}\right] \mathrm{d}\Omega. \tag{3.31c}$$

We used COMSOL 4.3b for meshing the geometry and also for solving the above equations. These dimensionless equations depend on two dimensionless parameters: Reynolds number and the geometric variable $\delta = h_0/L_0$. In addition, the shape function (3.10) adds another dimensionless parameter, λ, to this system. While we recognize that our theory, which is based on Stokes equations, is strictly valid only when $\mathcal{R}e = 0$, we have highlighted that for problems with two distinct length scales (h_0 and L_0) the ratio of the inertia to the viscous terms in the Navier-Stokes equations involves the product of $\mathcal{R}e$ and δ. Thus, below we have also performed some numerical calculations with finite $\mathcal{R}e$ to show that the results are still useful for finite Reynolds numbers.

We performed the numerical simulations for a range of $\mathcal{R}e = 0 - 20$ and $\delta = 0.2 - 1$ while varying λ from 0 to 0.99. The dimensionless channel height was $H_0 = 1$ and we applied a flow at the inlet at a fixed rate with a parabolic velocity profile of $6\,(Y - Y^2)$ so that $Q = 1$. The outlet pressure was also set to zero. After solving the governing equations, the pressure drop was measured at two cross sections that are symmetrically located on each side of the arch and separated by $2L_0$. These scales respect the nondimensionalization in Section II. Simulation results for $\mathcal{R}e = 1, \delta = 1$, and different λ are shown in Fig. 3.3. Since the flow rate is constant, the pressure drop increases rapidly as the gap becomes smaller (alternatively, λ increases).

The comparison between simulation results and different orders of the analytical solutions for a channel with a shape function provided in (3.10) is shown in Fig. 3.4. As expected from textbook discussions of classical lubrication theory, when δ is small, *i.e.* $\delta \leq 0.2$, the CLT as well as higher orders ELT estimate the pressure drop accurately (the errors are within 5% when $\mathcal{R}e \leq 10$). By increasing $\delta \to 1$, the CLT estimations deviate significantly from the simulation results (about 20 %) while higher orders ELT are still in very good agreement with the simulation results, *i.e.*, three terms in the asymptotic expansion in δ (including terms $\mathcal{O}(\delta^4)$) provides very good results even when $\delta \to 1$ (Fig. 3.4a). We also note that if a maximum 4% error is acceptable, the second-order ELT would be adequate to estimate the pressure drop for a simple shape like (3.10) while $\delta \leq 1$ and $\mathcal{R}e \leq 10$. As we further increase the Reynolds number, even the higher orders of the analytical solutions do not estimate the pressure drop accurately as inertial forces become more dominant than the viscous forces and can no longer be ignored.

We note that perturbation approximation can still be accurate even if the perturbation parameter, δ, is not small [19–22]. In fact, the validity of the perturbation method relies mainly on the good approximation of the leading-order term while a rapid convergence of higher-order terms may improve the approximation [19]. The leading-order term in this study, the classical lubrication theory, provides a good estimation of pressure drop. In addition, the higher-order terms of the pressure drop for a fixed λ converge rapidly. Therefore, perturbation method provides accurate approximation for this problem even when δ is not small.

We then investigate the use of higher-order ELT in applications where a channel, instead of an obstruction, has a convex shape. We choose the shape function (3.10) while varying λ from 0 (no bulge) to -1 (bulge with the size of the channel height) (Fig. 3.5a). This convexity alters the flow profile (Fig. 3.5b) and reduces the pressure drop within the channel. We performed numerical analyses for different $\delta, \mathcal{R}e$, and λ and the comparisons are shown in Fig. 3.5c. Since we have shown that even for $\delta = 1$ the extended lubrication theory

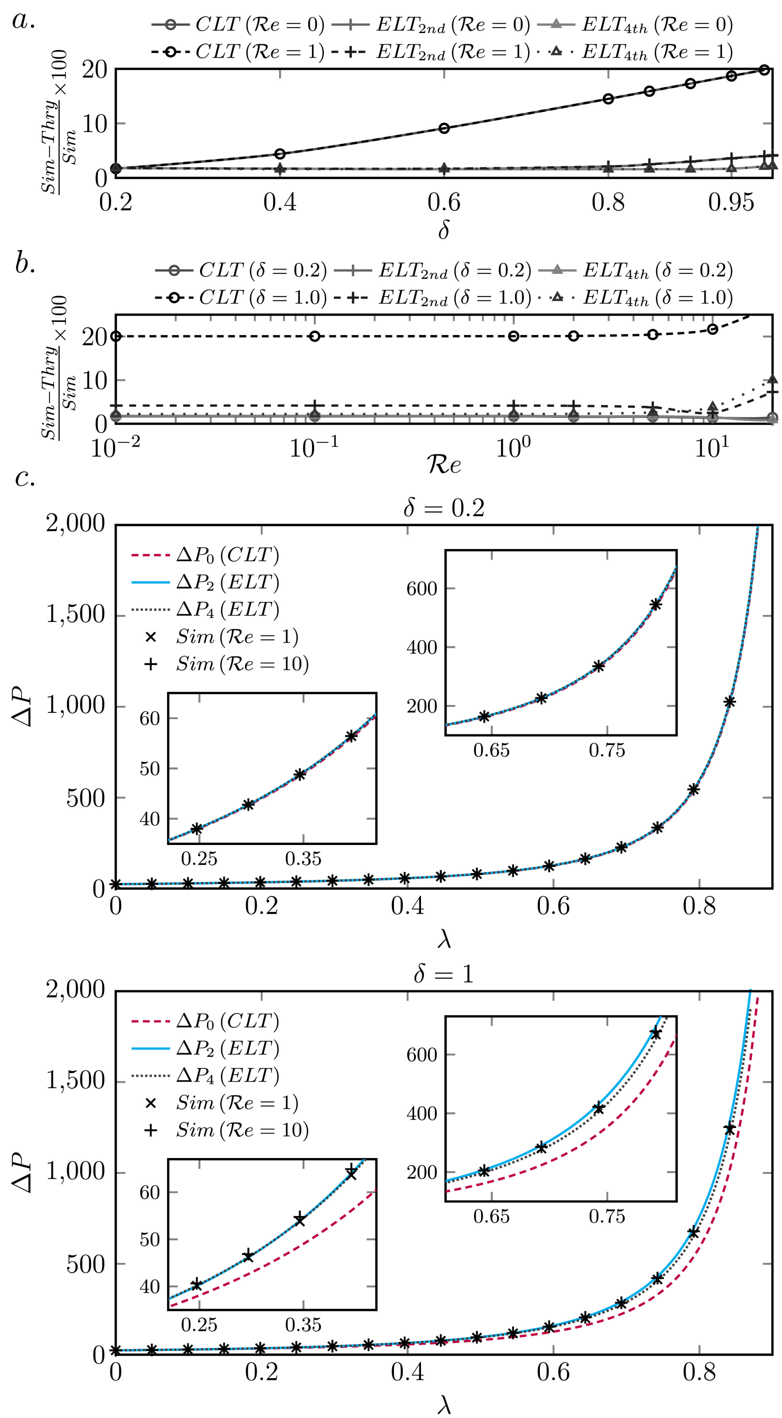

Figure 3.4: *a.* and *b.* Deviation of different orders of the analytical solutions from the simulation results while varying δ and $\mathcal{R}e$, respectively. Each point corresponds to the maximum difference between the simulation and analytical results when changing λ from 0 to 0.99. We note that as $\delta \to 1$, the deviation of CLT from the simulation results becomes significant (about 20%) while higher-order analytical solutions are still in a very good agreement with the simulation results for any $\mathcal{R}e \leq 10$. *c.* Comparison of the dimensionless pressure drop across the arch showing the analytical solutions and simulation results when $\delta = 0.2$ and $\delta = 1$.

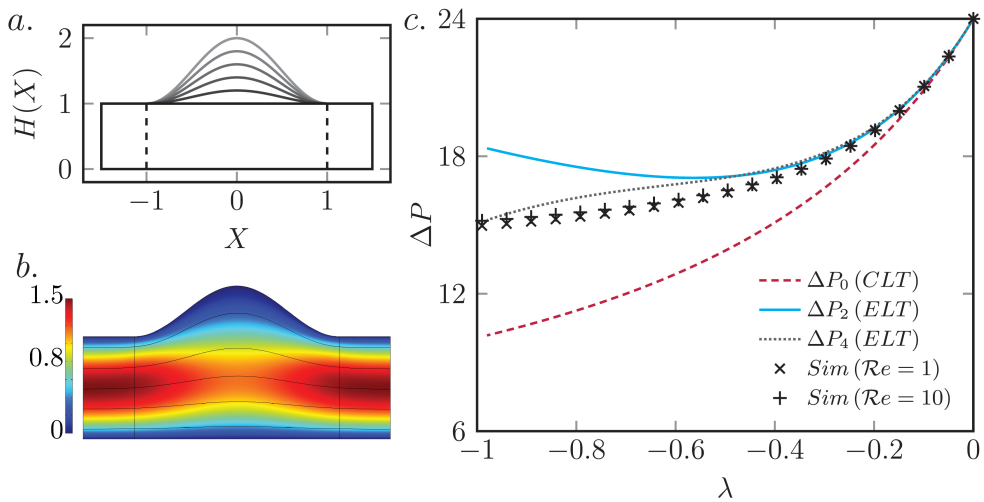

Figure 3.5: *a.* A schematic of a channel with a convex shape. The bulge becomes larger as $\lambda \to -1$. *b.* Velocity magnitude of a channel with 50% convexity ($\lambda = -\frac{1}{2}$), when $\delta = 1$ and $\mathcal{R}e = 1$. *c.* Comparison of the dimensionless pressure drop between simulation results and different orders of the analytical solutions for a channel with a convexity shape provided in a, when $\delta = 1$.

provides a reasonable approximation to the full numerical simulations (Fig. 3.4a), here we choose $\delta = 1$. For a channel with a sharp convexity, only fourth-order ELT and higher may accurately estimate the pressure drop (within 5% error) while CLT and the second-order ELT estimations differ from the simulation results by about 30% and 20%, respectively. Therefore, higher orders of the analytical solutions significantly improve the estimation of pressure drop within a channel with a significant change in geometry.

Until now, we have used shape functions that are entirely differentiable. This condition may not be met in models of all applications. Here we provide of an example showing that ELT can be applied to a channel whose shape is continuous but piece-wise differentiable, i.e. the shape function may have finite non-differentiable points. A channel with such a shape function can be divided into smaller sections where each part has a differentiable shape. The pressure drop within each piece is estimated using ELT. Since the flow is laminar, the total pressure drop across the original channel is the summation of the pressure drops within each part. For example, consider a shape function with a single non-differentiable point as follows

$$H(X) = \begin{cases} 1 - \frac{\lambda}{2\gamma}(X+1) & -1 \le X \le 2\gamma - 1, \\ 1 + \frac{\lambda}{2(1-\gamma)}(X-1) & 2\gamma - 1 < X \le 1, \end{cases} \tag{3.32}$$

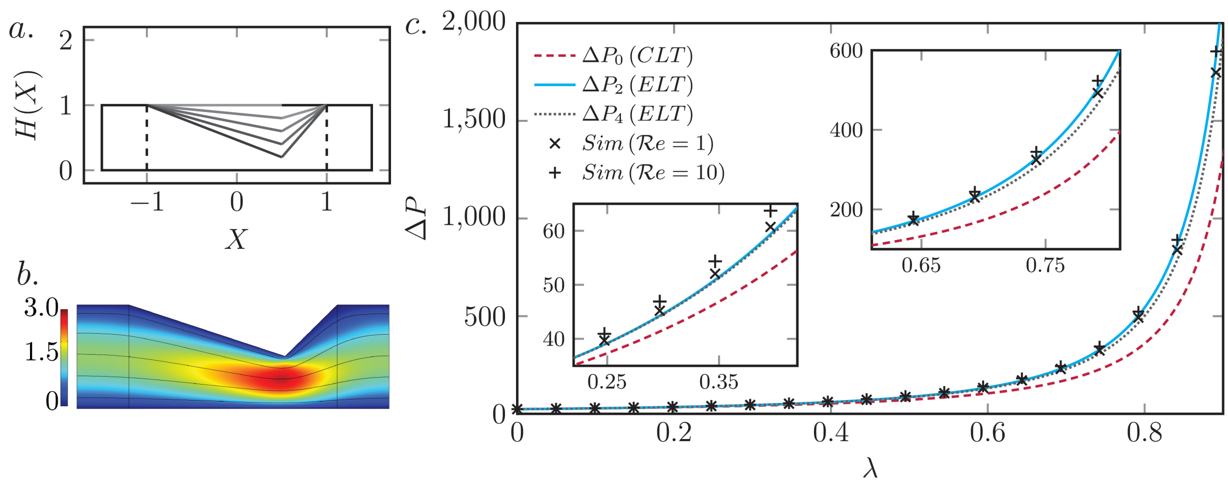

Figure 3.6: *a.* A schematic of a channel with a shape function that is not differentiable at $\gamma = 0.75$ (see equation (3.32) for the definition of γ). The gap size decreases as $\lambda \to 1$. *b.* Velocity magnitude of a channel with a non-differentiable point at $\gamma = 0.75$, when $\delta = 1$ and $\mathcal{R}e = 1$. *c.* Comparison of the dimensionless pressure drop between simulation results and different orders of the analytical solutions for a channel with a single non-differentiable point, provided in *a*, when $\delta = 1$.

where $0 < \gamma < 1$ is a dimensionless parameter that determines the location of the discontinuity in slope and $1 - \lambda$ gives the minimum gap height. This shape function is plotted for $\gamma = 0.75$ in Fig. 3.6a. Following the same procedure introduced in Section II, the pressure drop is

$$\Delta P = \Delta P_0 \left(1 + \frac{4}{5}\,\lambda^2\,\delta^2 - \frac{64}{225}\,\lambda^4\,\delta^4 + \mathcal{O}\left(\delta^6\right)\right) \tag{3.33}$$

where $\Delta P_0 = \frac{12\,(2-\lambda)}{(1-\lambda)^2}$, and the terms inside the parentheses correspond to CLT, second-order ELT, fourth-order ELT, and so on, respectively. We used the same shape function (3.32) to perform numerical simulations, and the comparison is shown in Fig. 3.6b. For channels with small δ ($\delta \leq 0.2$), theoretical and numerical results are in good agreement, while for channels with $\delta \approx 1$, pressure drop estimated using the higher orders of the analytical solutions follow the numerical results more closely. These results show that ELT can be applied to a channel with a piece-wise differentiable shape function. We note that shape functions can appear on both sides of a channel and the same procedure can be followed to find analytical solutions at different orders.

3.6 Conclusions

We extended the lubrication approximation by obtaining higher-order terms in a systematic perturbation analysis and compared the analytical results with experiment and numerical simulations. Experimental results were closer to higher-order analytical solutions when the gap was narrow so that the two-dimensional approximation was appropriate. Very good agreement was found between higher-order analytical solutions and the simulation results, confirming that for channels with a high aspect ratio, the higher-order terms of the extended lubrication theory results in a significant improvement in accuracy as compared to the classical lubrication theory. For low Reynolds numbers, simple piece-wise differentiable shape functions can be used with the analytical solutions obtained in this study, which provides a robust tool to accurately estimate the pressure drop in a channel with positive or negative constrictions, whose changes in height are comparable to its length.

References

[1] W. E. Langlois. *Slow Viscous Flow*. New York: Macmillan, 1964.

[2] L. G. Leal. *Advanced Transport Phenomena: Fluid Mechanics and Convective Transport Processes*. Cambridge: Cambridge University Press, 2007.

[3] H. Ockendon and J. R. Ockendon. *Viscous Flow*. Cambridge: Cambridge University Press, 1995.

[4] A. Szeri. *Fluid Film Lubrication: Theory and Design*. Cambridge University Press, 2005.

[5] A. T. John. "Hydrodynamic Lubrication". In: *Handbook of Lubrication and Tribology, Volume II*. doi:10.1201/b12265-18. CRC Press, 2012, pp. 1–14.

[6] H. A. Stone. "On Lubrication Flows in Geometries with Zero Local Curvature". In: *Chemical Engineering Science* 60.17 (2005), pp. 4838–4845.

[7] M. C. Marchetti, J. F. Joanny, S. Ramaswamy, T. B. Liverpool, J. Prost, M. Rao, and R. A. Simha. "Hydrodynamics of Soft Active Matter". In: *Reviews of Modern Physics* 85.3 (2013), pp. 1143–1189.

[8] O. Amyot and F. Plouraboue. “Capillary Pinching in a Pinched Microchannel”. In: *Physics of Fluids* 19.3 (2007).

[9] H. A. Stone, A. D. Stroock, and A. Ajdari. “Engineering flows in small devices: Microfluidics toward a lab-on-a-chip”. In: *Annual Review of Fluid Mechanics* 36 (2004), pp. 381–411.

[10] F. Plouraboue, S. Geoffroy, and M. Prat. “Conductances between Confined Rough Walls”. In: *Physics of Fluids* 16.3 (2004), pp. 615–624.

[11] D. P. Holmes, B. Tavakol, G. Froehlicher, and H. A. Stone. “Control and manipulation of microfluidic flow via elastic deformations”. In: *Soft Matter* 9.29 (2013), pp. 7049–7053.

[12] Y. Aboelkassem and A. E. Staples. “Flow Transport in a Microchannel Induced by Moving Wall Contractions: a Novel Micropumping Mechanism”. In: *Acta Mechanica* 223.3 (2012), pp. 463–480.

[13] Y. Aboelkassem and A. E. Staples. “A Bioinspired Pumping Model for Flow in a Microtube with Rhythmic Wall Contractions”. In: *Journal of Fluids and Structures* 42 (2013), pp. 187–204.

[14] J. H. Snoeijer. “Free-Surface Flows with Large Slopes: Beyond Lubrication Theory”. In: *Physics of Fluids* 18.2 (2006).

[15] D. Bonn, J. Eggers, J. Indekeu, J. Meunier, and E. Rolley. “Wetting and Spreading”. In: *Reviews of Modern Physics* 81.2 (2009), pp. 739–805.

[16] L. Limat and H. A. Stone. “Three-Dimensional Lubrication Model of a Contact Line Corner Singularity”. In: *EPL (Europhysics Letters)* 65.3 (2004), p. 365.

[17] J. N. Tilton and A. C. Payatakes. “Collocation solution of creeping newtonian flow through sinusoidal tubes: A correction”. In: *AIChE Journal* 30.6 (1984), pp. 1016–1021.

[18] S. Michelin, T. D. Montenegro-Johnson, G. De Canio, N. Lobato-Dauzier, and E. Lauga. “Geometric pumping in autophoretic channels”. In: *Soft Matter* (2015).

[19] J. P. Boyd. “The devil’s invention: asymptotic, superasymptotic and hyperasymptotic series”. In: *Acta Applicandae Mathematica* 56.1 (1999), pp. 1–98.

[20] C. M. Bender and S. A. Orszag. *Advanced Mathematical Methods for Scientists and Engineers I*. Springer Science & Business Media, 1999.

[21] M. Frasca. "Duality in perturbation theory and the quantum adiabatic approximation". In: *Physical Review A* 58.5 (1998), p. 3439.

[22] Z. Drmac, V. Hari, L. Sopta, Z. Tutek, and K. Veselic. *Applied Mathematics and Scientific Computing*. Springer, 2003.

Chapter 4

Buckling Instability of Dielectric Elastomeric Films

This work has been published in *Soft Matter*. Here it is reproduced by permission of The Royal Society of Chemistry.

4.1 Abstract

Buckling instability, when properly implemented within soft, mechanical structures, can generate advanced functionality. In this chapter, we use the voltage–induced buckling of thin, flexible plates to pump fluids within a microfluidic channel. The soft electrodes that enable electrical actuation are compatible with fluids, and undergo large, reversible deformations. We quantified the onset of voltage-induced buckling, and measured the flow rate within the microchannel. This embeddable, flexible microfluidic pump will aid in new generation of stand-alone microfluidic devices that require a tunable flow rate.

4.2 Introduction

Advances in microfluidic technology have introduced innovative ways to control fluid flow on a small scale [1–5]. The active control of fluid flow within such devices is crucial for further improvements in nanofluidics [6, 7], biomedical fluidic devices [8–10], and digital microfluidics [11–13]. The complexity of microfluidic channels has advanced to resemble integrated circuitry [1, 4, 14], and the mechanisms that move fluid within these channels now require the same degree of flexibility and precision. Electrically active soft materials that deform in response to an applied voltage may provide this advanced functionality [15]. In this paper, we present a means for microfluidic control via the electrical actuation of thin, flexible films within microfluidic channels. These structures consist of a dielectric elastomer confined between two compliant electrodes that can actively and reversibly buckle out of the plane to pump fluids in response to an applied voltage. The use of elastic electrodes enables a robust and reversible pumping mechanism that will have improvements in rapid microfluidic diagnostics, adaptive materials, and artificial muscles.

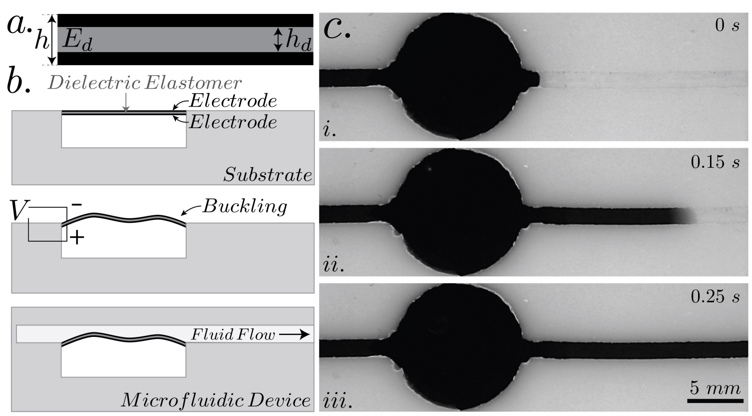

Figure 4.1: *a.* A schematic of the composite plate. *b.* Schematics of the electrically active microfluidic pump: A thin composite plate consists of a pre-strained dielectric elastomer with electrodes bonded on each side while the plate is clamped at its edges. Applying a voltage across the clamped thin plate causes an out-of-plane deformation, which can be used to move the fluid within microchannels. *c.* Actuation of the dielectric elastomer by applying the voltage pushes fluid (dyed water) with a flow rate of 20 mm^3/s into the microchannel.

When a film of a soft dielectric elastomer (DE) is sandwiched between two electrode films, creating a composite plate (Figure 4.1a), applying a voltage to the electrodes produces an electric field within the DE that induces a Maxwell stress through its thickness [16]. As a result, the DE is compressed by pulling opposite charges on two electrodes closer and stretched by spreading similar charges on each electrode [17, 18]. If the composite plate has free edges, the applied voltage will cause it to expand in-plane [19–25]. If, instead, the plate is clamped at the electrode edges, thus prevented from expanding laterally, the plate will buckle out of the plane above a critical compressive stress. In this paper, we show that embedding this confined plate within a microfluidic channel and applying an adequate voltage (Figure 4.1b) allows the buckling instability to move the fluid and control the flow (Figure 4.1c). We will discuss the critical voltage required to induce buckling, the subsequent buckling modes that emerge, and the impact that the pressure around the electro-active plate has on the fluid flow rate.

4.3 Design of Experiment

4.3.1 Preparation of conductive PDMS as flexible electrodes

Flexible conductive electrodes were made by mixing carbon black (CB) particles into PDMS using the following procedure: 3 wt.% CB particles (Ketjenblack EC-600JD, AkzoNobel) were dispersend in 40 mL of tetrahydrofuran (Sigma-Aldrich) for 1 hour using a tip-ultrasonicator (VirSonic 100). An ice-bath was used to prevent overheating of the suspension. Then, the suspension was transferred to the uncrosslinked PDMS (vinyl terminated PDMS with 9400 Da molecular weight, Gelest Inc.) that was preheated to 70 °C. The mixture was continuously stirred and heated for about 4 hours to allow the solvent to evaporate. After adding the catalyst (Platinum-Cyclovinylmethylsiloxane Complex, Gelest Inc.) and crosslinker (Tetrakis (dimethylsiloxy) silane, Gelest Inc.), and manual mixing for 10 minutes before casting on both sides of the dielectric fim.

4.3.2 Fabrication of the composite thin plate

VHB 4910 acrylic tape (3M) was used as the dielectric elastomeric film, which was stretched biaxially to 250% prestraining, and attached to an acrylic frame (8560K171, McMaster-Carr) for maintaining the prestrain. The electrodes' geometry was defined using a polyester film with a circular pattern (diameter: 13.5 mm) and the conductive PDMS mixture was cast directly on both sides of the prestrained DE film. The cast electrodes were cured at room temperature for 48 hours prior to use. For easy voltage application to the electrodes, we used conductive copper tape (SPI Supplies) bonded to the conducting PDMS electrodes using a silver epoxy paste (CW2400, Ted Pella Inc.).

4.3.3 Characterization of the composite thin plate

The geometrical parameters and material properties of the fabricated pumping device are as follows: Plate radius was measured using a caliper ($R = 6.75$ mm). DE thickness was calculated based on the applied pre-strain ($h_d = (82 \pm 5)\ \mu$m). The plate's total thickness was measured using a caliper to be $h = (180 \pm 20)\ \mu$m. To determine the residual stress, we applied constant 250% strain to VHB samples with thickness of 1 mm, gauge length of 128 mm, and width of 25 mm, and measured the changes in force under that strain for 30 min. Uniaxial residual stress was then obtained by dividing the plateau value of the force curve by the final cross sectional area of the samples ($\sigma_i = (100 \pm 40)$ kPa). After running the stress relaxation test and while the sample was under 250% strain, we performed a simple tension test to obtain the elastic modulus of the VHB film under pre-strain and subjected to stress relaxation condition ($E_d = 350$ kPa). Electrode modulus was $E_e = 800$ kPa [19] and we used rules of mixtures to estimate the plate's effective modulus ($E = 544$ kPa). Permittivity constant is $\varepsilon_0 = 8.85 \times 10^{-12}$ Pa m^2/V^2 and the relative permittivity of VHB is reported as $\varepsilon = 3.21$ [19].

4.3.4 Fabrication of the microfluidic pump device

The bottom substrate was made of polyvinylsiloxane (PVS) (Elite double 32, Zhermack) and molded accordingly to define a cylindrical chamber matching the diameter of the conductive

PDMS electrodes. Then, a thin layer of uncrosslinked PVS was manually spread on the surface of the bottom substrate and the thin plate was placed on top to chemically bond the bottom substrate and the entire film except the circular actuation regime. Similarly, the top substrate with a cylindrical chamber and a micro-sized channel ($h = \mathcal{O}(50\,\mu\mathrm{m})$) was made from PVS and chemically bonded to the other side of the thin plate.

4.3.5 Measurements and data analysis

A pressure sensor (CPCL04D, Honeywell) was utilized to measure the pressure difference between the top and bottom chambers. A bidirectional miniature flow meter (HAF-BLF0050, Honeywell) was used to measure the air flow moving into or out of the channels. Images of the thin film deformed at different voltages were taken with EO cameras (EO-1312C, Edmund Optics Inc.) at a rate of 10 fps while a green laser line (LC532-5-3F, 532 nm/5 mW) indicated a desired cross section of the thin film. A LabVIEW code was developed to generate proper signals for controlling the high voltage amplifier (Trek20/20C, Trek Inc.). In addition, the code was able to sync and trigger the cameras while reading the output voltages of the power supply, pressure sensor, and flow meters. We also developed a MATLAB code and used the Image Processing Toolbox for extracting curvatures, creating 3D meshes, and calculating the geometrical flow rate, as indicated in the main text.

4.4 Modeling

The composite plate is prepared by biaxially stretching the DE and then bonding the solid electrodes to it. In addition to a significant thickness reduction which eventually lowers the actuation voltage, the prestrain mechanism improves the DE's stability against different failure modes, and enhances the voltage breakdown for this material.[24] The prestrain also leaves a residual stress σ_i in the DE. Applying a voltage V to the electrodes, which are clamped along their edges, induces a compressive Maxwell stress σ_e through the DE thickness, which initially reduces σ_i. Once the total radial stress, $\sigma_r = \sigma_e - \sigma_i$, exceeds the critical buckling stress for the clamped circular plate, it will deform out of the plane.

To examine the topography of the buckled plate, a laser line was imaged by a camera to record the deformations of the circular plate at different locations on its surface (Figure 4.2a). The lines remain unperturbed until the applied voltage generates a stress that exceeds the critical buckling stress of the plate. As the plate deforms out of the plane (Figure 4.2b), we extract the deformation profiles of each laser line via image processing (Figure 4.2c) to obtain a quantitative measure of the entire deformation of the plate (Figure 4.2d).

We determined the onset of buckling by measuring how the length of the line L along diameter changes as a function of V. We normalized L by the initial length of the cross section, L_0, and plotted it versus applied voltage in Figure 4.3a. The results show a sharp increase in L, corresponding to an out-of-plane deformation, around $V = 6.8$ kV. Changing the conditions surrounding the composite plate, such as the pressure above and below it (Figure 4.3b), has a dramatic effect on the post-buckled shape of the plate (Figure 4.3c), yet they appear to have no effect on the onset of buckling (Figure 4.3a).

We first seek to describe the onset of buckling when a voltage is applied to the thin plate. The relation between V and the radial strain e_r for a free-standing, thin plate is described by:

$$e_r \approx \frac{\varepsilon_o \varepsilon}{2E_d} \left(\frac{V}{h_d} \right)^2, \tag{4.1}$$

where E_d is the elastic modulus of the DE, ε_0 is the permittivity constant, ε is relative permittivity of the DE, h_d is the thickness of the dielectric layer, and V is the applied voltage [17]. We assume that near the buckling threshold the material is incompressible and elastic, therefore the applied voltage causes a stress in the radial direction in the form $\sigma_e \approx \frac{\varepsilon_o \varepsilon}{2(1-\nu^2)} \left(V/h_d\right)^2$, where $\nu \approx 0.5$ is the Poisson ratio of the DE. At the onset of buckling, the deflection of the plate is small relative to the plate thickness, so we use the linearized plate equations as an estimation of the critical buckling stress. A clamped, circular plate exposed to a radial compressive stress will buckle out of the plane when $(\sigma_r)_{cr} = \frac{kD}{R^2 h}$, where R is the plate's radius, $D = \frac{Eh^3}{12(1-\nu^2)}$ is the flexural rigidity, and k is a numerical factor that depends on the boundary conditions and the buckling mode; $k_1 = 14.68$ and $k_2 = 26.4$ for modes 1 and 2 of a clamped plate, respectively [26]. Considering both the residual stress and the voltage-induced stress, we estimate the critical voltage for plate buckling as:

$$V_c \approx h_d \left(\frac{k\,E}{6\ \varepsilon_o \varepsilon} \left(\frac{h}{R} \right)^2 + \frac{2\,(1-\nu^2)\,\sigma_i}{\varepsilon_o \varepsilon} \right)^{1/2}, \tag{4.2}$$

which is similar to linearized critical voltage equations reported in other studies.[27] We consider the effect of prestrain as an initial condition for this system, and use material properties measured after the applied prestrain. We expect that small deformations should result in a linear behavior, and therefore, this linearized theory will be accurate in describing the onset of buckling.* When $h/R \ll 1$, the critical voltage is dominated by the residual stress. For example, in our experiments $h/R \approx 0.03$, so the experimentally measured residual stress within the plate, $\sigma_i = \mathcal{O}(10^2 \text{ kPa})$, is significantly larger than the stress required to buckle an initially stress-free plate, $\sigma_c = \mathcal{O}(1 \text{ kPa})$. Since the applied voltage in this case mainly serves to reduce the residual stress in the dielectric film, we approximate the critical voltage by considering only the residual stress term. Neglecting numerical factors of order one, we find that for a thin, prestrained film with significant residual stress,

$$V_c \sim \sqrt{\frac{h_d^2 \sigma_i}{\varepsilon_0 \varepsilon}}. \tag{4.3}$$

Equation (4.3) predicts that the critical voltage for the composite plates shown in Figure 4.3 should be around $V_c = (4.8 \pm 0.9)$ kV, which deviates by about 25% from our experimentally observed value of $V_c \approx 6.8$ kV. Also, equation (4.3) suggests that the critical voltage should scale linearly with the film thickness. Experiments over a wide range of h will be necessary to verify this scaling, though this work is beyond the scope of the current article.

4.5 Discussion

While the above calculation is useful for determining the critical threshold for buckling, it says nothing about the post-buckled shape of the plate. The difference between the pressure and volume above and below the plate will control the post-buckled shape, which will, in turn, determine the structure's ability to move fluid within the microchannel. We can use the

*To consider nonlinear terms, one can use the Helmholtz free energy along with the neo-Hookean model to obtain the equation of state for equal-biaxial pre-stretching condition $-\sigma_i + \varepsilon\,\varepsilon_0 \left(\frac{V}{h_d}\right)^2 = \frac{E}{2(1+\nu)}\left(\lambda^2 - \lambda^{-4}\right)$,[20] where $\lambda = 1 + e_r$ is the total film stretch, and the changes in the film thickness caused by the electric field are neglected. Using stress-stretch relation in the neo-Hookean model, $\sigma_r = \frac{E}{2(1+v)}\left(\lambda^2 - \lambda^{-4}\right)$, and substituting the critical buckling stress $(\sigma_r)_{cr}$, we find an equation for V_c that is very similar to equation (4.2).

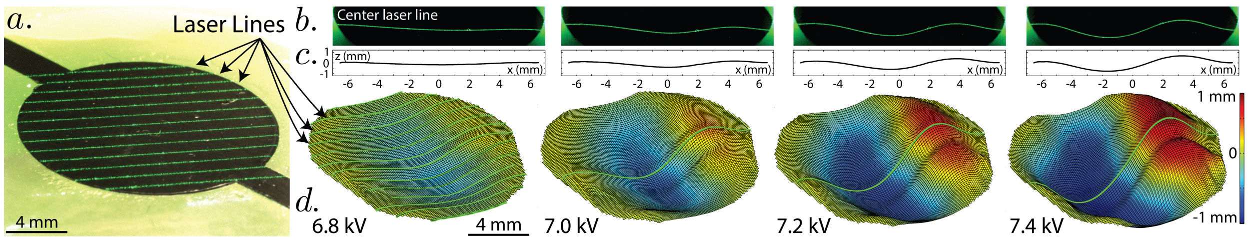

Figure 4.2: 3D surface reconstruction of the shape of the thin plate by taking and processing the images of different cross sections at different voltages. *a.* Overlaid images of the laser line at different cross sections when the voltage is zero. *b.* Raw images of the laser line for the middle cross section taken at different voltages. *c.* Extracted profiles of the images shown in part (*b*) using image processing. *d.* 3D surface profile of the thin plate at different voltages.

imaging technique demonstrated in Figure 4.2 to determine both the plate's buckling mode, and the expected fluid flow rate. Since the plate resides in a chamber of known dimensions (Figure 4.3b), integration of the volume above or below the 3D surfaces in Figure 4.3c allows us to define a geometrical flow rate, which gives a measure of the net volume change as a function of time for a given voltage. By assuming the flow is incompressible, this net volume change yields the fluid flow rate as a function of voltage. This geometrically derived flow rate was verified using both a flow meter and optical imaging. To determine the effect of chamber on the post-buckled plate's deformation, we embedded the plate in a controlled environment, and varied the surrounding pressure and volume. We identified three important regimes that determine the plate's deformation.

First, both sides of the plate are exposed to a constant pressure P_0, and reside within a closed chamber (Figure 4.3b-i). In this case, a mode two, asymmetric out-of-plane deformation was observed once the critical buckling threshold was reached (Figure 4.3c-i). The amplitude of the deformations increased with the voltage, and the mode two shape remained well into the post-buckling regime. Since this shape has an up-down symmetry about the horizontal axis, it does not move any fluid in the top chamber. This result was confirmed by observing that both the geometrical flow rate and the experimental flow rate from the flow meter measured zero flow (Figure 4.4a). This buckling mode can be easily understood by considering that the plate's surface area increases with the applied voltage, but any axisym-

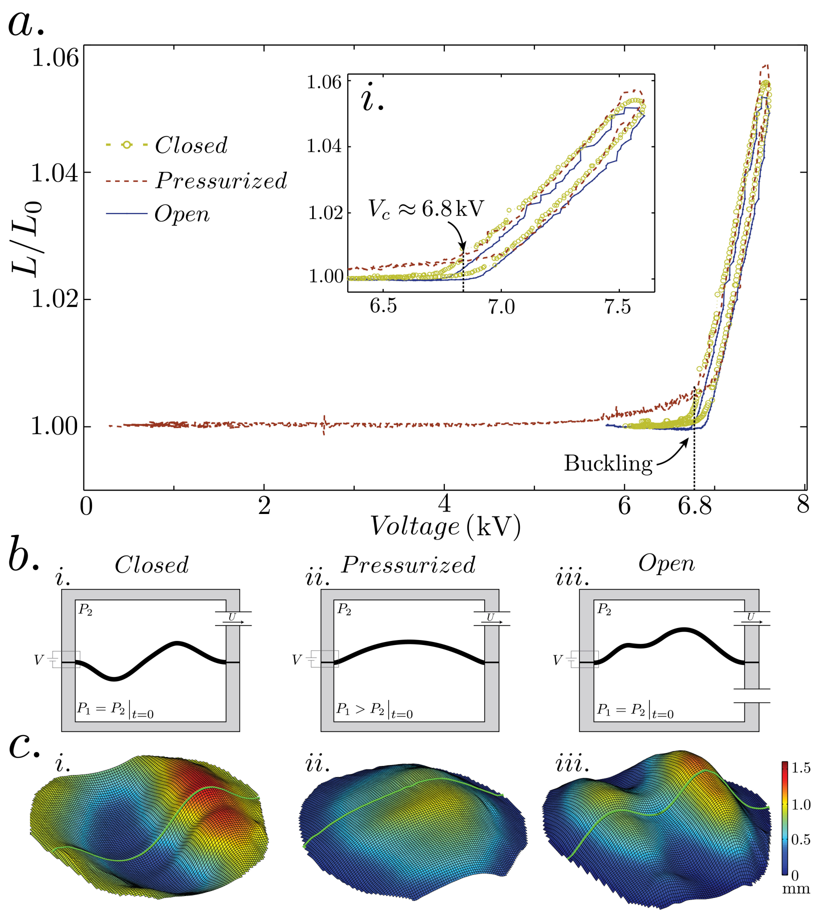

Figure 4.3: *a.* Changes in line length of the middle cross section normalized with the initial line length at zero voltage. The inset (same units) shows occurrence of the critical buckling voltage at which the line length starts changing linearly with the voltage. This critical buckling threshold appears to be independent of the pressure in the surrounding chambers. *b.* , *c.* Schematics and corresponding 3D profiles for the three modes of electrically induced deformation by varying volume and pressure above and below the thin plate: *i. Closed.* One chamber is closed but both chambers initially have the same pressure, *ii. Pressurized.* One chamber is closed and at a higher pressure *iii. Open.* Both sides are open and have the same pressure.

metric deformation would cause the chamber below the plate to be pressurized. Therefore, the minimal energy corresponds to an out-of-plane deformation with up-down symmetry, which will have a negligible change on the pressure in the closed chamber. To understand

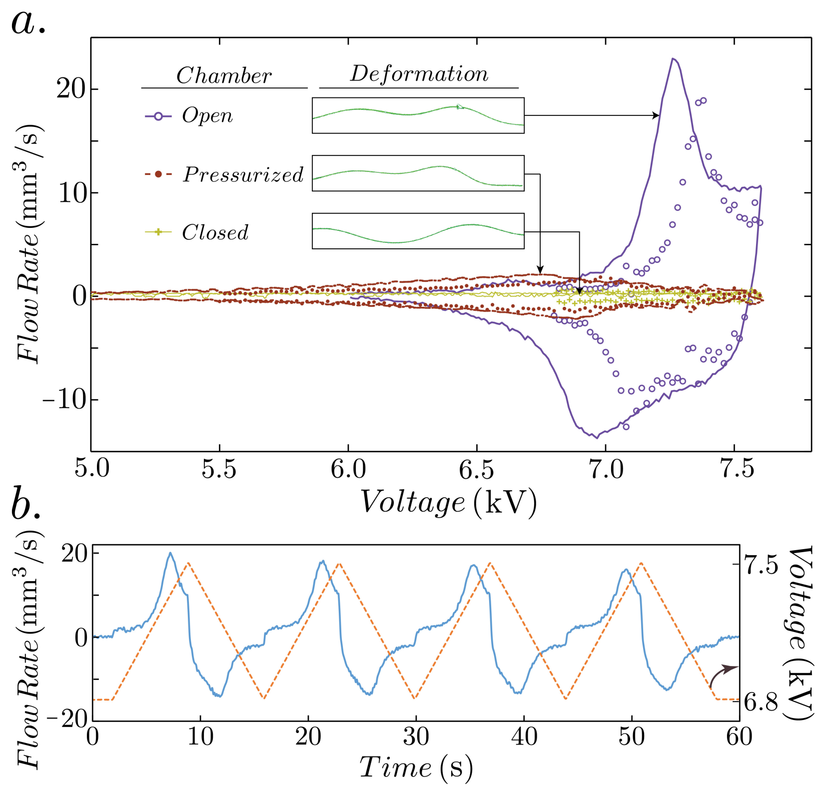

Figure 4.4: *a.* Flow rate as a function of voltage for different cases measured using a flow meter (lines) and estimated geometrically from 3D surface profiles (dots). The voltage was applied at a rate of 100 V/s for all cases. The flow rate of the 'open' case was an order of magnitude higher than the one of the 'pressurized' case while the 'closed' case resulted in zero flow rate. *b.* Cyclic flow rate of the pump, measured using a flow meter, for the 'open' case when the voltage stimulus was in the form of a triangle waveform oscillating between 6.8 kV and 7.5 kV. The pump showed a repeatable flow rate profile and the slight decrease in the maximum flow rate of different cycles can be related to viscoelastic effects of the plate. Note that for each cycle, we have a pumping mechanism followed by a suction that is useful for the pumping in the next cycle.

this effect, we consider that the bending energy of the plate scales as $U_b \sim Eh^3\kappa^2$, where κ is the curvature, and therefore the work done by bending has the form $W_b \sim Eh^3 R\,\kappa$. The work done by the pressure is $W_p = P\mathcal{V}$, where $\mathcal{V}$ is the volume change above or below the plate, which we estimate from the volume of a spherical cap $\mathcal{V} = (3R - w)\pi w^3/3 \sim R^4\kappa$

for a small cap height of w. The ratio of $W_b/W_P \sim (E/P)(h/R)^3 \sim 10^{-6}$ indicated that buckling of a thin plate is energetically more favorable than changing the pressure in the enclosed chambers. Therefore, the plate will spontaneously adopt a higher mode of buckling that does not necessitate a change in pressure in the surrounding chambers.

Second, we prescribe one chamber to be at a higher pressure than the other, *i.e.* $P > P_0$. A mode one, axisymmetric out-of-plane deformation is observed above the buckling threshold (Figure 4.3b-ii). We applied a positive initial pressure of $P \approx 500$ Pa to the bottom channel and increased the voltage linearly at a rate of 100 V/s to 7.6 kV. We observed a small deformation before reaching 6.8 kV, which has also been reported in previous studies [28, 29]; however, the thin film underwent significant deformation when the voltage exceeded 6.8 kV. The axisymmetry of the buckled plate, enabled by the pressure difference between the two chambers, results in a net positive flow out of the open chamber. We measured a flow rate that increases slowly with voltage until 6.8 kV, followed by a decrease afterward (Figure 4.4a).

Finally, we consider the case when both channels are open and exposed to air, so the pressure difference between two sides of the thin film is zero (Figure 4.3b-iii). In this case, a highly nonlinear, yet reproducible, shape emerged at the onset of buckling, and varied with increasing applied voltage. Exceeding 7.4 kV caused the entire thin plate to rapidly undergo a snap-through to compensate the further surface extension. These factors lead to a significant flow rate, at least one order of magnitude higher than the other two cases (Figure 4.4a). We suspect this response is because the deformation of the thin film is not restricted by changes in pressure of each chamber. Further study of coupled interactions between the fluid and the flexible plate may be necessary to fully characterize the effect of pressure on the buckling dynamics, which will be left as future work.

Both the shape of the buckled plate and the resulting fluid flow rate are dependent on the pressures in the chambers above and below it. Positive, directional flow was observed when one chamber is pressurized, or when both chambers are open to the atmosphere. Incorporating these concepts into the design of a microfluidic system provides a voltage-induced means for generating flow. As a demonstration of this pumping mechanism, we applied a voltage cycle and measured the flow rate as a function of time (Fig. 4.4b), which produced both pumping and suction within the channel.

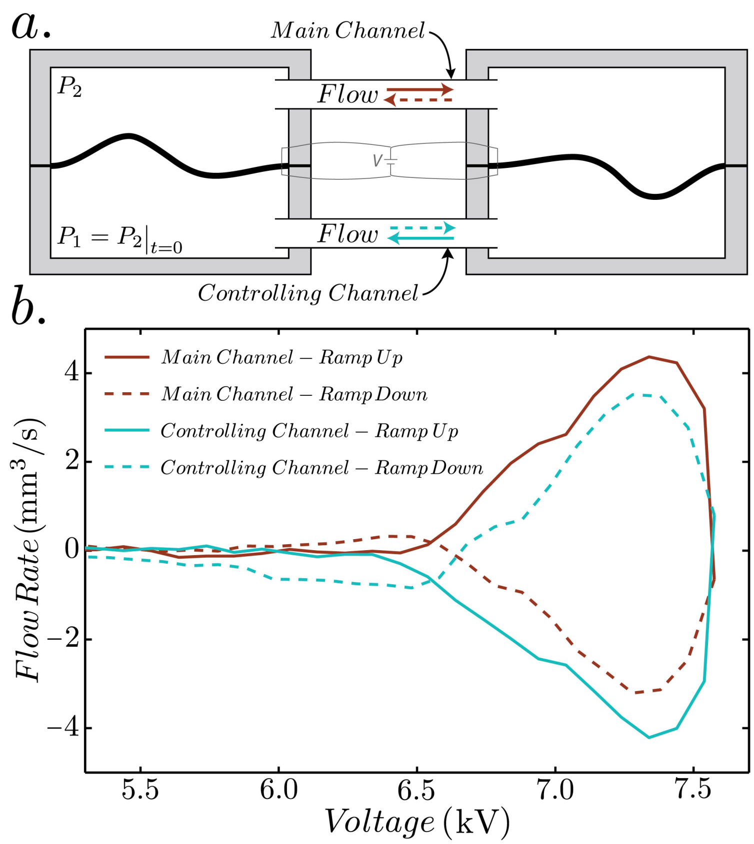

Figure 4.5: *a.* A schematic of combining two pumps in series; bottom channels are also connected to enhance the pumping action. *b.* When the left plate deforms, air is pulled out from the bottom channel from the right to the left pump, forcing the right plate to deform in the opposite direction and therefore pulling the air in the top channel in the reverse direction, from the left to the right and increasing the efficiency of pumping. This mechanism is reversed when decreasing the voltage to zero. The rate of change of voltage is 100 V/s.

4.6 Toward Coupling and Enhancement

Current microfluidic designs involve closed chambers with equal pressures - matching the scenario in which no flow was measured. To address this limitation, we provide a simple solution for generating flow by coupling multiple pumps. We consider two pumps that are connected in series, *i.e.* each pump is connected to one end of a microfluidic channel.

The bottom chambers of the pumps are also connected through the second "controlling" channel, to couple the pumping action (Figure 4.5a). Since we have a constant volume in the bottom channels, each pump operates similar to single pump with a closed chamber and same initial pressure, where the flow rate was zero. By applying the voltage, both plates buckle, but the deformation of one affects the deformation of the other. In fact, plates deform by pulling/pushing the air from one chamber to the next one without a need for changing the volume or pressure of the surrounding medium. Therefore, we observe higher flow rates due to the coupling of suction and pumping between these two pumps (Figure 4.5b). This effect is reversed when the voltage is decreased, providing a robust means for controllable bidirectional flows. Similar bidirectional flows have been observed in the heartbeat mechanism of the dorsal vessel in some insects, *e.g.* aperygotes and mayflies [30]. Note that this is a closed and isolated system where outside pressure does not play any role in plate deformation, so the flow rate of this system is most comparable to the one of a 'closed' pump discussed above, which shows a significant increase in the flow rate. The versatility of the advanced material design that we present allows these pumps in series or in parallel to enable bidirectional flows and microfluidic vacuum pumps with enhanced flow rates.

4.7 Conclusions

We presented the voltage-induced out-of-plane deformation of a confined dielectric thin plate, and utilized this mechanism as a means to pump fluids within microchannels. We prepared elastic electrodes that are flexible, and can be in direct contact with fluid. In addition to the applied voltage, we considered the effect of pressure and volume on the deformation of the thin plate. The change in surface area depends on the voltage, while the deformation shape, which significantly affects the flow rate, is a function of voltage, pressure, and volume. The flow rate was observed to be as high as 20 mm^3/s. These pumps can also be utilized in series and/or parallel in order to enhance the flow rate, or add advanced functionality such as microchannel vacuums or bidirectional fluid flow. These steps will open new avenues for microfluidic systems where a low power consumption pump with a tunable flow rate can easily be integrated.

References

[1] T. Thorsen, S. J. Maerkl, and S. R. Quake. "Microfluidic large-scale integration". In: *Science* 298.5593 (2002), pp. 580–584.

[2] H. A. Stone, A. D. Stroock, and A. Ajdari. "Engineering flows in small devices: Microfluidics toward a lab-on-a-chip". In: *Annual Review of Fluid Mechanics* 36 (2004), pp. 381–411.

[3] P. Tabeling. *Introduction to microfluidics*. Oxford University Press, 2005. ISBN: 0198568649.

[4] D. C. Leslie, C. J. Easley, E. Seker, J. M. Karlinsey, M. Utz, M. R. Begley, and J. P. Landers. "Frequency-specific flow control in microfluidic circuits with passive elastomeric features". In: *Nature Physics* 5.3 (2009), pp. 231–235.

[5] D. P. Holmes, B. Tavakol, G. Froehlicher, and H. A. Stone. "Control and manipulation of microfluidic flow via elastic deformations". In: *Soft Matter* 9.29 (2013), pp. 7049–7053.

[6] J. C. Eijkel and A. Van Den Berg. "Nanofluidics: what is it and what can we expect from it?" In: *Microfluidics and Nanofluidics* 1.3 (2005), pp. 249–267.

[7] R. B. Schoch, J. Han, and P. Renaud. "Transport phenomena in nanofluidics". In: *Reviews of Modern Physics* 80.3 (2008), p. 839.

[8] T. Fujii. "PDMS-based microfluidic devices for biomedical applications". In: *Microelectronic Engineering* 61 (2002), pp. 907–914.

[9] H. Andersson and A. Van den Berg. "Microfluidic devices for cellomics: a review". In: *Sensors and Actuators B: Chemical* 92.3 (2003), pp. 315–325.

[10] J. O. Tegenfeldt, C. Prinz, H. Cao, R. L. Huang, R. H. Austin, S. Y. Chou, E. C. Cox, and J. C. Sturm. "Micro-and nanofluidics for DNA analysis". In: *Analytical and Bioanalytical Chemistry* 378.7 (2004), pp. 1678–1692.

[11] R. Fair. "Digital microfluidics: is a true lab-on-a-chip possible?" In: *Microfluidics and Nanofluidics* 3.3 (2007), pp. 245–281.

[12] M. Abdelgawad and A. R. Wheeler. "The digital revolution: a new paradigm for microfluidics". In: *Advanced Materials* 21.8 (2009), pp. 920–925.

[13] G. M. Whitesides. “What Comes Next?” In: *Lab on a Chip* 11.2 (2011), pp. 191–193.

[14] W. Wu, A. DeConinck, and J. A. Lewis. “Omnidirectional Printing of 3D Microvascular Networks”. In: *Advanced Materials* 23.24 (2011), H178–H183.

[15] F. Carpi, S. Bauer, and D. De Rossi. “Stretching Dielectric Elastomer Performance”. In: *Science* 330.6012 (2010), pp. 1759–1761.

[16] R. E. Pelrine, R. D. Kornbluh, and J. P. Joseph. “Electrostriction of polymer dielectrics with compliant electrodes as a means of actuation”. In: *Sensors and Actuators A: Physical* 64.1 (1998), pp. 77–85.

[17] R. Pelrine, R. Kornbluh, Q. Pei, and J. Joseph. “High-Speed Electrically Actuated Elastomers with Strain Greater Than 100%”. In: *Science* 287.5454 (2000), pp. 836–839.

[18] Z. Suo. “Mechanics of stretchable electronics and soft machines”. In: *MRS Bulletin* 37.03 (2012), pp. 218–225.

[19] M. Bozlar, C. Punckt, S. Korkut, J. Zhu, C. C. Foo, Z. Suo, and I. A. Aksay. “Dielectric elastomer actuators with elastomeric electrodes”. In: *Applied Physics Letters* 101.9 (2012), pp. 091907–5.

[20] T. Lu, J. Huang, C. Jordi, G. Kovacs, R. Huang, D. R. Clarke, and Z. Suo. “Dielectric elastomer actuators under equal-biaxial forces, uniaxial forces, and uniaxial constraint of stiff fibers”. In: *Soft Matter* 8.22 (2012), pp. 6167–6173.

[21] J.-S. Plante and S. Dubowsky. “Large-scale failure modes of dielectric elastomer actuators”. In: *International Journal of Solids and Structures* 43 (2006), pp. 7727–7751.

[22] X. Zhao and Z. Suo. “Theory of Dielectric Elastomers Capable of Giant Deformation of Actuation”. In: *Physical Review Letters* 104.17 (2010), p. 178302.

[23] Z. Suo. “Theory of dielectric elastomers”. In: *Acta Mechanica Solida Sinica* 23.6 (2010), pp. 549–578.

[24] B. Li, H. Chen, J. Qiang, S. Hu, Z. Zhu, and Y. Wang. “Effect of mechanical pre-stretch on the stabilization of dielectric elastomer actuation”. In: *J. Physics D: Applied Physics* 44.15 (2011), p. 155301.

[25] R. Shankar, T. K. Ghosh, and R. J. Spontak. “Dielectric elastomers as next-generation polymeric actuators”. In: *Soft Matter* 3.9 (2007), pp. 1116–1129.

[26] P. Bulson. *The Stability of Flat Plates*. Chatto and Windus, 1970.

[27] S. Rosset, M. Niklaus, P. Dubois, and H. R. Shea. “Mechanical characterization of a dielectric elastomer microactuator with ion-implanted electrodes”. In: *Sensors and Actuators A: Physical* 144.1 (2008), pp. 185–193.

[28] V. Rocco, F. Antonio, B. Massimo, C. Federico, F. Gabriele, and R. Danilo De. “Modeling and experimental validation of buckling dielectric elastomer actuators”. In: *Smart Materials and Structures* 21.9 (2012), p. 094005.

[29] S. Rosset, M. Niklaus, P. Dubois, and H. R. Shea. “Large-Stroke Dielectric Elastomer Actuators With Ion-Implanted Electrodes”. In: *J. Microelectromechanical Systems* 18.6 (2009), pp. 1300–1308.

[30] M. W. Westneat, J. J. Socha, and W.-K. Lee. “Advances in biological structure, function, and physiology using synchrotron X-ray imaging”. In: *Annu. Rev. Physiol.* 70 (2008), pp. 119–142.

Chapter 5

Fluidic Electrodes: Toward Miniaturization, Higher Frequencies, and Lower Voltages

5.1 Abstract

Accurate and integrable control of different flows within micro channels is crucial to further development of micro devices and lab-on-chip applications. In this chapter, we introduce a flexible micro actuator that undergoes buckling at a high deformation rate and disturbs the nearby fluid flows. The actuator consists of a confined, thin, dielectric film that buckles out of the plane when exposed to a certain voltage through conductive fluid electrodes. Similar to the previous chapter, we offer a model to estimate the onset of the critical buckling voltage. The buckling shape of this micro actuator is obtained using image processing techniques. We then investigate the effects of buckling frequency, flow rate, and the pressure difference between the two sides of the thin film, on the functionality of the micro actuator and on the disturbance of the adjacent flow. This simple mechanism provides a fast, repeatable, and robust means to control or disturb fluids within microfluidic devices.

5.2 Introduction

Microfluidic devices have become primary tools in many applications to control and monitor variety of parameters [1–3]. Further development and utilization of Lap-on-a-Chip (LoC) devices are associated with the design of a fully stand-alone system capable of accurately and appropriately controlling different flows within microchannels while keeping the the cost low. Numerous studies have been conducted to develop variety of valves [4] and pumps [5, 6] that are appropriate for specific micro systems, the majority of which need difficult techniques for fabrication [2] or extensive external equipment during the testing to control different parameters. Among all, Quake NanoFlex^{TM} valves [7, 8] are shown to be efficient, easy to fabricate, and reliable to work; however, running these valves at very high frequencies may not be feasible due to the intrinsic time lag of pneumatic signals. In this study, we introduce a micro actuator that operates using an electric signal, which minimizes the time lag, and works at very high frequencies. The latter advantage enables us to observe the effect of buckling frequency on the disturbance of the fluid flow and study the fluid-soft solid interaction. Similar to the previous chapter, we use the buckling instability of a thin, dielectric film for actuation, but significantly increase the frequency of actuation by replacing flexible electrodes with fluid ones.

Common dielectric actuators usually consist of a dielectric film sandwiched between two electrodes [9]. When the dielectric film is exposed to an electric field, its thickness reduces and therefore its surface area increases because of the film incompressibility [10, 11]. If clamped from its edges, the film cannot extend and at a critical voltage, it undergoes buckling instability [12]. This out-of-plane deformation is used towards disturbing the adjacent flows.

Different type of electrodes and techniques have been utilized to apply a voltage to the dielectric film [13]. Gel electrodes are used in robotic applications for structures that do not undergo large deformations nor become in contact with liquids. On the other hand, compliant solid electrodes, such as CB-PDMS [11] and ionic elastomers [14], are reliable, have great compatibility with fluids, and undergo significant deformations; however, it is difficult to reduce the thickness of this type of electrodes and therefore the total thickness of the composite actuator. Studies have also been conducted to make a superficial layer of the dielectric film conductive using ion-bombardment techniques [15], which make the film

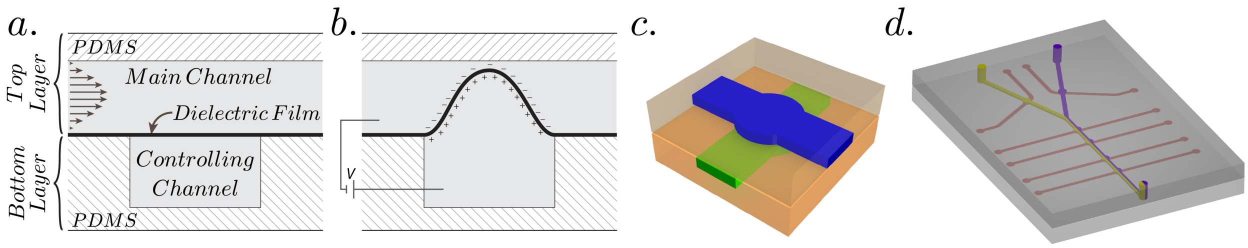

Figure 5.1: *a.* A schematic of micro actuator that disturbs nearby fluid flows. The dielectric film separates the crossed top and bottom channels. The main channels are all grounded. *b.* By applying adequate positive electrical signal to one of the controlling channels, the thin film between that channel and the crossing top channel undergoes out-of-plane buckling. We use this buckling for controlling the flow within the main channel. *c.* A 3D schematic of a section of the device showing the main (blue) and controlling (green) channels, which are separated by the thin dielectric film. *d.* a 3D schematic of the device showing different micro actuators at the intersections of top and bottom channels.

stiffen and thus deform less.

5.3 Design of Experiment

5.3.1 Approach

We use conductive fluids as electrodes to apply a voltage to a dielectric film. Fluid electrodes do not restrict the dielectric film's deformation nor add any thickness to the total thickness of the actuating mechanism. Therefore, the film undergoes faster and larger deformations at lower voltages. In addition, the entire system can now be miniaturized and embedded into a micro channel while the fabrication is significantly easier than those of gel and soft solid electrodes. These unique features make fluid electrodes very suitable for applications requiring high frequency and large deformations.

This microactuating device has three layers: The top layer contains 'main channels,' whose flows are going to be controlled; the bottom layer has embedded 'control channels' that are used to send the actuation signal; and the dielectric film that separates the main and control channels (Figure 5.1a). The main channels are grounded to reduce the risk of any damage to components sensitive to electric potential, such as living cells and colloidal particles. Since the channels are filled with electrically conductive fluids, e.g. salt water, applying a voltage to a pair of one main and one control channel creates an electric field within the dielectric film, which generates Maxwell stresses, and at a critical voltage, the film deforms out of the plane, resulting in a constriction that disturbs the fluid (Figure 5.1b).

5.3.2 Fabrication

The thin film was prepared by spin coating ploydimethylsiloxane (PDMS) (Dow Corning Sylgard 184) on a Silicon wafer with the spin speed and time varied to control the film thickness ($h = \mathcal{O}(40\mu\text{m})$), and then curing it at 90 °C for 5 min. The molds for top and bottom layers were prepared first by patterning the main and control channels on a Silicon wafer via photo lithography techniques and then etching the wafer using Deep Reactive Ion Etching (DRIE) technique. We then made the bottom and top layers by casting PDMS onto molds and curing them at 120 °C for 1 hr. Next, we bond the thin film to the top layer using a Corona treater (Laboratory Cronoa Treater, UV Process Supply Inc). The Bottom layer was also exposed to corona plasma for about 1 minute, aligned under microscope, and bonded to the free side of the thin film.

5.3.3 Experimental setup

The fluid electrode solution was prepared by dissolving 20% NaCl salt (Kroger) into distilled water (Kroger) at 90 °C. We then added water soluble dyes to the saltwater solution to differentiate the flows in different channels. The electrical conductivity of all solutions was very high ($> 200 mS/cm$ measured using Hanna Instruments HI2003 - Edge). The sample was mounted on a hand made x-y-z stage, and we used a microscopic lens (Navitar Zoom 6000) attached to a Nikon D610 camera to take images and movies of an area of interest from top view. The main channels were all grounded while one control channel at a time was connected to the high voltage signal generated using a high voltage amplifier (Trek 20/20C-HS). We used LabVIEW to generate low voltage signals for controlling the high voltage amplifier, and track the voltage and the current via an NI DAQ System (NI cDAQ-9174 with NI 9205 and NI 9269). The fluid in control channels was stationary while the flow in main channels was pressure driven, simply via raising a reservoir to a certain height. The pressure difference between the control and the main channels was also applied by relatively elevating or lowering the corresponding reservoirs.

5.4 Modeling

To estimate the onset of critical buckling voltage, we start with the linearized relation between the radial strain, e_r and the applied voltage, V as follows [9]:

$$e_r \approx \frac{\epsilon_0 \epsilon}{2E} \left(\frac{V}{h} \right)^2 \tag{5.1}$$

where ϵ is the permittivity constant, ϵ_0 is the relative permittivity of the dielectric film, h is the film thickness, and E is the film's elastic modulus. Using the constitutive relations [16], we have the radial stress, $\sigma_r \approx \frac{\epsilon_0 \epsilon}{2(1-\nu^2)} \left(V/h \right)^2$. Then we use linearized plate theory to estimate the critical stresses at which the buckling occurs [17, 18]: $\sigma_{cr} = \frac{k\,D}{R^2 h}$ where $D = \frac{E\,h^3}{12(1-\nu^2)}$ is the bending stiffness, ν is Poisson's ration, R is the film diameter, and k is a series of constant coefficients for different buckling modes, e.g., $k_1 = 14.68$ and $k_2 = 26.4$ for the first and second buckling modes. By substituting the radial stress into the critical stress equation, we have:

$$V_c \approx h \left(\frac{k\,E\,h^2}{6\,\epsilon_0 \epsilon\,R^2} \right)^{\frac{1}{2}} \tag{5.2}$$

For example, here are the measured parameters for one of our fabricated devices: $h \approx 45\,\mu\text{m}, R = 475\,\mu\text{m}, \epsilon \approx 3, \epsilon_0 = 8.85 \times 10^{-12}$ Pa m^2/V$^2, k = 26.4,$ and $E = 1.2$ MPa. Equation (5.2) therefore estimates that $V_c \approx 3.2$ kV, which is in agreement with the experimentally measured critical voltage of $V_c \approx 3.3$ kV for that particular device. We note that equation (5.2) is very sensitive to the film thickness so it must be used only for a coarse estimation of the critical voltage if proper techniques are not available to accurately measure the film thickness.

5.5 Results and Discussion

By applying an adequate voltage to a control channel, while connecting the main channel to the ground, the circular intersection of that control channel with the main channel buckles out of the plane. This deformation is evidenced by two methods, one suggesting the shape of buckling deformation and the other one revealing the complex interaction between the soft film and nearby fluid.

5.5.1 Qualitative determination of the buckling shape

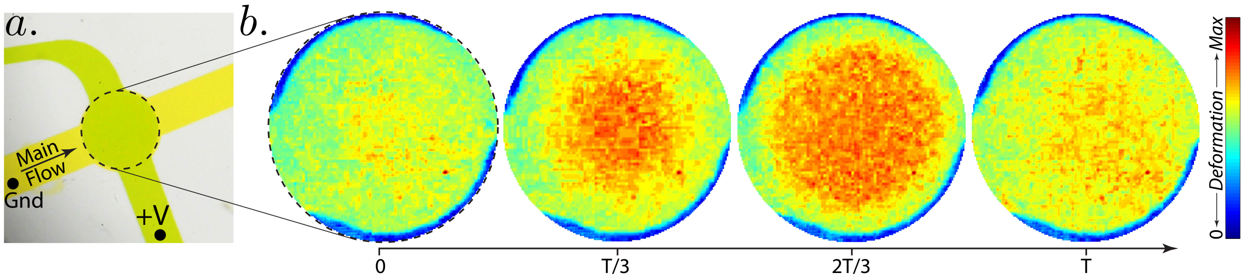

Figure 5.2: *a.* Top view of the device showing the micro actuator, the circular intersection of the main and the control channels *b.* 3D patterns of buckling deformations of the micro actuator in one cycle.

First, we take pictures of the circular intersection between the main and the control channels from the top view (Figure 5.2a) and use image processing techniques to estimate the shape of the buckled thin film. By turning the voltage on, the circular intersection actuates and deforms out of the plane, making a constriction within the channel. On the other hand, the intensity of the fluid color depends on the fluid height at each point. Therefore, we intent to determine the buckling shape of this micro actuator by tracking the changes in the intensity of the fluid from the top view. These intensity changes might not be visible to naked eyes, as the out-of-plane deformation for the actuators at this scale is on the order of 25 μm. However, the image processing techniques enable us to track small intensity changes and relate them to the film's deformation, thus obtaining a 3D deformation pattern. Figure 5.2b shows that the thin film is relatively flat - with a negligible concave pattern - at the beginning of a cycle, when the voltage is off. As the voltage increases, the concave pattern grows gradually but reaches its maximum at about 2/3 of the cycle, followed by a quick return to its initial shape as soon as the voltage goes back to zero. This is consistent with previously reported results of a similar case [12]. We note that this method provides a qualitative measure of changes in the buckling shape of such a small plate as a function of voltage or other parameters while the second method, discussed below, is used to estimate the amount of deformation.

5.5.2 Estimation of buckling deformation and flow changes

We study the micro actuator's deformation indirectly via its interaction with the adjacent fluid, which is evidenced by the the changes in flow ratios at the two fluids' interface (Figure 5.3a). When the micro actuator buckles out of the plane, it affect the flow in the corresponding channel, which consequently changes the ratio of two fluids and moves the interface up or down accordingly. We obtain the interface between two fluids using image processing techniques (Figure 5.3b) and estimate the changes in the ratio of one flow, for example, the yellow flow, by averaging the ratio of that flow over a narrow bandwidth shown in Figure 5.3b. We run each experiment for several cycles to improve the consistency of results (Figure 5.3c). In addition, we let the film relaxed for one second before switching to the next frequency test. This relaxation time is at least 3 orders of magnitudes longer than the time required for charging and discharging the micro actuator.

We note that the mechanism of interaction between the thin film and the adjacent fluid has four major steps during one voltage cycle. The first one is an equilibrium state where the voltage is zero (Figure 5.3c-i); the film is insignificantly deformed by the fluid flow over the film, and the flow is lightly controlled by the deformed thin film. Since both changes are minor for the current experiments, we simply assume that both the film deformation and the flow changes are negligible. By increasing the voltage, however, the thin film deforms significantly into the channel, causing a momentary increase in the flow of that channel while the changes in the main flow are still not comparable to that increase by the film's deformation (Figure 5.3c-ii). At some point, the reduction in the pressure driven flow due to the film's deformation becomes dominant and the flow increase caused by the film deformation into the channel can no longer compensate it (Figure 5.3c-iii). At this step, we may observe another equilibrium state if the voltage is kept constant. In the last step, the voltage is reduced to zero and the film tends to go back to its original shape but the coupling

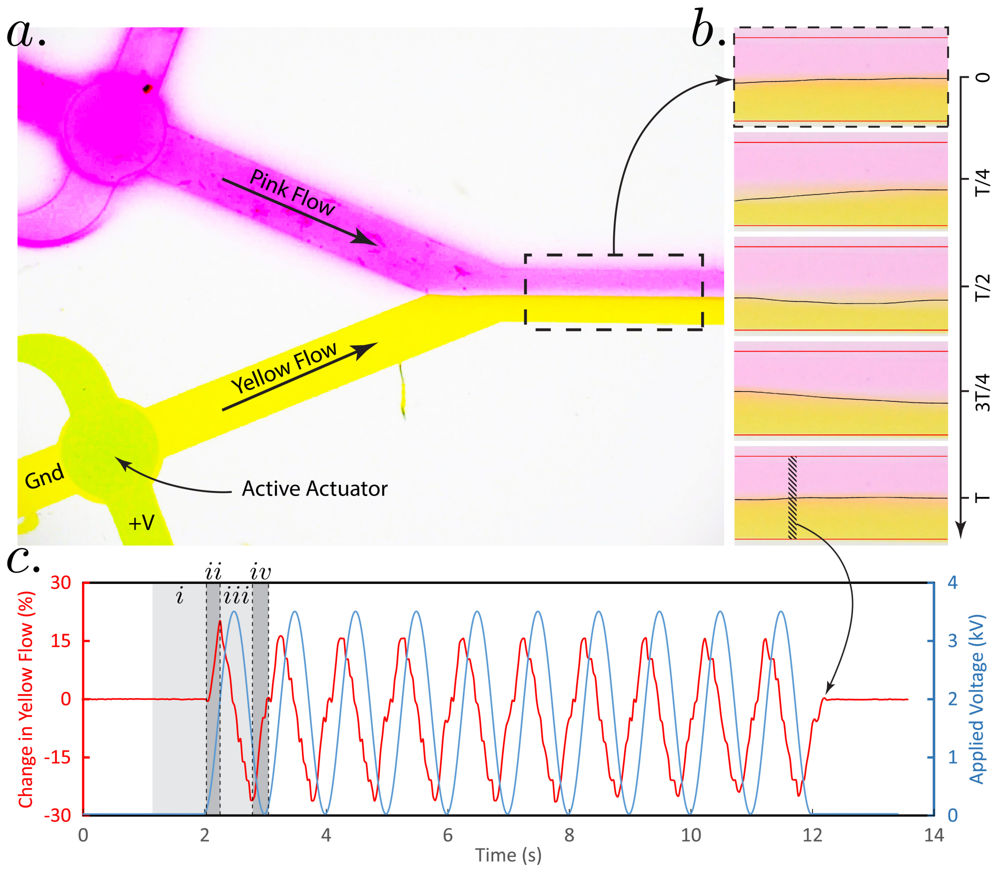

Figure 5.3: *a.* Two pressure driven flows merging into one channel *b.* Sequences of images showing the disturbance of two fluids' interface caused by the micro actuator. Extracting the interface and the channel's walls is done using image processing and the results are overlaid on top of the raw images. *c.* Changes in the ratio of yellow flow when the voltage is oscillating at a rate of 1 Hz. $i - iv$ bands demonstrate four different stages of coupling between the thin film's deformation and changes in fluid flow.

between film's deformation and flow changes plays a significant role in reducing the film's deformation and increasing the flow smoothly to the original equilibrium state. By repeating the voltage cycle, we observe the same interaction behavior although the maximum change in flow becomes more consistent usually after the second cycle.

When the micro actuator buckles into the channel, the interface between two fluids adapts a shape with a maximum (Figure 5.4a) that propagates through the channel while the wave amplitude attenuates. The later phenomenon, which can be treated similar to the attenuation of surface waves within viscous fluids [19, 20], suggests that the interface amplitude and its location can more accurately be obtained at the beginning of merging the two channels. We use changes in the amplitude's location to estimate the flow rate within the main channels due to the applied pressure. To reduce any contribution of higher-frequency actuations on the fluid disturbances (Figure 5.4b), we first focus on the tests run at 1 Hz to obtain the flow rate and the film deformation. The accuracy of results at higher frequencies will be improved by using a high speed camera along with more advanced devices to apply a constant pressure.

We then track the location of the maximum amplitude within each voltage cycle and compare it to adjacent frames to estimate the flow rate (Figure 5.4c), which be used as the primary variable to plot other parameters. The fluid viscosity of solution in the main channel was 1.8 mPa.s (Vibro Viscometer SV-10) and its density, measured by weighing 30 ml of fluid using an analytical balance (Sartorius Practum 124), was 1120 kg/m^3. Knowing the geometry of the channel ($h = 50\,\mu$m and $w = 500\,\mu$m), $\mathcal{R}e$ will be 0.04, 0.45, and 0.66 for $P_{applied} = 250,\ 800,$ and 1600 Pa, respectively.

We also measure changes in the maximum amplitude and plot them versus the estimated pressure driven flow rate (Figure 5.4d). As we expect, increasing the rate of pressure driven flows causes a decrease in the maximum amplitude as it becomes more difficult for the yellow fluid to disturb the other flow and permeate the pink fluid. The change in the maximum amplitude alone is not adequate to establish a relation between the film deformation and fluid flow. For example, a disturbance wave with high amplitude but short wavelength may represent the same amount of fluid volume as a disturbance wave with low amplitude but long wavelength. Therefore, we intend to obtain the persistence length, the maximum length of a disturbed interface (Figure 5.4e), These results show that disturbing a medium range flow may result in the longest persistence length.

We estimate the area under the disturbed interface bounded between zero and the persistence length using a MATLAB script. Assuming that the interface does not significantly change across the height of these channels ($h = \mathcal{O}(50\mu\text{m})$), the fluid volume permeated the second fluid due to the thin film's deformation is then estimated by multiplying the surface area by the channel height (Figure 5.4f). The results demonstrate that the thin film undergoes

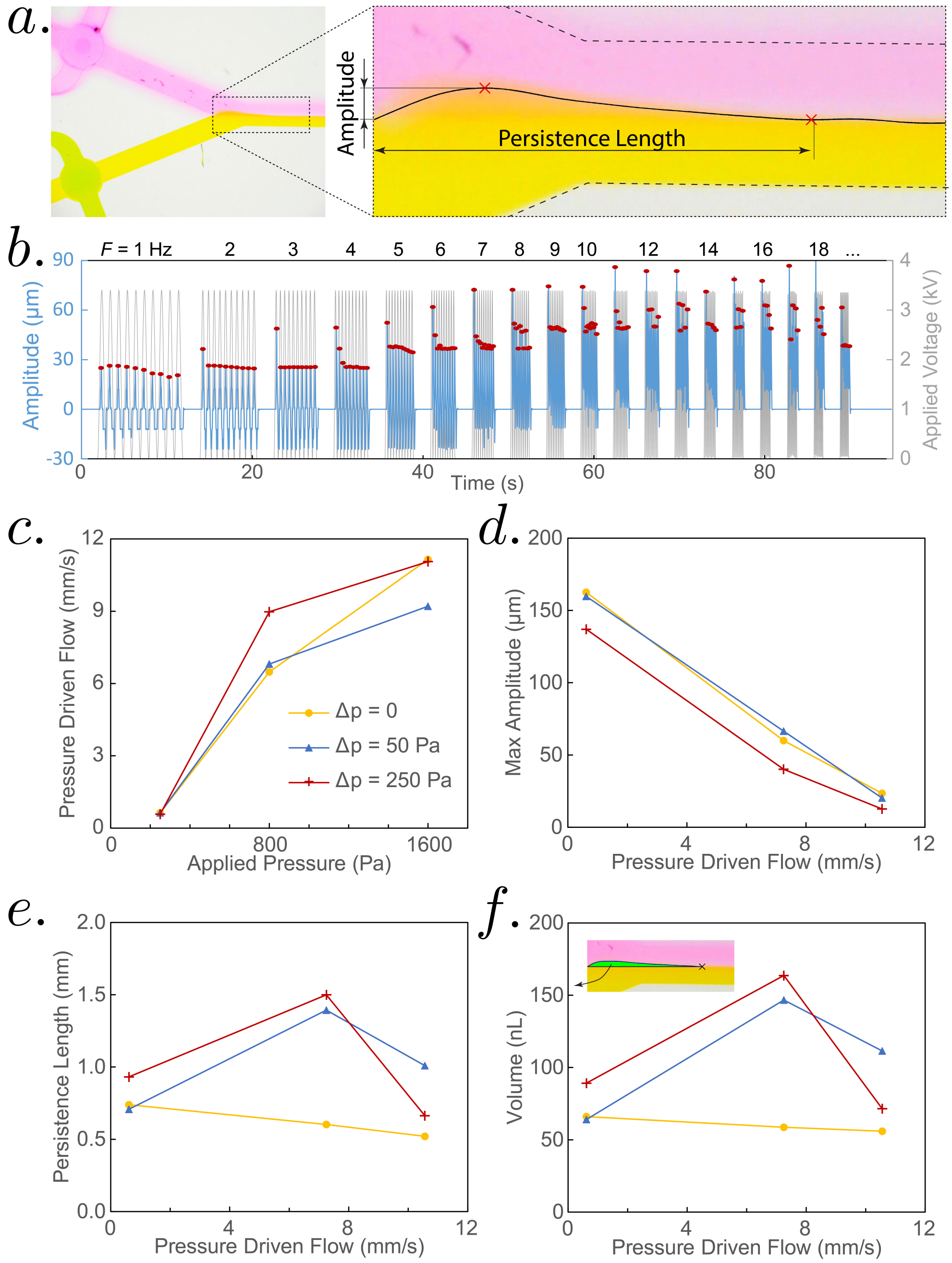

Figure 5.4: *a.* A disturbed interface between two fluids at the beginning of merging point. *b.* Change in the amplitude of disturbed interface plotted for different frequencies. Maximum amplitudes per each voltage cycle are shown in red dots. *c.* The rate of pressure driven flow as a function of applied pressure, measured by tracking the changes in the location of maximum amplitude using image processing. *d.-f.* Changes in the maximum amplitude, persistence length, and the volume of disturbed fluid as a function of measured flow rate. Only data corresponding to F = 1 Hz were used to calculate the parameters shown in *c-f*. The four *c-f* plots also share the same legend.

more buckling when the fluid flow is not too low or too high. When the flow is high, it costs a lot of energy for the thin film to move the fluid so it might be energetically more favorable for the thin film to deform less or undergo higher, but asymmetric buckling modes [12]. On the other hand, a regular flow over the thin film may help it to deform more, similar to the deformation of flexible tubes due to their inner flows [21, 22]. We note again that the determination of persistence length significantly affects the estimation of disturbed volume; further investigation is therefore required to verify the trend for other cases, *e.g.* when $\Delta p \approx 0$.

Based on the 3D patterns of deformation, we assume that the thin film undergoes the first buckling mode when $\Delta p = 800$ Pa or $\Delta p = 1600$ Pa. Therefore, the amount of fluid moved by the film at its maximum deformation can be estimated from the volume of a spherical cap $\mathcal{V} = (3R - w)\pi w^3/3$ where $R = 500\,\mu$m is the plate radius, $\mathcal{V}$ is the fluid volume estimated from Figure 5.4f and w is the maximum buckling deformation of the thin film. For example, when the pressure driven flow rate is about 0.6 mm/s, the average fluid volume moved by the thin film is about 70 nL. Using the above equation, we then estimate that the maximum deformation of the thin film under such condition is about 36 μm, which in fact seems to be very reasonable compared to the channel height of 50 μm.

These micro actuators can work in series and parallel for further advanced functionality, e.g., bidirectional flows, or for more efficiently enhancing (pumping) or controlling (valving) different flows within micro channels. Controlling the flow can significantly be improved by fabricating the main channel with a semicircular cross section. Unlike other types of electrodes, electrical conductivity of fluid electrodes does not decrease by stretching the dielectric film, resulting in a consistent, large actuation. Since we use highly conductive fluid electrodes, the majority of the voltage drop occurs within the thin film. However, if an experiment needs low conductive fluid electrodes or there are particles and cell very sensitive to voltage application, we suggest a secondary channel coupled with the main channel would shield the fluid any applied voltage. For instance, the voltage applied to one actuator deforms into the secondary channel, which in turn causes the passive micro actuator to partially close the main channel without any electricity involved.

5.6 Conclusions

We presented a new means to disturb and control fluid flow using the buckling deformation of a micro actuator that consists of a thin dielectric film. We used fluid electrodes to aid in voltage application to the dielectric film, which reduced the critical buckling voltage and significantly enhanced the rate of deformation. The buckling shape of the micro actuator was qualitatively obtained via tracking intensity changes within dyed fluids. We showed that the disturbed interface between two fluids can be utilized to characterize the interaction between the soft actuator and corresponding fluid, resulting in estimations of fluid flow and the film's deformation. The pressure difference between the main and control channels may affect the buckling shape while the applied pressure and consequently the pressure-driven flow may considerably alter the film's deformation. These micro actuators may play a significant role in the development of stand-alone microfluidics where a fast and robust means is required to control different flows within micro channels.

References

[1] G. M. Whitesides. "The origins and the future of microfluidics". In: *Nature* 442.7101 (2006), pp. 368–373.

[2] D. Mark, S. Haeberle, G. Roth, F. von Stetten, and R. Zengerle. "Microfluidic lab-on-a-chip platforms: requirements, characteristics and applications". In: *Chemical Society Reviews* 39.3 (2010), pp. 1153–1182.

[3] G. M. Whitesides. "What Comes Next?" In: *Lab on a Chip* 11.2 (2011), pp. 191–193.

[4] K. W. Oh and C. H. Ahn. "A review of microvalves". In: *Journal of Micromechanics and Microengineering* 16.5 (2006), R13.

[5] D. Laser and J. Santiago. "A review of micropumps". In: *Journal of micromechanics and microengineering* 14.6 (2004), R35.

[6] B. D. Iverson and S. V. Garimella. "Recent advances in microscale pumping technologies: a review and evaluation". In: *Microfluidics and Nanofluidics* 5.2 (2008), pp. 145–174.

[7] M. A. Unger, H.-P. Chou, T. Thorsen, A. Scherer, and S. R. Quake. “Monolithic Microfabricated Valves and Pumps by Multilayer Soft Lithography”. In: *Science* 288.5463 (2000), pp. 113–116.

[8] J. Melin and S. R. Quake. “Microfluidic large-scale integration: the evolution of design rules for biological automation”. In: *Annu. Rev. Biophys. Biomol. Struct.* 36 (2007), pp. 213–231.

[9] R. E. Pelrine, R. D. Kornbluh, and J. P. Joseph. “Electrostriction of polymer dielectrics with compliant electrodes as a means of actuation”. In: *Sensors and Actuators A: Physical* 64.1 (1998), pp. 77–85.

[10] R. Pelrine, R. Kornbluh, Q. Pei, and J. Joseph. “High-Speed Electrically Actuated Elastomers with Strain Greater Than 100%”. In: *Science* 287.5454 (2000), pp. 836–839.

[11] M. Bozlar, C. Punckt, S. Korkut, J. Zhu, C. C. Foo, Z. Suo, and I. A. Aksay. “Dielectric elastomer actuators with elastomeric electrodes”. In: *Applied Physics Letters* 101.9 (2012), pp. 091907–5.

[12] B. Tavakol, M. Bozlar, C. Punckt, G. Froehlicher, H. A. Stone, I. A. Aksay, and D. P. Holmes. “Buckling of dielectric elastomeric plates for soft, electrically active microfluidic pumps”. In: *Soft matter* 10.27 (2014), pp. 4789–4794.

[13] P. Brochu and Q. Pei. “Advances in Dielectric Elastomers for Actuators and Artificial Muscles”. In: *Macromolecular Rapid Communications* 31.1 (2010), pp. 10–36.

[14] C. Keplinger, J.-Y. Sun, C. C. Foo, P. Rothemund, G. M. Whitesides, and Z. Suo. “Stretchable, transparent, ionic conductors”. In: *Science* 341.6149 (2013), pp. 984–987.

[15] S. Rosset, M. Niklaus, P. Dubois, and H. R. Shea. “Large-Stroke Dielectric Elastomer Actuators With Ion-Implanted Electrodes”. In: *J. Microelectromechanical Systems* 18.6 (2009), pp. 1300–1308.

[16] J. M. Gere and S. P. Timoshenko. *Mechanics of materials PWS*. KENT Publishing Company, Elsevier Science BV, Amsterdam, 1990.

[17] S. P. Timoshenko and J. M. Gere. *Theory of elastic stability*. McGraw-Hill Book Company Inc., New York, 1961.

[18] P. S. Bulson. *The stability of flat plates*. Elsevier Publishing Company, 1969.

[19] L. Landau and E. Lifshitz. *Fluid Mechanics*. 2nd. Vol. 6. Course of theoretical physics. 1987.

[20] F. Behroozi. “Fluid viscosity and the attenuation of surface waves: a derivation based on conservation of energy”. In: *European Journal of Physics* 25 (2004), p. 115.

[21] J. B. Grotberg and O. E. Jensen. “Biofluid mechanics in flexible tubes”. In: *Annual Review of Fluid Mechanics* 36 (2004), pp. 121–147.

[22] A. H. Shapiro. “Steady Flow in Collapsible Tubes”. In: *Journal of Biomechanical Engineering* 99.3 (1977). 10.1115/1.3426281, pp. 126–147.

Future Work

- *Extension of lubrication theory to axisymmetric or 3D geometries:*

  We used two-dimensional analysis of perturbation expansion in Chapter 3 to describe the flow in a two-dimensional channel. The same approach can be used to derive three-dimensional analytical solutions, which might more accurately describe flow within three-dimensional geometries. In addition, an axisymmetric solution can be developed to describe the flow in circular tubes with large constrictions.

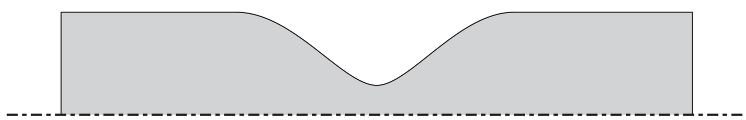

- *Coupling between the deformation of a flexible channel and its internal flow.* This can be another extension to lubrication theory by considering a shape function that changes as of a function of the internal flow, providing an analytical tool to describe the flow in flexible channels.

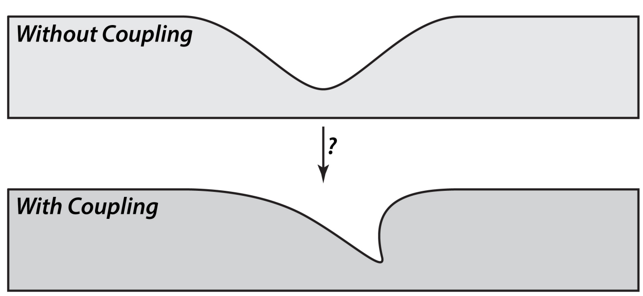

- *Use of electrical stimulus to cause snapping of thin plates for advanced functionality.* We presented a method in Chapters 4 and 5 to use electrical stimulus to make a dielectric film undergo bifurcation buckling. By modifying the geometry or material, *e.g.* making a film with a non-uniform thickness pattern or non-uniform material properties across its thickness, the film may undergo snap-through buckling. This might be beneficial when an accurate and fast response of the film is required for a specific functionality.

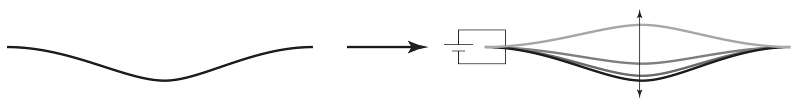

- *Soft-hard transition via non-Newtonian fluids within a channel with flexible arches.* The Newtonian fluid used in the first study can be replaced with a non-Newtonian fluid, e.g. a cornstarch suspension. By applying a mechanical strain, *e.g.* bending, stretching, pressing, or twisting, at a low rate, the device deforms similar to the previous cases. However, if the strain is applied at higher rates, the shear-thickening cornstarch suspension becomes stiff and reduces the device flexibility. This mechanism can be used for example in a knee brace to damp sudden falls or impacts beyond a critical threshold while the brace is flexible during walking and other normal activities.

- *Buckling deformation of thin cylindrical tubes via mechanical and electrical stimuli.* This study can be extended to the buckling deformation of thin, flexible tubes, and the interaction of the buckled tubes with their internal or external fluids. The tube can undergo buckling mechanically, *e.g.* by reducing the inside pressure, or electrically, *e.g.* by applying an electric potential between inner and outer conductive fluids.

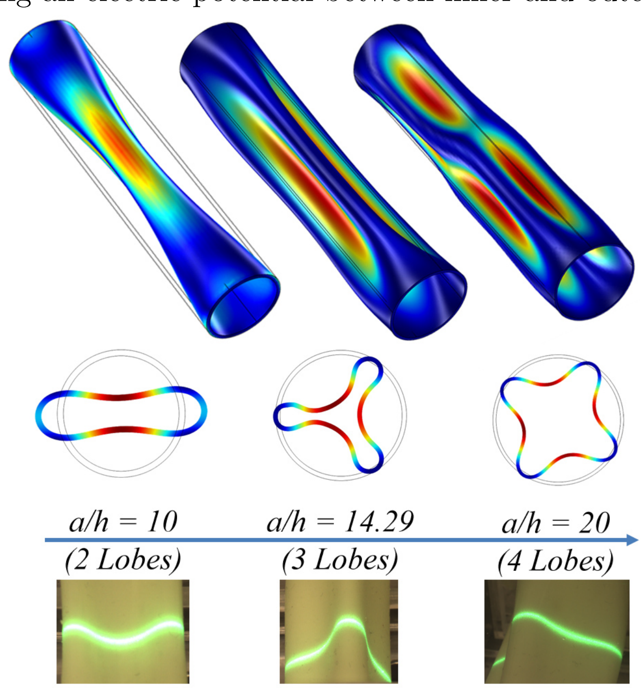

References

M. Abdelgawad and A. R. Wheeler. “The digital revolution: a new paradigm for microfluidics”. In: *Advanced Materials* 21.8 (2009), pp. 920–925.

Y. Aboelkassem and A. E. Staples. “A Bioinspired Pumping Model for Flow in a Microtube with Rhythmic Wall Contractions”. In: *Journal of Fluids and Structures* 42 (2013), pp. 187–204.

Y. Aboelkassem and A. E. Staples. “A Three-Dimensional Model for Flow Pumping in a Microchannel Inspired by Insect Respiration”. In: *Acta Mechanica* (2013), pp. 1–15.

Y. Aboelkassem and A. E. Staples. “Flow Transport in a Microchannel Induced by Moving Wall Contractions: a Novel Micropumping Mechanism”. In: *Acta Mechanica* 223.3 (2012), pp. 463–480.

N. Akkas. “Bifurcation and snap-through phenomena in asymmetric dynamic analysis of shallow spherical shells”. In: *Computers & Structures* 6.3 (1976), pp. 241–251.

R. F. Almgren. “An isotropic three-dimensional structure with Poisson’s ratio–1”. In: *Journal of Elasticity* 15 (1985), pp. 427–430.

O. Amyot and F. Plouraboue. “Capillary Pinching in a Pinched Microchannel”. In: *Physics of Fluids* 19.3 (2007).

H. Andersson and A. Van den Berg. “Microfluidic devices for cellomics: a review”. In: *Sensors and Actuators B: Chemical* 92.3 (2003), pp. 315–325.

S. S. Antman. *Nonlinear problems of elasticity, volume 107 of Applied Mathematical Sciences*. Springer, New York, 2005.

B. Audoly and Y. Pomeau. *Elasticity and geometry: from hair curls to the non-linear response of shells*. Oxford University Press, 2010.

F. Behroozi. "Fluid viscosity and the attenuation of surface waves: a derivation based on conservation of energy". In: *European Journal of Physics* 25 (2004), p. 115.

C. M. Bender and S. A. Orszag. *Advanced Mathematical Methods for Scientists and Engineers I*. Springer Science & Business Media, 1999.

E. Berthier and D. J. Beebe. "Flow rate analysis of a surface tension driven passive micropump". In: *Lab on a Chip* 7.11 (2007), pp. 1475–1478.

K. Bertoldi, P. M. Reis, S. Willshaw, and T. Mullin. "Negative Poisson's Ratio Behavior Induced by an Elastic Instability". In: *Advanced Materials* 22.3 (2010), pp. 361–366.

M. A. Biot. "General Theory of Three Dimensional Consolidation". In: *Journal of Applied Physics* 12.2 (1941), pp. 155–164.

D. Bonn, J. Eggers, J. Indekeu, J. Meunier, and E. Rolley. "Wetting and Spreading". In: *Reviews of Modern Physics* 81.2 (2009), pp. 739–805.

J. P. Boyd. "The devil's invention: asymptotic, superasymptotic and hyperasymptotic series". In: *Acta Applicandae Mathematica* 56.1 (1999), pp. 1–98.

M. Bozlar, C. Punckt, S. Korkut, J. Zhu, C. C. Foo, Z. Suo, and I. A. Aksay. "Dielectric elastomer actuators with elastomeric electrodes". In: *Applied Physics Letters* 101.9 (2012), pp. 091907–5.

P. Brochu and Q. Pei. "Advances in Dielectric Elastomers for Actuators and Artificial Muscles". In: *Macromolecular Rapid Communications* 31.1 (2010), pp. 10–36.

P. Bulson. *The Stability of Flat Plates*. Chatto and Windus, 1970.

P. S. Bulson. *The stability of flat plates*. Elsevier Publishing Company, 1969.

M. A. Burns et al. "An Integrated Nanoliter DNA Analysis Device". In: *Science* 282.5388 (1998), pp. 484–487.

F. Carpi, S. Bauer, and D. De Rossi. "Stretching Dielectric Elastomer Performance". In: *Science* 330.6012 (2010), pp. 1759–1761.

Z. Drmac, V. Hari, L. Sopta, Z. Tutek, and K. Veselic. *Applied Mathematics and Scientific Computing*. Springer, 2003.

J. C. Eijkel and A. Van Den Berg. "Nanofluidics: what is it and what can we expect from it?" In: *Microfluidics and Nanofluidics* 1.3 (2005), pp. 249–267.

R. Fair. “Digital microfluidics: is a true lab-on-a-chip possible?” In: *Microfluidics and Nanofluidics* 3.3 (2007), pp. 245–281.

M. Frasca. “Duality in perturbation theory and the quantum adiabatic approximation”. In: *Physical Review A* 58.5 (1998), p. 3439.

S. P. Fritton and S. Weinbaum. “Fluid and Solute Transport in Bone: Flow-Induced Mechanotransduction”. In: *Annual review of fluid mechanics* 41 (2009), pp. 347–374.

T. Fujii. “PDMS-based microfluidic devices for biomedical applications”. In: *Microelectronic Engineering* 61 (2002), pp. 907–914.

P. Garstecki, M. J. Fuerstman, H. A. Stone, and G. M. Whitesides. “Formation of Droplets and Bubbles in a Microfluidic T-Junction-Scaling and Mechanism of Break-up”. In: *Lab on a Chip* 6.3 (2006), pp. 437–446.

J. M. Gere and S. P. Timoshenko. *Mechanics of materials PWS*. KENT Publishing Company, Elsevier Science BV, Amsterdam, 1990.

L. J. Gibson and M. F. Ashby. “The Mechanics of Three-Dimensional Cellular Materials”. In: *Proceedings of the Royal Society of London A: Mathematical, Physical and Engineering Sciences* 382.1782 (1982), pp. 43–59.

L. J. Gibson, M. F. Ashby, G. S. Schajer, and C. I. Robertson. “The Mechanics of Two-Dimensional Cellular Materials”. In: *Proceedings of the Royal Society of London A: Mathematical, Physical and Engineering Sciences* 382.1782 (1982), pp. 25–42.

T. S. Gross, J. L. Edwards, K. J. McLeod, and C. T. Rubin. “Strain Gradients Correlate with Sites of Periosteal Bone Formation”. In: *Journal of Bone and Mineral Research* 12.6 (1997), pp. 982–988.

J. B. Grotberg and O. E. Jensen. “Biofluid mechanics in flexible tubes”. In: *Annual Review of Fluid Mechanics* 36 (2004), pp. 121–147.

E. J. Hinch. *Perturbation methods*. Cambridge university press, 1991.

D. P. Holmes, B. Tavakol, G. Froehlicher, and H. A. Stone. “Control and manipulation of microfluidic flow via elastic deformations”. In: *Soft Matter* 9.29 (2013), pp. 7049–7053.

B. D. Iverson and S. V. Garimella. “Recent advances in microscale pumping technologies: a review and evaluation”. In: *Microfluidics and Nanofluidics* 5.2 (2008), pp. 145–174.

A. T. John. “Hydrodynamic Lubrication”. In: *Handbook of Lubrication and Tribology, Volume II*. doi:10.1201/b12265-18. CRC Press, 2012, pp. 1–14.

S. Judex, T. S. Gross, and R. F. Zernicke. “Strain Gradients Correlate with Sites of Exercise-Induced Bone-Forming Surfaces in the Adult Skeleton”. In: *Journal of Bone and Mineral Research* 12.10 (1997), pp. 1737–1745.

C. Keplinger, J.-Y. Sun, C. C. Foo, P. Rothemund, G. M. Whitesides, and Z. Suo. “Stretchable, transparent, ionic conductors”. In: *Science* 341.6149 (2013), pp. 984–987.

J. Kevorkian and J. D. Cole. *Perturbation methods in applied mathematics*. Vol. 34. Springer Science & Business Media, 2013.

D.-Y. Khang, H. Jiang, Y. Huang, and J. A. Rogers. “A Stretchable Form of Single-Crystal Silicon for High-Performance Electronics on Rubber Substrates”. In: *Science* 311.5758 (2006), pp. 208–212.

H. S. Kim and A. J. Crosby. “Solvent-Responsive Surface via Wrinkling Instability”. In: *Advanced Materials* 23.36 (2011), pp. 4188–4192.

P. Kundu and I. Cohen. *Fluid Mechanics, 4th Edition*. Elsevier Academic Press, 2008.

R. Lakes. “Foam Structures with a Negative Poisson’s Ratio”. In: *Science* 235.4792 (1987), pp. 1038–1040.

L. Landau and E. Lifshitz. *Fluid Mechanics*. 2nd. Vol. 6. Course of theoretical physics. 1987.

W. E. Langlois. *Slow Viscous Flow*. New York: Macmillan, 1964.

D. Laser and J. Santiago. “A review of micropumps”. In: *Journal of micromechanics and microengineering* 14.6 (2004), R35.

L. G. Leal. *Advanced Transport Phenomena: Fluid Mechanics and Convective Transport Processes*. Cambridge: Cambridge University Press, 2007.

D. C. Leslie, C. J. Easley, E. Seker, J. M. Karlinsey, M. Utz, M. R. Begley, and J. P. Landers. “Frequency-specific flow control in microfluidic circuits with passive elastomeric features”. In: *Nature Physics* 5.3 (2009), pp. 231–235.

B. Li, H. Chen, J. Qiang, S. Hu, Z. Zhu, and Y. Wang. “Effect of mechanical pre-stretch on the stabilization of dielectric elastomer actuation”. In: *J. Physics D: Applied Physics* 44.15 (2011), p. 155301.

L. Limat and H. A. Stone. “Three-Dimensional Lubrication Model of a Contact Line Corner Singularity”. In: *EPL (Europhysics Letters)* 65.3 (2004), p. 365.

T. Lu, J. Huang, C. Jordi, G. Kovacs, R. Huang, D. R. Clarke, and Z. Suo. “Dielectric elastomer actuators under equal-biaxial forces, uniaxial forces, and uniaxial constraint of stiff fibers”. In: *Soft Matter* 8.22 (2012), pp. 6167–6173.

M. C. Marchetti, J. F. Joanny, S. Ramaswamy, T. B. Liverpool, J. Prost, M. Rao, and R. A. Simha. “Hydrodynamics of Soft Active Matter”. In: *Reviews of Modern Physics* 85.3 (2013), pp. 1143–1189.

D. Mark, S. Haeberle, G. Roth, F. von Stetten, and R. Zengerle. “Microfluidic lab-on-a-chip platforms: requirements, characteristics and applications”. In: *Chemical Society Reviews* 39.3 (2010), pp. 1153–1182.

J. Melin and S. R. Quake. “Microfluidic large-scale integration: the evolution of design rules for biological automation”. In: *Annu. Rev. Biophys. Biomol. Struct.* 36 (2007), pp. 213–231.

S. Michelin, T. D. Montenegro-Johnson, G. De Canio, N. Lobato-Dauzier, and E. Lauga. “Geometric pumping in autophoretic channels”. In: *Soft Matter* (2015).

A. H. Nayfeh. *Perturbation methods*. John Wiley & Sons, 2008.

N.-T. Nguyen and Z. Wu. “Micromixers–a review”. In: *Journal of Micromechanics and Microengineering* 15.2 (2005), R1.

Z. G. Nicolaou and A. E. Motter. “Mechanical metamaterials with negative compressibility transitions”. In: *Nat Mater* 11.7 (2012), pp. 608–613.

H. Ockendon and J. R. Ockendon. *Viscous Flow*. Cambridge: Cambridge University Press, 1995.

K. W. Oh and C. H. Ahn. “A review of microvalves”. In: *Journal of Micromechanics and Microengineering* 16.5 (2006), R13.

T. J. Pedley, B. S. Brook, and R. S. Seymour. “Blood Pressure and Flow Rate in the Giraffe Jugular Vein”. In: *Philosophical Transactions of the Royal Society of London. Series B: Biological Sciences* 351.1342 (1996), pp. 855–866.

T. J. Pedley and X. Y. Luo. “Modelling Flow and Oscillations in Collapsible Tubes”. In: *Theoretical and Computational Fluid Dynamics* 10.1-4 (1998), pp. 277–294.

R. Pelrine, R. Kornbluh, Q. Pei, and J. Joseph. “High-Speed Electrically Actuated Elastomers with Strain Greater Than 100%”. In: *Science* 287.5454 (2000), pp. 836–839.

R. E. Pelrine, R. D. Kornbluh, and J. P. Joseph. “Electrostriction of polymer dielectrics with compliant electrodes as a means of actuation”. In: *Sensors and Actuators A: Physical* 64.1 (1998), pp. 77–85.

J.-S. Plante and S. Dubowsky. “Large-scale failure modes of dielectric elastomer actuators”. In: *International Journal of Solids and Structures* 43 (2006), pp. 7727–7751.

F. Plouraboue, S. Geoffroy, and M. Prat. “Conductances between Confined Rough Walls”. In: *Physics of Fluids* 16.3 (2004), pp. 615–624.

C. Pozrikidis. *Introduction to theoretical and computational fluid dynamics, 2nd Edition*. Oxford University Press, 2011.

J. Prakash and P. Sinha. “Lubrication Theory for Micropolar Fluids and its Application to a Journal Bearing”. In: *International Journal of Engineering Science* 13.3 (1975), pp. 217–232.

C. E. Riley. “Elastic buckling loads of slender columns with variable cross section by the newmark method”. MA thesis. Colorado State University, 2003.

R. M. Rivello. *Theory and analysis of flight structures*. McGraw-Hill College, 1969.

L. J. Robert. “Lubrication”. In: *Handbook of Lubrication and Tribology, Volume II*. doi:10.1201/b12265-16. CRC Press, 2012, pp. 1–14.

V. Rocco, F. Antonio, B. Massimo, C. Federico, F. Gabriele, and R. Danilo De. “Modeling and experimental validation of buckling dielectric elastomer actuators”. In: *Smart Materials and Structures* 21.9 (2012), p. 094005.

S. Rosset, M. Niklaus, P. Dubois, and H. R. Shea. "Large-Stroke Dielectric Elastomer Actuators With Ion-Implanted Electrodes". In: *J. Microelectromechanical Systems* 18.6 (2009), pp. 1300–1308.

S. Rosset, M. Niklaus, P. Dubois, and H. R. Shea. "Mechanical characterization of a dielectric elastomer microactuator with ion-implanted electrodes". In: *Sensors and Actuators A: Physical* 144.1 (2008), pp. 185–193.

G. W. Scherer, J. H. Prevost, and Z.-H. Wang. "Bending of a poroelastic beam with lateral diffusion". In: *International Journal of Solids and Structures* 46 (2009), pp. 3451–3462.

R. B. Schoch, J. Han, and P. Renaud. "Transport phenomena in nanofluidics". In: *Reviews of Modern Physics* 80.3 (2008), p. 839.

R. Shankar, T. K. Ghosh, and R. J. Spontak. "Dielectric elastomers as next-generation polymeric actuators". In: *Soft Matter* 3.9 (2007), pp. 1116–1129.

A. H. Shapiro. "Steady Flow in Collapsible Tubes". In: *Journal of Biomechanical Engineering* 99.3 (1977). 10.1115/1.3426281, pp. 126–147.

J. H. Snoeijer. "Free-Surface Flows with Large Slopes: Beyond Lubrication Theory". In: *Physics of Fluids* 18.2 (2006).

H. A. Stone. "On Lubrication Flows in Geometries with Zero Local Curvature". In: *Chemical Engineering Science* 60.17 (2005), pp. 4838–4845.

H. A. Stone, A. D. Stroock, and A. Ajdari. "Engineering flows in small devices: Microfluidics toward a lab-on-a-chip". In: *Annual Review of Fluid Mechanics* 36 (2004), pp. 381–411.

Y. Sun, W. M. Choi, H. Jiang, Y. Y. Huang, and J. A. Rogers. "Controlled buckling of semiconductor nanoribbons for stretchable electronics". In: *Nat Nano* 1.3 (2006), pp. 201–207.

Z. Suo. "Mechanics of stretchable electronics and soft machines". In: *MRS Bulletin* 37.03 (2012), pp. 218–225.

Z. Suo. "Theory of dielectric elastomers". In: *Acta Mechanica Solida Sinica* 23.6 (2010), pp. 549–578.

A. Szeri. *Fluid Film Lubrication: Theory and Design*. Cambridge University Press, 2005.

P. Tabeling. *Introduction to microfluidics*. Oxford University Press, 2005. ISBN: 0198568649.

B. Tavakol, M. Bozlar, C. Punckt, G. Froehlicher, H. A. Stone, I. A. Aksay, and D. P. Holmes. “Buckling of dielectric elastomeric plates for soft, electrically active microfluidic pumps”. In: *Soft matter* 10.27 (2014), pp. 4789–4794.

J. O. Tegenfeldt, C. Prinz, H. Cao, R. L. Huang, R. H. Austin, S. Y. Chou, E. C. Cox, and J. C. Sturm. “Micro-and nanofluidics for DNA analysis”. In: *Analytical and Bioanalytical Chemistry* 378.7 (2004), pp. 1678–1692.

T. Thorsen, S. J. Maerkl, and S. R. Quake. “Microfluidic large-scale integration”. In: *Science* 298.5593 (2002), pp. 580–584.

J. N. Tilton and A. C. Payatakes. “Collocation solution of creeping newtonian flow through sinusoidal tubes: A correction”. In: *AIChE Journal* 30.6 (1984), pp. 1016–1021.

S. Timoshenko, S. Woinowsky-Krieger, and S. Woinowsky-Krieger. *Theory of plates and shells*. Vol. 2. McGraw-hill New York, 1959.

S. P. Timoshenko and J. M. Gere. *Theory of elastic stability*. McGraw-Hill Book Company Inc., New York, 1961.

M. A. Unger, H.-P. Chou, T. Thorsen, A. Scherer, and S. R. Quake. “Monolithic Microfabricated Valves and Pumps by Multilayer Soft Lithography”. In: *Science* 288.5463 (2000), pp. 113–116.

D. Vella, J. Bico, A. Boudaoud, B. Roman, and P. M. Reis. “The macroscopic delamination of thin films from elastic substrates”. In: *Proceedings of the National Academy of Sciences* 106.27 (2009), pp. 10901–10906.

M. W. Westneat, J. J. Socha, and W.-K. Lee. “Advances in biological structure, function, and physiology using synchrotron X-ray imaging”. In: *Annu. Rev. Physiol.* 70 (2008), pp. 119–142.

F. White. *Fluid mechanics*. McGraw-Hill Higher Education, 2015.

G. M. Whitesides. “What Comes Next?” In: *Lab on a Chip* 11.2 (2011), pp. 191–193.

G. M. Whitesides. “The origins and the future of microfluidics”. In: *Nature* 442.7101 (2006), pp. 368–373.

W. Wu, A. DeConinck, and J. A. Lewis. “Omnidirectional Printing of 3D Microvascular Networks”. In: *Advanced Materials* 23.24 (2011), H178–H183.

E. Yamaguchi and W. Chen. “Basic theory of plates and elastic stability”. In: *Structural Engineering Handbook, Boca Raton, CRC Press LLC* (1999).

X. Zhao and Z. Suo. “Theory of Dielectric Elastomers Capable of Giant Deformation of Actuation”. In: *Physical Review Letters* 104.17 (2010), p. 178302.

Appendix A. LabVIEW Codes

This LabVIEW code was developed initially to control several equipment, such as linear stages, cameras, and a high voltage amplifier, while simultaneously monitoring and recording several parameters, such as pressure from a pressure sensor, flow from a flowmeter, and voltage from a high voltage amplifier. We are currently working on an event-based version of this code with improved performance. The new code will be released after debugging process. Here is an earlier version that is debugged:

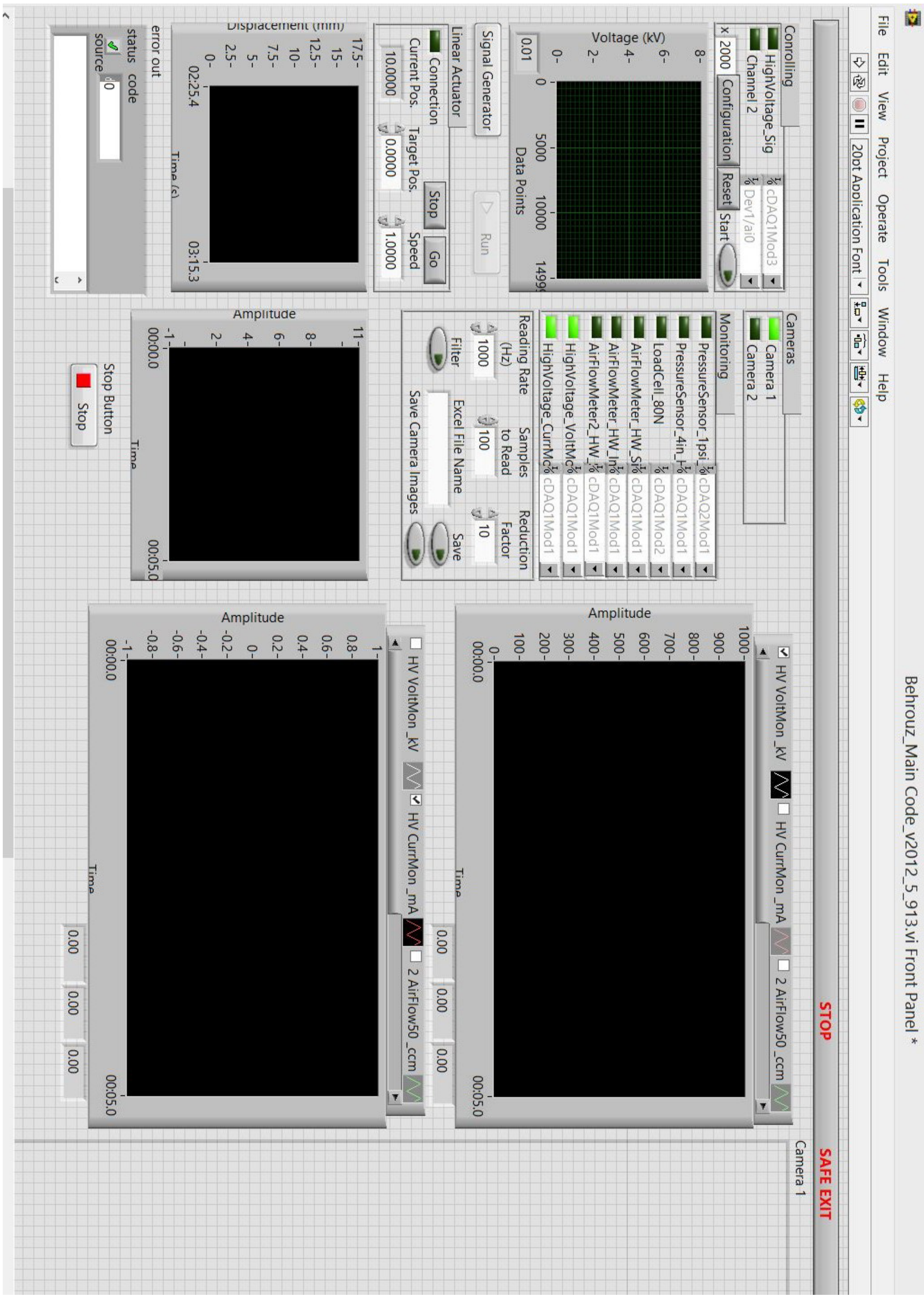
Behrouz_Main Code_v2012_5_913.vi Front Panel *
File Edit View Project Operate Tools Window Help
20pt Application Font
STOP
SAFE EXIT
Controlling
HighVoltage_Sig
Channel 2
cDAQ1Mod3
Dev1/ai0
Configuration
Reset
Start
Voltage (kV)
Data Points
Signal Generator
Run
Linear Actuator
Connection
Stop
Go
Current Pos.
Target Pos.
Speed
10.0000
0.0000
1.0000
Displacement (mm)
error out
status
code
source
Cameras
Camera 1
Camera 2
Monitoring
PressureSensor_1psi
PressureSensor_4in
LoadCell_80N
AirFlowMeter_HW_Si
AirFlowMeter_HW_In
AirFlowMeter2_HW
HighVoltage_VoltMo
HighVoltage_CurrMo
Reading Rate (Hz)
Samples to Read
Reduction Factor
1000
100
10
Filter
Excel File Name
Save
Save Camera Images
Amplitude
Stop Button
Stop
HV VoltMon _kV
HV CurrMon _mA
2 AirFlow50 _ccm
Camera 1

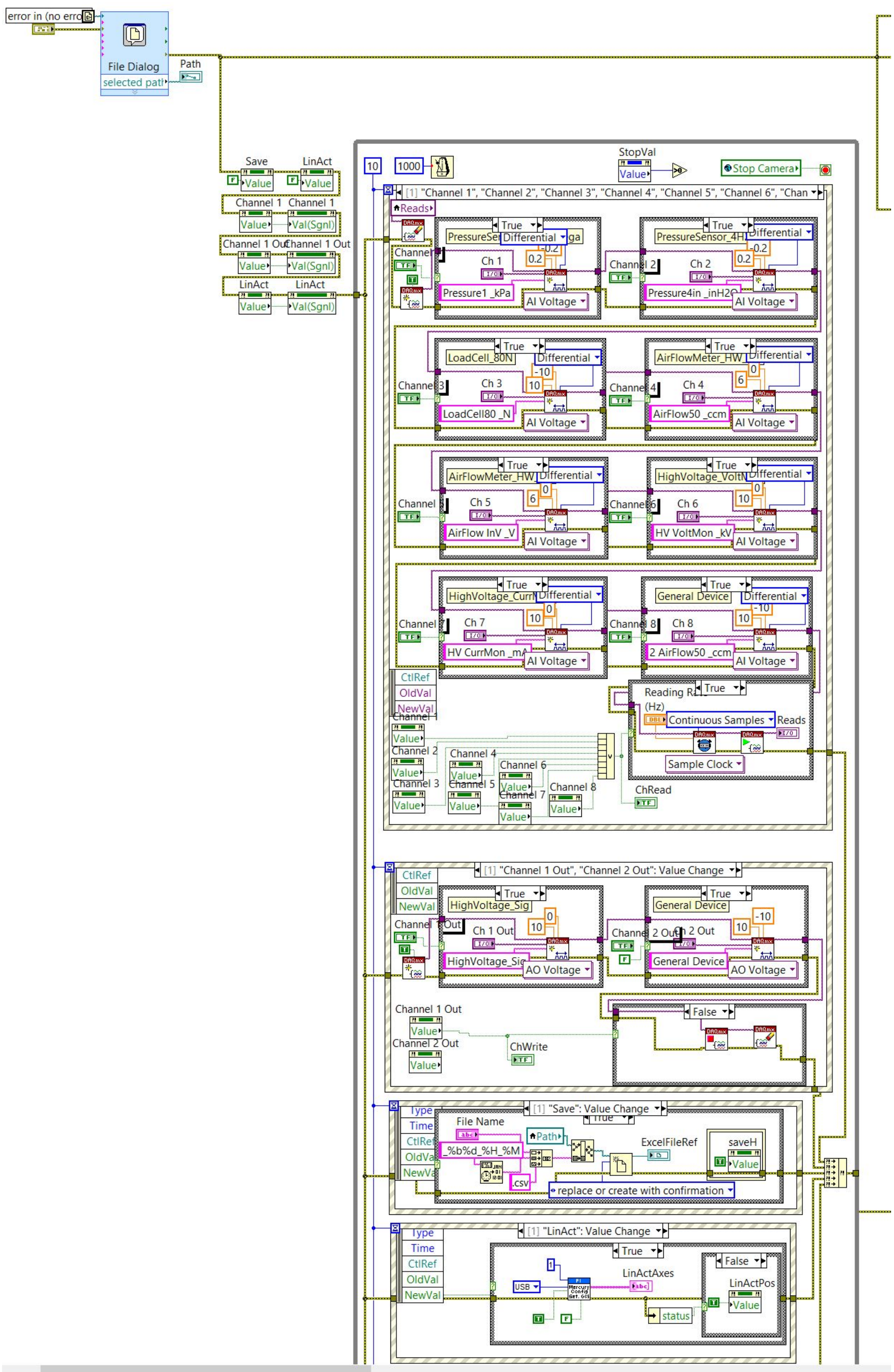

error in (no error)
File Dialog
selected path
Path
Save
LinAct
Channel 1
Channel 1 Out
StopVal
Stop Camera
[1] "Channel 1", "Channel 2", "Channel 3", "Channel 4", "Channel 5", "Channel 6", "Chan
Reads
PressureSensor_4H
Pressure1 _kPa
Pressure4in _inH2O
AI Voltage
Differential
LoadCell_80N
LoadCell80 _N
AirFlowMeter_HW
AirFlow50 _ccm
AirFlow InV _V
HighVoltage_Volt
HV VoltMon _kV
HighVoltage_Curr
HV CurrMon _mA
General Device
2 AirFlow50 _ccm
Continuous Samples
Sample Clock
ChRead
[1] "Channel 1 Out", "Channel 2 Out": Value Change
HighVoltage_Sig
AO Voltage
ChWrite
[1] "Save": Value Change
File Name
%b%d_%H_%M
csv
ExcelFileRef
saveH
replace or create with confirmation
[1] "LinAct": Value Change
LinActAxes
LinActPos
status

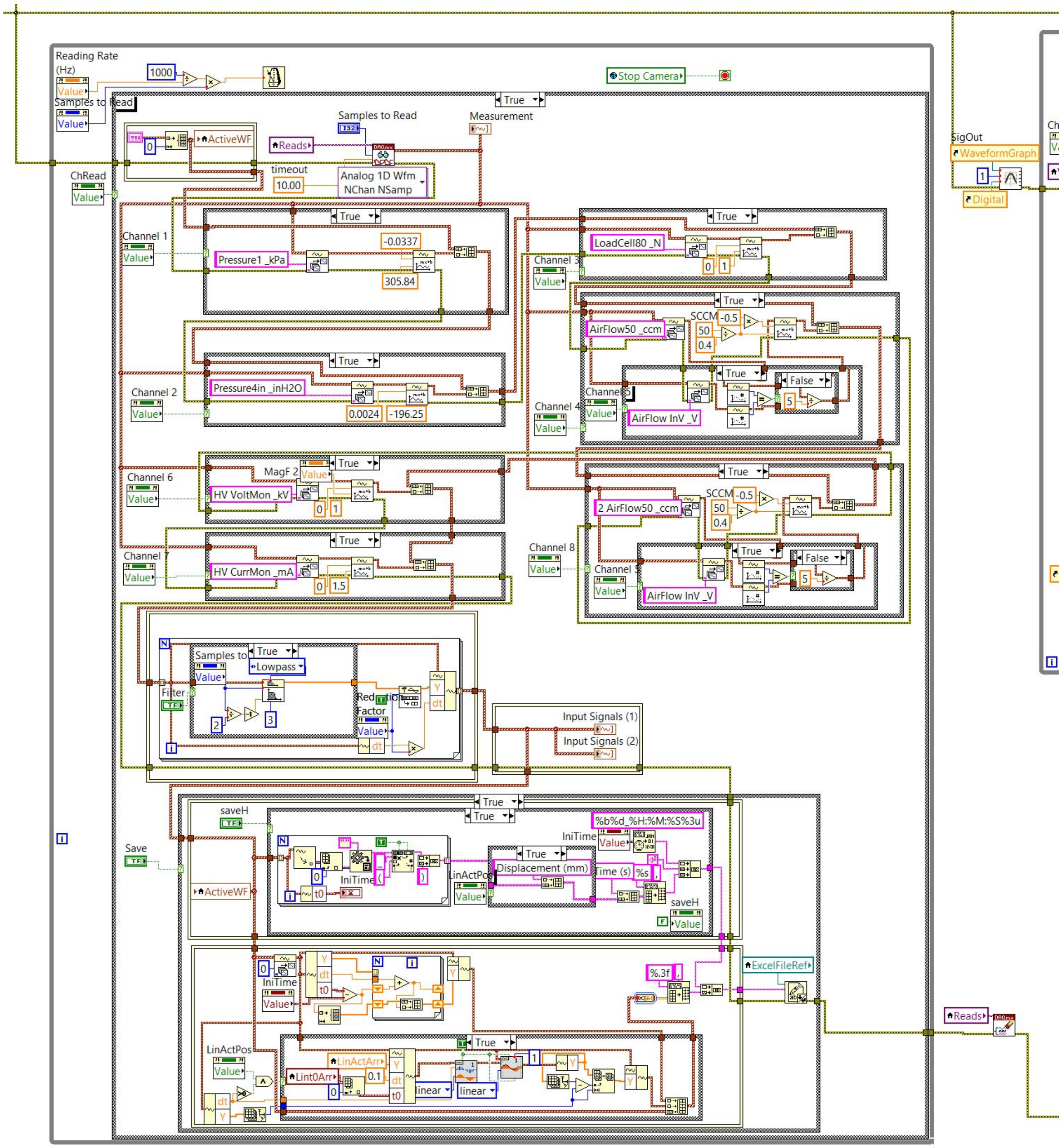

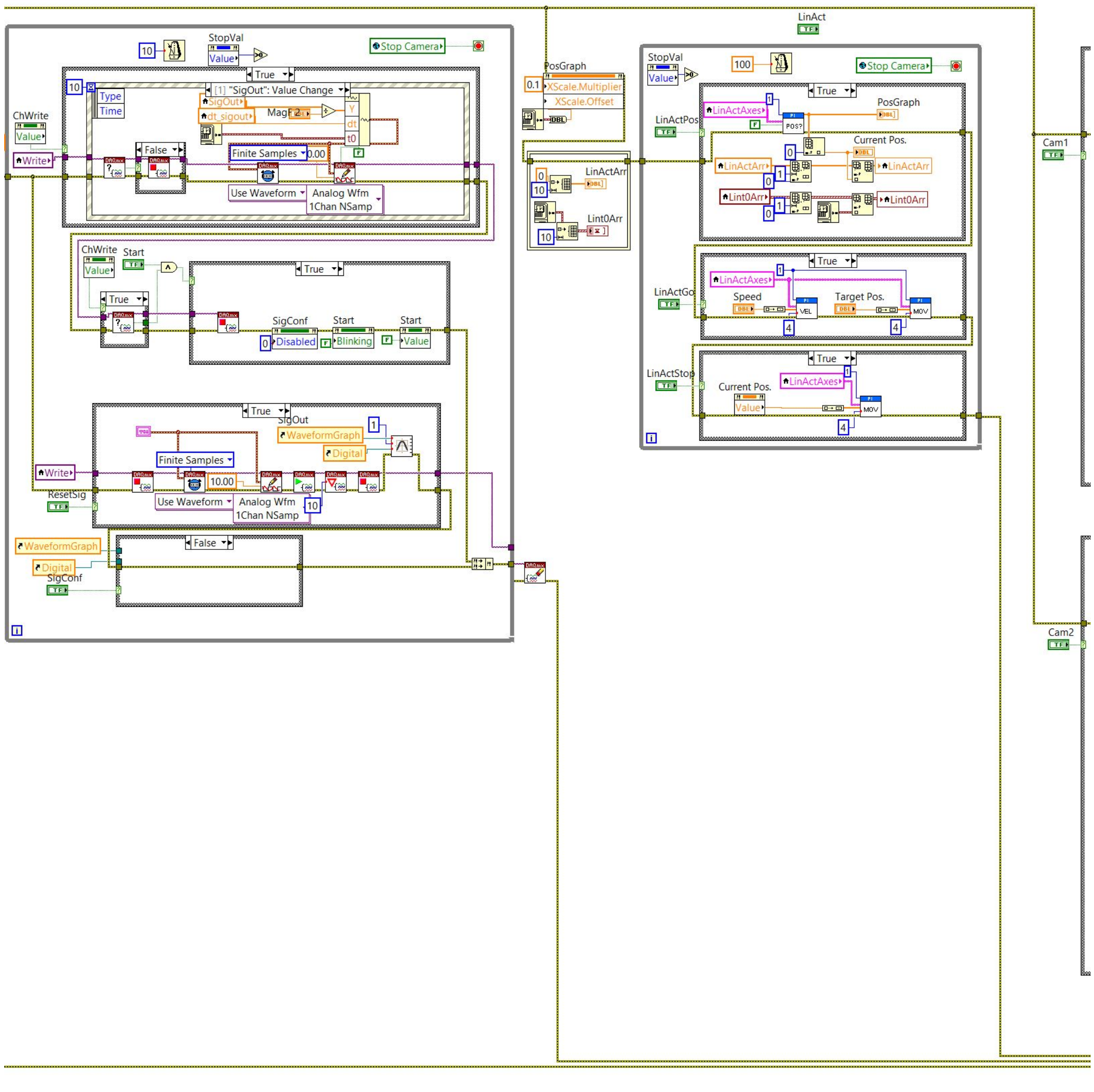
StopVal
Value
Stop Camera
"SigOut": Value Change
SigOut
dt_sigout
Mag
Finite Samples
Use Waveform
Analog Wfm 1Chan NSamp
ChWrite
Write
Start
SigConf
Disabled
Blinking
WaveformGraph
Digital
ResetSig
PosGraph
XScale.Multiplier
XScale.Offset
LinActArr
Lint0Arr
LinAct
LinActPos
LinActAxes
Current Pos.
LinActGo
Speed
Target Pos.
LinActStop
Cam1
Cam2

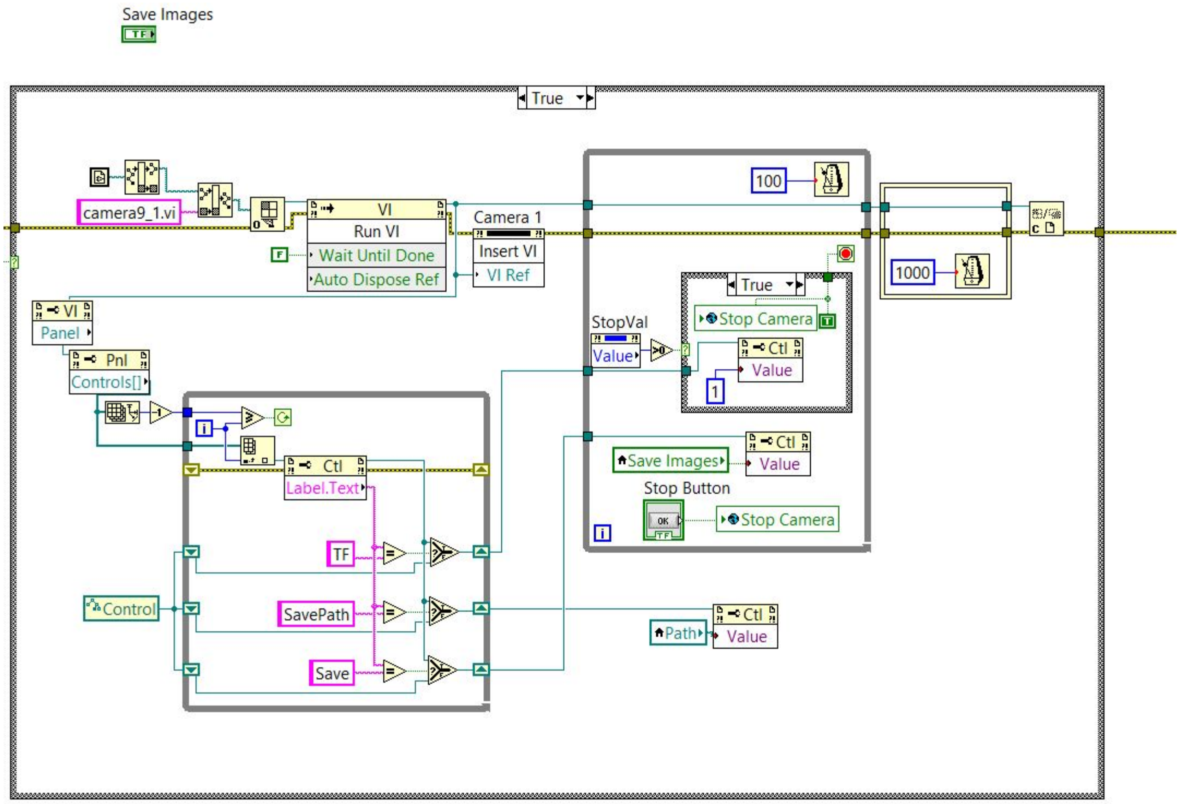
Save Images
True
camera9_1.vi
VI
Run VI
Wait Until Done
Auto Dispose Ref
Camera 1
Insert VI
VI Ref
100
1000
VI
Panel
Pnl
Controls[]
StopVal
Value
True
Stop Camera
Ctl
Value
1
Ctl
Label.Text
TF
SavePath
Save
Control
Save Images
Ctl
Value
Stop Button
Stop Camera
Path
Ctl
Value

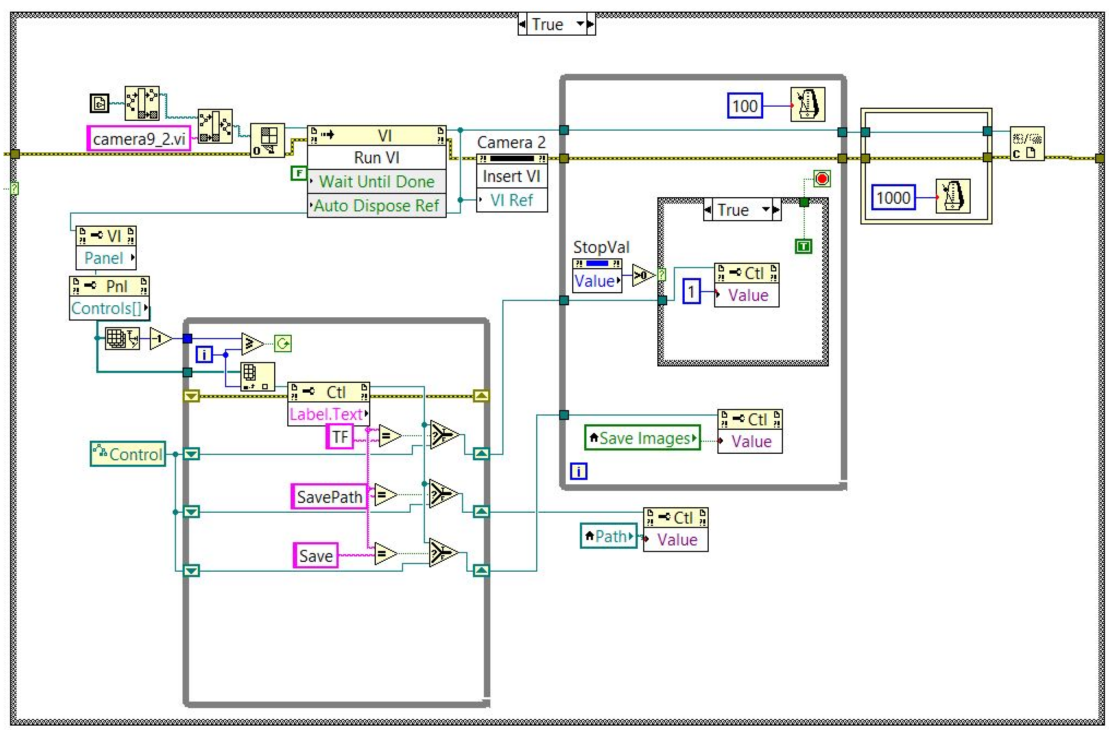
True
camera9_2.vi
VI
Run VI
Wait Until Done
Auto Dispose Ref
Camera 2
Insert VI
VI Ref
100
1000
VI
Panel
Pnl
Controls[]
StopVal
Value
True
1
Ctl
Value
Ctl
Label.Text
TF
SavePath
Save
Control
Save Images
Ctl
Value
Path
Ctl
Value

Appendix B. MATLAB Codes

B.1 Extracting curvature profiles from images

The following code extracts the curvature profiles of all the images within one folder and prepares the results for the next code to generate 3D surfaces:

```
% By Behrouz Tavakol -- Last Modified on 12/08/2012
% Gets the curvature for each slice.
% -----------------------

clear all; close all; clc

% ------- The desired folder for analysis ... ----------
seldir= uigetdir('',...
    'Please select your desired folder for image processing');
if seldir ==0
    seldir = '';
else
    seldir = [seldir,'\'];
end

% ------- z (stage movement relative to the center) ---------
```

```
% positive: further from the camera
% negative: closer to the camera

z_str= inputdlg({'z (mm):'},'Calibration...',1,{'0'});
z = str2double(z_str{1});

% ------- Reading data from Excel ... ----------
Excelfilename = dir([seldir,'*.csv']);


Excel_data = importdata([seldir,Excelfilename(end).name]);
ti_s = Excel_data.textdata{1,1};
for i=1:size(Excel_data.colheaders,2)
    if size(strfind(lower(Excel_data.colheaders{i}),'time'),2)>0
        Tex = Excel_data.data(:,i);
    elseif size(strfind(lower(Excel_data.colheaders{i}),'hv voltmon'),2)>0
        Vex = Excel_data.data(:,i);
    elseif size(strfind(lower(Excel_data.colheaders{i}),'hv currmon'),2)>0
        Aex = Excel_data.data(:,i);
    elseif size(strfind(lower(Excel_data.colheaders{i}),'pressure'),2)>0
        Pex = Excel_data.data(:,i);
    end
end

ti_s = ti_s(find(ti_s=='_')+1:end);
s1_ms = ti_s(end-2:end);
s1_s  = ti_s(end-5:end-4);
s1_m  = ti_s(end-8:end-7);
s1_h  = ti_s(end-11:end-10);

Ti = str2double(s1_ms)/1000+str2double(s1_s)+...
         str2double(s1_m)*60+str2double(s1_h)*3600
```

```
if isempty(Vex), break, end
if Tex(1)>1
    disp('** Data Correction was required since time did not start from 0')
    Ti = Ti + Tex(1)-Tex(2)+Tex(1);
    Tex(1:10) = Tex(1:10)-Tex(1)+Tex(2)-Tex(1);
    %break
end


filelist = dir([seldir,'*.TIFF']);
if size(filelist,1)==0, return, end

% ----------- simple Calibration ---------------
% dx & dy in (mm/px)
i = 0;
calib = false;
while i<size(filelist,1) && not(calib)
   i = i+1;
   if size(strfind(lower(filelist (i).name),'calib'),2)>0
       calib = true;
   end
end
if calib
    [dx, dy] = Simple_Calib_Using_2Lines([seldir,filelist(i).name]);
    filelist(i)=[];
else
    [dx, dy] = Simple_Calib_Using_2Lines([seldir,filelist(1).name]);
end

% --------------- Cropping ... -----------------
I1 = imread([seldir,filelist(end).name]);
```

```
I1 = I1/2 + imread([seldir,filelist(round(end/2)).name]);
I1 = I1 + imread([seldir,filelist(1).name])/2;
[I2,rect]=imcrop(I1);close
rect = round(rect)   % [x y width height]

% --------------- Masking ... -----------------

I2 = imcrop(I1,rect);
I2 = rgb2gray(I2);
I2 = imadjust(I2);
masks = ones(size(I2));
mn = 0;

% clear masks
mask_b = true;
while mask_b
    for i=1:size(masks,1)
        for j=1:size(masks,2)
            I2(i,j) = I2(i,j).*masks(i,j);
        end
    end

    I2 = imadjust(I2);
    imshow(im2bw(I2,graythresh(I2)));
    anw = questdlg('Would you like to mask any region?', ...
                   ['Masking #',num2str(mn+1)], 'Yes','No','Reset','No');
    switch anw
        case 'Yes'
            mn = mn+1;
            imshow(I2);

            [J,BW] = roifill;
```

```
            for i=1:size(masks,1)
                for j=1:size(masks,2)
                    masks(i,j) = masks(i,j).*(1-BW(i,j));
                end
            end
            for i=1:size(masks,1)
                for j=1:size(masks,2)
                    I2(i,j) = I2(i,j).*masks(i,j);
                end
            end
            imshow(I2);

        case 'No'
            mask_b = false;
            break

        case 'Reset'
            I2 = imcrop(I1,rect);
            I2 = rgb2gray(I2);
            I2 = imadjust(I2);
            masks = ones(size(I2));
            mask_b = true;
            mn = 0;

            imshow(im2bw(I2,graythresh(I2)));
    end
end

% Static or Dynamic Masking

anw = questdlg('Which masking technique would you like to apply?', ...
                   'Static or Dynamic Masking', ...
```

```
                   'Static','Dynamic','Static');
switch anw
    case 'Static'
        StatMask = true;
    case 'Dynamic'
        StatMask = false;
        dmasks = ones(size(I2));
end

%---------------------------------------------
% ------------ Reading Images ... -----------


AnlTime = 0;
tic;
for nn = 1:size(filelist,1)

    s = filelist(nn).name;

% ---------- Reading Time ----------------
    s1 = s(1:find(s=='.')-1);
    s1_ms = s1(end-2:end);
    s1_s  = s1(end-4:end-3);
    s1_m  = s1(end-6:end-5);
    s1_h  = s1(end-8:end-7);
    ti = str2double(s1_ms)/1000+str2double(s1_s)+...
         str2double(s1_m)*60+str2double(s1_h)*3600;

    T(nn) = ti-Ti;

% ---------- Reading and Analyzing the Image -----------
    I1 = imread([seldir,s]);
```

```
if StatMask
% --- Static Masking ...
    I2 = imcrop(I1,rect);

    I2 = rgb2gray(I2);

    for i=1:size(masks,1)
        for j=1:size(masks,2)
            I2(i,j) = I2(i,j).*masks(i,j);
        end
    end
    I2 = imadjust(I2);

else
% --- Dynamic Masking ....
    if mod(nn-1,10)==0
        I2 = imcrop(I1,rect);
        if nn+9 <= size(filelist,1)
           I2=(I2+imcrop(imread([seldir,filelist(nn+9).name]),rect));
        end

        I2 = rgb2gray(I2);

        for i=1:size(masks,1)
            for j=1:size(masks,2)
                I2(i,j) = I2(i,j).*masks(i,j).*dmasks(i,j);
            end
        end
        I2 = imadjust(I2);
        mask_b = true;
        dmn = 0;
```

```
fm = figure; imshow(im2bw(I2,graythresh(I2)));
while mask_b
    anw = questdlg('Would you like to modify the dynamic mask?', ...
       ['Masking #',num2str(dmn+1)], 'Yes','No','Reset','No');
    switch anw
        case 'Yes'
            dmn = dmn+1;
            imshow(I2);
            [J,BW] = roifill;
            for i=1:size(dmasks,1)
                for j=1:size(dmasks,2)
                    dmasks(i,j) = dmasks(i,j).*(1-BW(i,j));
                end
            end
            for i=1:size(dmasks,1)
                for j=1:size(dmasks,2)
                    I2(i,j) = I2(i,j).*dmasks(i,j);
                end
            end
            imshow(im2bw(I2,graythresh(I2)));

        case 'No'
            mask_b = false;
            break

        case 'Reset'
            dmasks = ones(size(I2));
            mask_b = true;
            dmn = 0;
            I2 = imcrop(I1,rect);
            if nn+9 <= size(filelist,1)
                I2=(I2+imcrop(imread(...
```

```
                        [seldir,filelist(nn+9).name]),rect));
                end
                I2 = rgb2gray(I2);

                for i=1:size(masks,1)
                    for j=1:size(masks,2)
                        I2(i,j) = I2(i,j).*masks(i,j);
                    end
                end
                I2 = imadjust(I2);
                imshow(im2bw(I2,graythresh(I2)));
            end
        end
        close(fm);
        refresh
        uiwait(gcf,1)
    end

    I2 = imcrop(I1,rect);
    I2 = rgb2gray(I2);

    for i=1:size(masks,1)
        for j=1:size(masks,2)
            I2(i,j) = I2(i,j).*masks(i,j).*dmasks(i,j);
        end
    end
    I2 = imadjust(I2);

end
% ----

level = graythresh(I2);
```

```
    F = 1.0; % Modify this to find a good threshold
    I3 = im2bw(I2,level*F);

% ---------- Obtaining the curvature -----------
    i = 1;
    np = 0;
    xc = []; bc = []; tc = [];

    while i<=size(I3,2)
        rem = find(I3(:,i)==1);
        if size(rem,1)>0
            np = np+1;
            xc(np)=i;
            bc(np)=rem(end);
            tc(np)=rem(1);
            if np>1
             if  abs(bc(np)-tc(np)) > 20
                 disp(['Modifying the path (unusual path!) @',num2str(i)])
            end
            end

        end
        i = i+1;
    end

    c_x = xc;
    c_y = (tc+bc)./2;

    if nn==1
        mean_width = mean(abs(tc-bc));
    end
```

```
%  ---------- Filtering & Smoothing -----------

    f = 2;                    % Hz (sampling frequency)
    f_cutoff = 0.04;           % Hz (cutoff frequency)

    fnorm = f_cutoff/(f/2);   % normalized cut off freq

    [b1,a1] = butter(10,fnorm,'low'); % Low pass Butterworth filter of order 10
    c_y_sm = filtfilt(b1,a1,c_y); % filtering



%  ---------- Finding the corresponding voltage and saving -----------

[t_err t_abs_ind] = min(abs(T(nn)-Tex));
tr(nn).ind = t_abs_ind;
tr(nn).t   = T(nn);
tr(nn).v   = Vex(t_abs_ind);
tr(nn).z   = z;
tr(nn).X   = c_x+rect(1);
tr(nn).Y   = c_y_sm+rect(2);
tr(nn).p   = Pex(t_abs_ind);



% % -- Plotting every 10 results
    if mod(nn,10)==0
        imshow(I1); hold on
        plot(c_x+rect(1),c_y_sm+rect(2),'r')
        title(['Frame# ',num2str(nn),',  V = ',...
```

```
                num2str(Vex(t_abs_ind)/1000,'% 6.3f'),' kV'])
        refresh
        uiwait(gcf,1)
    end

end

AnlTime = AnlTime+toc;
disp(['Elapsed Time = ',num2str(AnlTime)]);

%*******************************************

% % Plot desired data set:
% nn = 151;
% s = filelist(nn).name;
% I1 = imread([seldir,s]);
% imshow(I1); hold on
% plot(tr(nn).X,tr(nn).Y,'r')
% title(['Frame# ',num2str(nn),',  V = ',...
%        num2str(tr(nn).v/1000,'% 6.3f'),' kV'])

% ------------------------
% % Plot all curves
% for nn = 1:10:size(tr,2)
%     figure, hold on;
%     title(['Frames# ',num2str(nn),'-', num2str(nn+9)])
%     xlim([0 size(I1,2)])
%     ylim([-size(I1,1) 0])
%     for i=nn:nn+9
%         plot(tr(i).X,-tr(i).Y,'r')
%     end
%     uiwait(gcf,3)
```

```
%     close
% end

% ------------------------
% % Plot maximum height vs. pressure
    clear Xt Zt
    Xt = tr(nn).X;
    Zt = tr(nn).Y./cos(pi/6);
    theta = atan((mean(Zt(end-4:end))-mean(Zt(1:5)))/...
                  (mean(Xt(end-4:end))-mean(Xt(1:5))));
    Xarr = Xt.*cos(-theta) + Zt.*-sin(-theta);
    Zarr = Xt.*sin(-theta) + Zt.*cos(-theta);

    x0 = 0;
    z0 = Zarr(1);

    MH = zeros(1,nn);

    MaxZ = -1000;

    for nn = 1:size(tr,2)
        clear Xt Zt Xarr Zarr
        Xt = tr(nn).X;
        Zt = tr(nn).Y./cos(pi/6);
        Xarr = Xt.*cos(-theta) + Zt.*-sin(-theta)-x0;
        Zarr =(Xt.*sin(-theta) + Zt.*cos(-theta)-z0).*(-1);
        if max(Zarr)>MaxZ
            [MaxZ MaxZ_ind] = max(Zarr);
            MaxZ_x = Xarr(MaxZ_ind);
        end
    end
```

```
for nn = 1:size(tr,2)
    clear Xt Zt Xarr Zarr
    Xt = tr(nn).X;
    Zt = tr(nn).Y./cos(pi/6);
    Xarr = Xt.*cos(-theta) + Zt.*-sin(-theta)-x0;
    Zarr =(Xt.*sin(-theta) + Zt.*cos(-theta)-z0).*(-1);

    P_MH(nn)  = tr(nn).p;
    T_MH(nn)  = tr(nn).t;
    CH_x(nn)  = (min(Xarr) + max(Xarr))/2;

    [MH(nn) mxh_ind] = max(Zarr);
    [MinH(nn) mnh_ind] = min(Zarr);
    if mxh_ind<CH_x(nn)/2 || mxh_ind>CH_x(nn)*3/2
        H(nn) = MH(nn);
    else
        H(nn) = MinH(nn);
    end

    [MaxZ_xn MaxZ_ind] = min(abs(Xarr-MaxZ_x));
    HH(nn) = Zarr(MaxZ_ind);

end

HHn = HH - HH(1); P_MHn = P_MH - P_MH(1);
MaxZ = max(HHn);
MaxP = max(P_MHn);
figure, plot(T_MH,(P_MHn)./MaxP,'b')
hold on; plot(T_MH,(HHn)./abs(MaxZ),'r')
title('Pressure and Deformation vs. Time')
xlabel('Time (s)')
```

```
    ylabel('Norm. Pressure & Norm. Max Deformation')
    legend('Norm. Pressure','Norm. Max Deformation')
    ylim([-1.2 1.2])

    figure, hold on;
    title('Maximum Deformation vs. Pressure')
    box on; grid on;
    xlabel('Pressure (in H_2O)');
    ylabel('Max Deformation (mm)');

    dx = 0.0118; % based on the common calibration factor
    plot(P_MH,HH.*dx)


% ------------- saving into a file -----------------

FileName= seldir(1:end-1);
FN = find(FileName=='\');
FileName=FileName(FN(end)+1:end);
% All data  W/O calibration (for x,y,z), W/O angle correction (for y,z)
save([FileName,'_Analyzed_Data.mat'],'tr')

%*****************************************
```

B.2 Generating 3D surfaces and making 3D movies

This code generates 3D patterns of deformation for two purposes: extracting the geometrical fluid flow as well as saving high quality 3D images and movies for publications and presentations:

```
% By Behrouz Tavakol - Last modified on 12/09/2012
% Combines different slices and generates a 3D surface
% -----------------------

clear all; close all; clc

% ------- The desired folder for analysis ... ----------

seldir= uigetdir('',...
    'Please select the folder containing different slices');
if seldir ==0
    seldir = '';
else
    seldir = [seldir,'\'];
end

% ------- Reading data from .mat files ... ----------

Filelist = dir([seldir,'*.mat']);

i = 1;
nn = size(Filelist,1);
while i<=nn
   if size(strfind(lower(Filelist(i).name),'analyzed_data'),2)==0
       Filelist(i)=[];
       nn = size(Filelist,1);
   else
       i = i+1;
   end
end
```

```
clear tr Vrn Trn V T Z
for nn=1:size(Filelist,1)

    data = load([seldir,Filelist(nn).name],'tr');
    tr{nn} = data.tr;
    Ytr(nn) = tr{nn}(1).z;
end

% --------- sorting based on z (y) values -----------

% positive: further from the camera
% negative: closer to the camera

sy = size(Filelist,1);
[Y Yind] = sort(Ytr);

for nn=1:sy
   trn{nn} = tr{Yind(nn)};
   for i=1:size(trn{nn},2)
        trn{nn}(i).used = 0;
        trn{nn}(i).Y = trn{nn}(i).Y ./ cos(pi/6);
        Vrn{nn}(i) = trn{nn}(i).v;
        Trn{nn}(i) = trn{nn}(i).t;
    end
    sx(nn)= size(Vrn{nn},2);
    Y(nn) = trn{nn}(1).z;
end
clear tr

% --------- Matching the positions of different slices --------------

for nn=1:sy
```

```
    clear Xt Zt
    Xt = trn{nn}(1).X;
    Zt = trn{nn}(1).Y;

    theta(nn) = atan((mean(Zt(end-4:end))-mean(Zt(1:5)))/...
                     (mean(Xt(end-4:end))-mean(Xt(1:5))));
    Xarr{nn} = Xt.*cos(-theta(nn)) + Zt.*-sin(-theta(nn));
    Zarr{nn} = Xt.*sin(-theta(nn)) + Zt.*cos(-theta(nn));

    x0(nn) = 0;
    z0(nn) = mean(Zarr{nn}(1:5));
end

nn = 7;
figure, hold on
for i=1:5:size(trn{nn},2)
    plot(trn{nn}(i).X,trn{nn}(i).Y,'Color',[1/i 1-1/i 1-1/i])
end

clear Xarr Zarr
for nn=1:sy
    % Finding V maximum voltage
    [vmax vmax_ind(nn)] = max(Vrn{nn});
    [vo v_ind(nn)] = min(abs(Vrn{nn}(1:vmax_ind(nn))-vmax));
    clear Xt Zt
    Xt = trn{nn}(v_ind(nn)).X;
    Zt = trn{nn}(v_ind(nn)).Y;
    Xarr{nn} = Xt.*cos(-theta(nn)) + Zt.*-sin(-theta(nn))-x0(nn);
    Zarr{nn} =(Xt.*sin(-theta(nn)) + Zt.*cos(-theta(nn))-z0(nn)).*(-1);
end
```

```
y0ind = find(Y==0);
zmax = max(Zarr{y0ind});
zmin = min(Zarr{y0ind});

xn = load( 'xn_2013.mat','xn', '-ascii');
zn = load( 'zn_2013.mat','zn', '-ascii');

% ------------------------- Calibration ---------------------------

[filename, pathname] = uigetfile({'*.TIFF';'*.*'}, 'Select an image file');
if isequal(filename,0)
    disp('User selected Cancel')
    sx = max(Xarr{y0ind})-min(Xarr{y0ind}); % px (apparent length in x)
    lx = 13.4; % mm (real length in x)
    dx = lx/sx % Calibration factor
else
    I1 = imread([pathname,filename]);
    x0(1:sy) = round(size(I1,2)/2);
    figure, imshow(I1)
    hold on
    [cx1,cy1] = ginput(1);
    plot(cx1,cy1,'b+')
    [cx2,cy2] = ginput(1);
    plot(cx2,cy2,'b+')
    line([cx1 cx2],[cy1 cy2], 'Color','b');
    dxy= inputdlg({'Length of first line (mm):'},'Calibration...',...
                   1,{'13.45'});
    if isempty(dxy)
        lx = 1;
    else
        lx = str2double(dxy(1));
    end
```

```
    dx = lx/sqrt((cx2-cx1)^2+(cy2-cy1)^2)
end

close

% dx = 0.0116 for most cases of this experiment

% -------- Genrating the surface for a specific Voltage/Time ------------

vmax = 7600;
vmin = 6800;
vint = 200;
fps = 100/vint;

% --------------- Initialization for saving avi movie -----------------

avifile = VideoWriter(['movie_',date],'MPEG-4');
avifile.FrameRate = fps;
avifile.Quality = 100;
open(avifile);

% -------- Initialization of main surface figure
figure('color',[1 1 1],'position', [0 0 1920 1280]);

view(gca,[-26.5 56]);

zlim(1.2*dx.*[zmin-1 zmax])
set(gca,'CLim',dx.*[zmin,zmax])
colorbar('peer',gca,[0.18 0.411 0.0127 0.347],'LineWidth',1);

set(gca,'nextplot','replacechildren');
set(gcf,'Renderer','zbuffer');
```

```
uiwait(gcf,3)
refreshdata


% --- Finding the corresponding indices for a specific voltage/time ----



mn = 0;
vv = [vmin:vint:vmax , vmax-vint:-vint:vmin];
VVind = zeros(size(vv,2),sy);
for v = vv

mn = mn+1;
clear Xarr Zarr V T

for nn=1:sy
    if mn<= round(size(vv,2)/2+0.1)
        [vo v_ind(nn)] = min(abs(Vrn{nn}(1:vmax_ind(nn))-v));
        Temp = 'V_Up';
    else
        [vo v_ind(nn)] = min(abs(Vrn{nn}(vmax_ind(nn):end)-v));
        v_ind(nn) = v_ind(nn)+vmax_ind(nn)-1;
        Temp = 'V_Down';
    end
    clear Xt Zt
    Xt = trn{nn}(v_ind(nn)).X;
    Zt = trn{nn}(v_ind(nn)).Y;
    Xarr{nn}=(Xt.*cos(-theta(nn))+Zt.*-sin(-theta(nn))-x0(nn)+xn(nn)).*dx;
    Zarr{nn}=(Xt.*sin(-theta(nn))+Zt.*cos(-theta(nn))-z0(nn)-zn(nn)).*(-1).*dx;

end
```

```
% ------ Filling (interpolating) the empty cells -------

Xg = []; Yg = []; Zg = [];
for nn=1:sy

    i = size(Xg,2);
    j = size(Xarr{nn},2);
    Zg(i+1:i+j)= Zarr{nn};
    Xg(i+1:i+j)= Xarr{nn};
    Yg(i+1:i+j)= Y(nn);
end

ylin = linspace(min(Y),max(Y),100);
xlin = linspace(min(Xg),max(Xg),100);
[xq,yq] = meshgrid(xlin,ylin);
zq = griddata(Xg,Yg,Zg,xq,yq,'cubic');
surf(xq,yq,zq)

% Overlaying desired cross sectional curvatures
hold on
for nn=7:7 % or 1:sy if you want all cross sections
    i = size(Xarr{nn},2);
    clear Yy
    Yy(1:i)= Y(nn);
    plot3(Xarr{nn},Yy,Zarr{nn},'linewidth',4,'Color',[0,1,0])
end
hold off
grid off;
zlim(1.2*dx.*[zmin-1 zmax])
set(gca,'CLim',dx.*[zmin,zmax])
```

```
colorbar('peer',gca,[0.18 0.411 0.0127 0.347],'LineWidth',1);
set(gca,'nextplot','replacechildren');
set(gcf,'Renderer','zbuffer');
axis off;

view(gca,[-26.5 56]);

uiwait(gcf,1)
refreshdata
print('-dtiff', '-r1200',['3D_Map_',date,'_', num2str(v),Temp,'.tiff'])


frames(mn).xq = xq;
frames(mn).yq = yq;
frames(mn).zq = zq;
frames(mn).v  = v;
VVind(mn,:) = v_ind;

frame = getframe;
writeVideo(avifile,frame);

end


close(avifile);
% ------------- saving into a file -----------------

FileName= seldir(1:end-1);
FN = find(FileName=='\');
FileName=FileName(FN(end)+1:end);
save([FileName,'_SurfaceMesh.mat'],'frames')
```

Appendix C. Mathematica Codes

The following Mathematica script is written to examine the validity of the analytical solutions of Extended Lubrication Theory provided in Chapter 3. The code is parametric, so we only need to substitute an appropriate shape function for obtaining the analytical solutions associated with that shape.

Written by: Behrouz Tavakol (btavakol@vt.edu)
Version: *Mathematica* 9.0 and higher

Extended Lubrication Theory

In[1]:=
```
Clear["Global`*"]
Needs["PlotLegends`"]
```

General::obspkg : PlotLegends` is now obsolete. The legacy version being loaded may conflict with current functionality. See the Compatibility Guide for updating information.

Primary dimensionless equations are:

In[3]:=

$$eq1 = \partial_{\{X,1\}} U[X] + \partial_{\{Y,1\}} V[Y] == 0$$
$$eq2 = \delta^2 \partial_{\{X,2\}} U[X] + \partial_{\{Y,2\}} U[Y] == \partial_{\{X,1\}} P[X]$$
$$eq2 = \delta^4 \partial_{\{X,2\}} V[X] + \delta^2 \partial_{\{Y,2\}} V[Y] == \partial_{\{Y,1\}} P[Y]$$

Out[3]= $U'[X] + V'[Y] == 0$

Out[4]= $\delta^2 U''[X] + U''[Y] == P'[X]$

Out[5]= $\delta^4 V''[X] + \delta^2 V''[Y] == P'[Y]$

The boundary conditions are:

In[6]:=

$$BC1 = U[0] == 0$$
$$BC2 = U[H[X]] == 0$$
$$BC3 = \int_0^{H[X]} U[X,Y] dY == 1$$

Out[6]= $U[0] == 0$

Out[7]= $U[H[X]] == 0$

Out[8]= $\int_0^{H[X]} U[X, Y] dY == 1$

Perturbation Expansion:
U[X,Y;δ] = U0[X,Y] + δ^2 U2[X,Y] + δ^4 U4[X,Y]+...
V[X,Y;δ] = V0[X,Y] + δ^2 V2[X,Y] + δ^4 V4[X,Y]+...
P[X,Y;δ] = P0[X,Y] + δ^2 P2[X,Y] + δ^4 P4[X,Y]+...
Pluging into primary dimensionless equations and sorting w.r.t δ coefficients, we have:

Shape Function

In[9]:=
```
Shape = 1 - λ / 2 (1 + Cos[π X]);                    (* eq 10 *)
Plot[{Shape /. λ → 0, Shape /. λ → 0.25, Shape /. λ → 0.5,
  Shape /. λ → 0.75, Shape /. λ → 1}, {X, -1, 1}, Frame → True]
```

Out[10]=

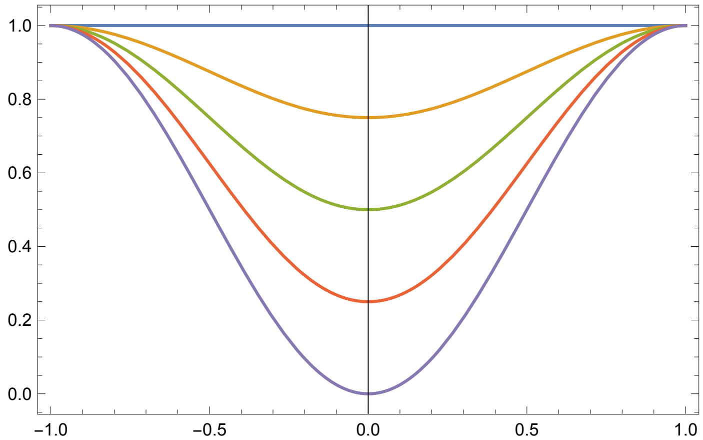

Leading Order

In[11]:=
```
eq1LeadingOrder = ∂{X,1}U0[X]+∂{Y,1}V0[Y] == 0    (* eq 6 *)
eq2LeadingOrder = ∂{Y,2}U0[Y]-∂{X,1}P0[X] == 0    (* eq 6 *)
eq3LeadingOrder = ∂{Y,1}P0[Y] == 0                (* eq 6 *)
BC1LeadingOrder = U0[0] == 0;
BC2LeadingOrder = U0[H[X]] == 0;
BC3LeadingOrder = ∫_0^H[X] U0[Y] dY == 1;
```

Out[11]= $U0'[X] + V0'[Y] == 0$

Out[12]= $-P0'[X] + U0''[Y] == 0$

Out[13]= $P0'[Y] == 0$

In[17]:=
```
U0Sol = Simplify[DSolve[{eq2LeadingOrder, BC1LeadingOrder, BC2LeadingOrder},
                        {U0[Y]}, Y]][[1]][[1]]
(* eq 7 *)
```

Out[17]= $U0[Y] \to \frac{1}{2} Y (Y - H[X]) P0'[X]$

In[18]:=
```
dP0dXSol = Solve[BC3LeadingOrder /. U0Sol, P0′[X]][[1]][[1]]
(* eq 8 *)
```

Out[18]= $P0'[X] \to -\frac{12}{H[X]^3}$

In[19]:=
```
U0Sol = U0Sol /. dP0dXSol
(* eq 9 *)
```

Out[19]= $U0[Y] \to -\frac{6\, Y\, (Y - H[X])}{H[X]^3}$

In[20]:= $V0 = \text{Simplify}\left[-\int_0^Y \partial_{\{X,1\}} (U0[Y] \text{ /. } U0Sol)\, dY\right]$

```
(* eq's 12 & 13 *)
```

Out[20]= $-\frac{6\, Y^2\, (Y - H[X])\, H'[X]}{H[X]^4}$

In[21]:=
```
(* Comparing V0 and eq 13 *)
```

$\text{Simplify}\left[\;2\, Y^3\, \partial_{\{X,1\}} \left(H[X]^{-3}\right) - 3\, Y^2\, \partial_{\{X,1\}} \left(H[X]^{-2}\right) - V0\;\right]$

Out[21]= 0

Verifying the other two boundary conditions: V0 (X, Y=0) = 0 & V0 (X, Y = H(X)) = 0

In[22]:=
```
V0 /. Y → 0
V0 /. Y → H[X]      (* eq 14 *)
```

Out[22]= 0

Out[23]= 0

Yes! Boundary conditions are all satisfied.

Applying the shape function:

In[24]:=
```
P0′[X] /. dP0dXSol /. H[X] → Shape
```

Out[24]= $-\frac{12}{\left(1 - \frac{1}{2}\, \lambda\, (1 + \text{Cos}[\pi\, X])\right)^3}$

In[25]:= $\text{DelP0} = \text{Simplify}\left[-\int_{-1}^{1} (P0'[X] \text{ /. } dP0dXSol \text{ /. } H[X] \to Shape)\, dX,\right.$

$\left.\quad \text{Assumptions} \to \{\lambda \in \text{Reals}, -1 < \lambda < 1, \lambda \neq 0\}\right]$ (* eq 11 *)

Out[25]= $\frac{3\left(8 - 8\, \lambda + 3\, \lambda^2\right)}{(1 - \lambda)^{5/2}}$

Second Order

In[26]:=
```
eq1SecondOrder = ∂{X,1}U2[X]+∂{Y,1}V2[Y] == 0                                   (* eq 15c *)
eq2SecondOrder = ∂{Y,2}U2[Y]-∂{X,1}P2[X] == Expand[-∂{X,2}(U0[Y]/.U0Sol)]        (* eq 15a *)
eq3SecondOrder = ∂{Y,1}P2[Y] == ∂{Y,2}V0                                        (* eq 15b *)
BC1SecondOrder = U2[0] == 0;
BC2SecondOrder = U2[H[X]] == 0;
BC3SecondOrder = ∫_0^H[X] U2[Y] dY == 0;
```

Out[26]= $U2'[X] + V2'[Y] == 0$

Out[27]= $-P2'[X] + U2''[Y] == \frac{72\,Y^2\,H'[X]^2}{H[X]^5} - \frac{36\,Y\,H'[X]^2}{H[X]^4} - \frac{18\,Y^2\,H''[X]}{H[X]^4} + \frac{12\,Y\,H''[X]}{H[X]^3}$

Out[28]= $P2'[Y] == \frac{(-24\,Y - 12\,(Y - H[X]))\,H'[X]}{H[X]^4}$

In[32]:=
```
P2Sol = FullSimplify[DSolve[{eq3SecondOrder}, {P2[Y]}, {Y}]][[1]][[1]]
P2Sol = P2Sol /. C[1] → C3[X]
Simplify[-∂{X,1}(U0[Y] /. U0Sol)]
```

Out[32]= $P2[Y] \to C[1] + \frac{6\,Y\,(-3\,Y + 2\,H[X])\,H'[X]}{H[X]^4}$

Out[33]= $P2[Y] \to C3[X] + \frac{6\,Y\,(-3\,Y + 2\,H[X])\,H'[X]}{H[X]^4}$

Out[34]= $-\frac{6\,Y\,(3\,Y - 2\,H[X])\,H'[X]}{H[X]^4}$

In[35]:=
```
aa = eq2SecondOrder /. P2'[X] → ∂{X,1}(P2[Y] /. P2Sol);
U2Sol = Expand[FullSimplify[
         DSolve[{aa, BC1SecondOrder, BC2SecondOrder}, {U2[Y]}, Y]]][[1]][[1]]
(* eq 18 *)
```

Out[36]= $U2[Y] \to$
$\frac{1}{2}\,Y^2\,C3'[X] - \frac{1}{2}\,Y\,H[X]\,C3'[X] + \frac{12\,Y^4\,H'[X]^2}{H[X]^5} - \frac{12\,Y^3\,H'[X]^2}{H[X]^4} - \frac{3\,Y^4\,H''[X]}{H[X]^4} + \frac{4\,Y^3\,H''[X]}{H[X]^3} - \frac{Y\,H''[X]}{H[X]}$

In[37]:=
```
(* Comparing this result to eq. 18: *)
Expand[
 (-2 ∂{X,2}(H[X]^-2) (Y^3 - H[X]^2 Y) + ∂{X,2}(H[X]^-3) (Y^4 - H[X]^3 Y) + 1/2 C3'[X] (Y^2 - H[X] Y))
         - (U2[Y] /. U2Sol)]
```

Out[37]= 0

In[38]:=
```
dC3dXSol = Solve[BC3SecondOrder /. U2Sol, C3′[X]][[1]][[1]]
(* eq 19 *)
```

Out[38]= $C3'[X] \to -\frac{6\left(6\,H'[X]^2 + H[X]\,H''[X]\right)}{5\,H[X]^3}$

In[39]:=
```
(* Comparing this result to eq. 19: *)
```
$\text{FullSimplify}\left[\left(6\,\partial_{\{X,2\}}\left(H[X]^{-2}\right)H[X] - \frac{18}{5}\,\partial_{\{X,2\}}\left(H[X]^{-3}\right)H[X]^2\right) - (C3'[X]\ /.\ dC3dXSol)\right]$

Out[39]= 0

In[40]:=
```
U2SolFul = U2Sol /. dC3dXSol
```

Out[40]= $U2[Y] \to \frac{12\,Y^4\,H'[X]^2}{H[X]^5} - \frac{12\,Y^3\,H'[X]^2}{H[X]^4} - \frac{3\,Y^4\,H''[X]}{H[X]^4} + \frac{4\,Y^3\,H''[X]}{H[X]^3} - \frac{Y\,H''[X]}{H[X]} - \frac{3\,Y^2\left(6\,H'[X]^2 + H[X]\,H''[X]\right)}{5\,H[X]^3} + \frac{3\,Y\left(6\,H'[X]^2 + H[X]\,H''[X]\right)}{5\,H[X]^2}$

In[41]:=
$V2 = \text{Expand}\left[-\int_0^Y \partial_{\{X,1\}}\left(U2[Y]\ /.\ U2SolFul\right)\, dY\right]$
```
(* eq 21) *)
```

Out[41]= $\frac{12\,Y^5\,H'[X]^3}{H[X]^6} - \frac{12\,Y^4\,H'[X]^3}{H[X]^5} - \frac{18\,Y^3\,H'[X]^3}{5\,H[X]^4} + \frac{18\,Y^2\,H'[X]^3}{5\,H[X]^3} - \frac{36\,Y^5\,H'[X]\,H''[X]}{5\,H[X]^5} + \frac{9\,Y^4\,H'[X]\,H''[X]}{H[X]^4} + \frac{2\,Y^3\,H'[X]\,H''[X]}{H[X]^3} - \frac{19\,Y^2\,H'[X]\,H''[X]}{5\,H[X]^2} + \frac{3\,Y^5\,H^{(3)}[X]}{5\,H[X]^4} - \frac{Y^4\,H^{(3)}[X]}{H[X]^3} + \frac{Y^3\,H^{(3)}[X]}{5\,H[X]^2} + \frac{Y^2\,H^{(3)}[X]}{5\,H[X]}$

Using the shape function

In[42]:=
```
dC3dX = FullSimplify[
  C3′[X] /. dC3dXSol /. {H[X] → Shape, H′[X] → ∂{X,1}(Shape), H″[X] → ∂{X,2}(Shape)}]
```

Out[42]= $-\frac{6\,\pi^2\,\lambda\,\left(2\,(-2+\lambda)\,\text{Cos}[\pi X] + \lambda\,(-5 + 7\,\text{Cos}[2\,\pi X])\right)}{5\,(-2+\lambda+\lambda\,\text{Cos}[\pi X])^3}$

In[43]:=
$DelP2 = \text{Simplify}\left[-\int_{-1}^{1} dC3dX\, dX,\ \text{Assumptions} \to \{\lambda \in \text{Reals},\ 1 > \lambda > -1,\ \lambda \neq 0\}\right]$
```
(* eq 20 *)
```

Out[43]= $\frac{12\,\pi^2\,\lambda^2}{5\,(1-\lambda)^{3/2}}$

Comparison of the second-order pressure drop between first and second cases:

In[44]:=
```
Plot[{DelP0, DelP2 }, {λ , 0, 1}]
```

Out[44]=

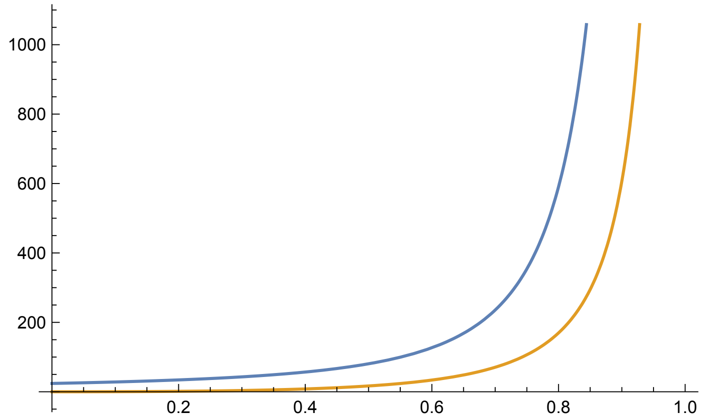

Fourth Order

In[45]:=
```
eq1FourthOrder = ∂{x,1}U4[X]+∂{Y,1}V4[Y] == 0                               (* eq 22a *)
eq2FourthOrder = ∂{Y,2}U4[Y]-∂{x,1}P4[X] == Expand[-∂{x,2}(U2[Y]/.U2Sol)]    (* eq 22b *)
eq3FourthOrder = ∂{Y,1}P4[Y] == Expand[Simplify[∂{Y,2}V2 +∂{x,2}V0]]         (* eq 22c *)
BC1FourthOrder = U4[0] == 0;
BC2FourthOrder = U4[H[X]] == 0;
BC3FourthOrder = ∫_0^H[X] U4[Y]dY == 0;
```

Out[45]= $U4'[X] + V4'[Y] == 0$

Out[46]= $$-P4'[X] + U4''[Y] == -\frac{360\,Y^4\,H'[X]^4}{H[X]^7} + \frac{240\,Y^3\,H'[X]^4}{H[X]^6} + Y\,H'[X]\,C3''[X] + \frac{1}{2}\,Y\,C3'[X]\,H''[X] + \frac{360\,Y^4\,H'[X]^2\,H''[X]}{H[X]^6} - \frac{288\,Y^3\,H'[X]^2\,H''[X]}{H[X]^5} + \frac{2\,Y\,H'[X]^2\,H''[X]}{H[X]^3} - \frac{36\,Y^4\,H''[X]^2}{H[X]^5} + \frac{36\,Y^3\,H''[X]^2}{H[X]^4} - \frac{Y\,H''[X]^2}{H[X]^2} - \frac{1}{2}\,Y^2\,C3^{(3)}[X] + \frac{1}{2}\,Y\,H[X]\,C3^{(3)}[X] - \frac{48\,Y^4\,H'[X]\,H^{(3)}[X]}{H[X]^5} + \frac{48\,Y^3\,H'[X]\,H^{(3)}[X]}{H[X]^4} - \frac{2\,Y\,H'[X]\,H^{(3)}[X]}{H[X]^2} + \frac{3\,Y^4\,H^{(4)}[X]}{H[X]^4} - \frac{4\,Y^3\,H^{(4)}[X]}{H[X]^3} + \frac{Y\,H^{(4)}[X]}{H[X]}$$

Out[47]= $$P4'[Y] == \frac{120\,Y^3\,H'[X]^3}{H[X]^6} - \frac{72\,Y^2\,H'[X]^3}{H[X]^5} - \frac{108\,Y\,H'[X]^3}{5\,H[X]^4} + \frac{36\,H'[X]^3}{5\,H[X]^3} - \frac{72\,Y^3\,H'[X]\,H''[X]}{H[X]^5} + \frac{54\,Y^2\,H'[X]\,H''[X]}{H[X]^4} + \frac{12\,Y\,H'[X]\,H''[X]}{H[X]^3} - \frac{38\,H'[X]\,H''[X]}{5\,H[X]^2} + \frac{6\,Y^3\,H^{(3)}[X]}{H[X]^4} - \frac{6\,Y^2\,H^{(3)}[X]}{H[X]^3} + \frac{6\,Y\,H^{(3)}[X]}{5\,H[X]^2} + \frac{2\,H^{(3)}[X]}{5\,H[X]}$$

In[51]:=
```
P4Sol = Expand[FullSimplify[DSolve[{eq3FourthOrder}, {P4[Y]}, {Y}]]][[1]][[1]];
P4Sol = P4Sol /. C[1] → C5[X]    (* eq 23 *)
```

Out[52]=
$$P4[Y] \to C5[X] + \frac{30\,Y^4\,H'[X]^3}{H[X]^6} - \frac{24\,Y^3\,H'[X]^3}{H[X]^5} - \frac{54\,Y^2\,H'[X]^3}{5\,H[X]^4} + \frac{36\,Y\,H'[X]^3}{5\,H[X]^3} - \frac{18\,Y^4\,H'[X]\,H''[X]}{H[X]^5} + \frac{18\,Y^3\,H'[X]\,H''[X]}{H[X]^4} + \frac{6\,Y^2\,H'[X]\,H''[X]}{H[X]^3} - \frac{38\,Y\,H'[X]\,H''[X]}{5\,H[X]^2} + \frac{3\,Y^4\,H^{(3)}[X]}{2\,H[X]^4} - \frac{2\,Y^3\,H^{(3)}[X]}{H[X]^3} + \frac{3\,Y^2\,H^{(3)}[X]}{5\,H[X]^2} + \frac{2\,Y\,H^{(3)}[X]}{5\,H[X]}$$

In[53]:=
```
eq4subs = eq2FourthOrder /. P4′[X] → ∂{X,1} (P4[Y] /. P4Sol);
U4Sol = Expand[FullSimplify[
        DSolve[{eq4subs, BC1FourthOrder, BC2FourthOrder}, {U4[Y]}, Y]]][[1]][[1]]
(* eq 27 *)
```

Out[54]=
$$U4[Y] \to \frac{1}{2}\,Y^2\,C5'[X] - \frac{1}{2}\,Y\,H[X]\,C5'[X] - \frac{18\,Y^6\,H'[X]^4}{H[X]^7} + \frac{18\,Y^5\,H'[X]^4}{H[X]^6} + \frac{18\,Y^4\,H'[X]^4}{5\,H[X]^5} - \frac{18\,Y^3\,H'[X]^4}{5\,H[X]^4} + \frac{1}{6}\,Y^3\,H'[X]\,C3''[X] - \frac{1}{6}\,Y\,H[X]^2\,H'[X]\,C3''[X] + \frac{1}{12}\,Y^3\,C3'[X]\,H''[X] - \frac{1}{12}\,Y\,H[X]^2\,C3'[X]\,H''[X] + \frac{18\,Y^6\,H'[X]^2\,H''[X]}{H[X]^6} - \frac{108\,Y^5\,H'[X]^2\,H''[X]}{5\,H[X]^5} - \frac{21\,Y^4\,H'[X]^2\,H''[X]}{5\,H[X]^4} + \frac{97\,Y^3\,H'[X]^2\,H''[X]}{15\,H[X]^3} + \frac{4\,Y\,H'[X]^2\,H''[X]}{3\,H[X]} + \frac{1}{30}\,Y\,H''[X]^2 - \frac{9\,Y^6\,H''[X]^2}{5\,H[X]^5} + \frac{27\,Y^5\,H''[X]^2}{10\,H[X]^4} + \frac{Y^4\,H''[X]^2}{2\,H[X]^3} - \frac{43\,Y^3\,H''[X]^2}{30\,H[X]^2} - \frac{1}{24}\,Y^4\,C3^{(3)}[X] + \frac{1}{12}\,Y^3\,H[X]\,C3^{(3)}[X] - \frac{1}{24}\,Y\,H[X]^3\,C3^{(3)}[X] + \frac{1}{15}\,Y\,H'[X]\,H^{(3)}[X] - \frac{12\,Y^6\,H'[X]\,H^{(3)}[X]}{5\,H[X]^5} + \frac{18\,Y^5\,H'[X]\,H^{(3)}[X]}{5\,H[X]^4} + \frac{2\,Y^4\,H'[X]\,H^{(3)}[X]}{5\,H[X]^3} - \frac{5\,Y^3\,H'[X]\,H^{(3)}[X]}{3\,H[X]^2} + \frac{3\,Y^6\,H^{(4)}[X]}{20\,H[X]^4} - \frac{3\,Y^5\,H^{(4)}[X]}{10\,H[X]^3} + \frac{Y^4\,H^{(4)}[X]}{20\,H[X]^2} + \frac{7\,Y^3\,H^{(4)}[X]}{30\,H[X]} - \frac{2}{15}\,Y\,H[X]\,H^{(4)}[X]$$

In[55]:=
```
C3Peq = C3′[X] /. dC3dXSol
FullSimplify[
  (∂{X,4} (H[X]^-3) Y^4 - 2 ∂{X,4} (H[X]^-2) Y^3 +
     (-∂{X,2} (H[X]^3 ∂{X,2} (H[X]^-3)) + 2 ∂{X,2} (H[X]^2 ∂{X,2} (H[X]^-2))) Y -
     C3‴[X] Y^2 + (∂{X,2} (H[X] C3′[X])) Y + C5′[X]) /.
   {C3′[X] → C3Peq, C3″[X] → ∂{X,1} (C3Peq), C3‴[X] → ∂{X,2} (C3Peq)}]
(* eq 25 modified *)
```

Out[55]=
$$-\frac{6\left(6\,H'[X]^2+H[X]\,H''[X]\right)}{5\,H[X]^3}$$

Out[56]=
$$\frac{1}{5\,H[X]^7}\Big(5\,H[X]^7\,C5'[X]+1800\,Y^4\,H'[X]^4-600\,Y^3\,H[X]\,H'[X]^2\left(2\,H'[X]^2+3\,Y\,H''[X]\right)+5\,Y\,H[X]^8\,C3^{(3)}[X]+$$
$$12\,Y^2\,H[X]^2\left(36\,H'[X]^4+120\,Y\,H'[X]^2\,H''[X]+15\,Y^2\,H''[X]^2+20\,Y^2\,H'[X]\,H^{(3)}[X]\right)-$$
$$5\,Y\,H[X]^6\,H^{(4)}[X]+Y\,H[X]^5\left(-H''[X]^2-2\,H'[X]\,H^{(3)}[X]+6\,Y\,H^{(4)}[X]\right)+$$
$$2\,Y\,H[X]^4\left(-83\,H'[X]^2\,H''[X]+24\,Y\,H'[X]\,H^{(3)}[X]+10\,Y\left(3\,H''[X]^2+Y\,H^{(4)}[X]\right)\right)-$$
$$3\,Y\,H[X]^3\left(-72\,H'[X]^4+168\,Y\,H'[X]^2\,H''[X]+80\,Y^2\,H'[X]\,H^{(3)}[X]+5\,Y^2\left(12\,H''[X]^2+Y\,H^{(4)}[X]\right)\right)\Big)$$

In[57]:=
```
dC5dXSol = Simplify[Solve[BC3FourthOrder /. U4Sol, C5′[X]]][[1]][[1]]
(* eq 28 *)
```

Out[57]=
$$C5'[X]\to\frac{1}{700\,H[X]^3}\Big(2088\,H'[X]^4+3484\,H[X]\,H'[X]^2\,H''[X]-2\,H'[X]\left(175\,H[X]^4\,C3''[X]+194\,H[X]^2\,H^{(3)}[X]\right)-$$
$$H[X]^2\left(175\,H[X]^2\,C3'[X]\,H''[X]+410\,H''[X]^2+70\,H[X]^3\,C3^{(3)}[X]+226\,H[X]\,H^{(4)}[X]\right)\Big)$$

In[58]:=
```
FullSimplify[eq2FourthOrder /. {U4″[Y] → ∂{Y,2} (U4[Y] /. U4Sol), C5′[X] → dC5dXSol}]
```

Out[58]=
$$\frac{1}{H[X]}\Big(-1800\,Y^4\,H'[X]^4+2\,H[X]\Big(5\,H[X]^6\,(C5'[X]-P4'[X])+$$
$$300\,Y^3\,H'[X]^2\left(2\,H'[X]^2+3\,Y\,H''[X]\right)-2\,Y\,H[X]^4\left(19\,H''[X]^2+20\,H'[X]\,H^{(3)}[X]\right)+$$
$$2\,Y\,H[X]^3\left(92\,H'[X]^2\,H''[X]+15\,Y\,H''[X]^2+12\,Y\,H'[X]\,H^{(3)}[X]\right)+$$
$$6\,Y\,H[X]^2\left(-18\,H'[X]^4-42\,Y\,H'[X]^2\,H''[X]+15\,Y^2\,H''[X]^2+20\,Y^2\,H'[X]\,H^{(3)}[X]\right)-$$
$$6\,Y^2\,H[X]\left(-36\,H'[X]^4+120\,Y\,H'[X]^2\,H''[X]+15\,Y^2\,H''[X]^2+20\,Y^2\,H'[X]\,H^{(3)}[X]\right)\Big)+$$
$$Y\,H[X]^3\left(15\,Y^3-20\,Y^2\,H[X]+6\,Y\,H[X]^2+4\,H[X]^3\right)H^{(4)}[X]\Big)=0$$

In[59]:=
```
FullSimplify[eq2FourthOrder /. U4''[Y] → ∂{Y,2} (U4[Y] /. U4Sol) /. dC5dXSol]
```

Out[59]=
$$\frac{1}{H[X]}\Big(24\left(5250\,Y^4-3500\,Y^3 H[X]-1260\,Y^2 H[X]^2+630\,Y H[X]^3-87\,H[X]^4\right)H'[X]^4-4\,H[X]\left(31500\,Y^4-25200\,Y^3 H[X]-8820\,Y^2 H[X]^2+6440\,Y H[X]^3+871\,H[X]^4\right)H'[X]^2 H''[X]+2\,H[X]^2 H'[X]\Big(175\,H[X]^6\,C3''[X]+2\left(4200\,Y^4-4200\,Y^3 H[X]-840\,Y^2 H[X]^2+1400\,Y H[X]^3+97\,H[X]^4\right)H^{(3)}[X]\Big)+H[X]^2\Big(175\,H[X]^6\,C3'[X]\,H''[X]+12600\,Y^4 H''[X]^2+70\,H[X]^7\,C3^{(3)}[X]+H[X]^5\left(700\,P4'[X]+226\,H^{(4)}[X]\right)+10\,H[X]^4\left(41\,H''[X]^2-28\,Y H^{(4)}[X]\right)+140\,Y H[X]^3\left(38\,H''[X]^2-3\,Y H^{(4)}[X]\right)+1400\,Y^2 H[X]^2\left(-3\,H''[X]^2+Y H^{(4)}[X]\right)-1050\,Y^3 H[X]\left(12\,H''[X]^2+Y H^{(4)}[X]\right)\Big)\Big)=0$$

Here we show that $\frac{d^2 U_2}{dX^2}$ vanishes when X → {-1,1} if we plug any of the shape functions : (as long as H [X = -1] = H [X = 1] = 0)

In[60]:=
```
∂{X,1} (U2[Y] /. U2SolFul /.
   {H[X] → Shape, H'[X] → ∂{X,1} (Shape), H''[X] → ∂{X,2} (Shape)}) /. X → {-1, 1}
```

Out[60]= {0, 0}

Shape function:

In[61]:=
```
Simplify[∫_{-1}^{1} ∂{X,2} (U2[Y] /. U2SolFul /. {H[X] → Shape, H'[X] → ∂{X,1} (Shape),
      H''[X] → ∂{X,2} (Shape)}) dX , Assumptions → {λ ∈ Reals, 1 > λ > 0}]
```

Out[61]= 0

Also, $\frac{\partial^2}{\partial X^2}\int_0^Y V0(X, s)\,ds$ vanishes as X →{-1,1} [as long as $H'[X] = H'''[X] = 0$ when X→ {-1,1}] :

In[62]:=
```
∂{X,2} (∫_0^Y V0 dY) /. {H[X] → Shape, H'[X] → ∂{X,1} (Shape),
   H''[X] → ∂{X,2} (Shape), Derivative[3][H][X] → ∂{X,3} (Shape)} /. X → {-1, 1}
```

Out[62]= {0, 0}

Substituting the shape function

In[63]:=
```
dC5dX = C5'[X] /. dC5dXSol /. {C3'[X] → C3Peq, C3''[X] → ∂{X,1} (C3Peq),
   Derivative[3][C3][X] → ∂{X,2} (C3Peq)}; dC5dX = FullSimplify[
  dC5dX /. {H[X] → Shape, H'[X] → ∂{X,1} (Shape), H''[X] → ∂{X,2} (Shape),
    Derivative[3][H][X] → ∂{X,3} (Shape), Derivative[4][H][X] → ∂{X,4} (Shape)}]
```

Out[63]=
$$\frac{1}{5600\,(-2+\lambda+\lambda\,\mathrm{Cos}[\pi X])^3}\,\pi^4\,\lambda\Big(2\,(-2+\lambda)\,(1136+\lambda\,(-1136+651\,\lambda))\,\mathrm{Cos}[\pi X]+\lambda\Big(35\,(112+\lambda\,(-112+19\,\lambda))-48\,(153+\lambda\,(-153+35\,\lambda))\,\mathrm{Cos}[2\,\pi X]-4150\,(-2+\lambda)\,\lambda\,\mathrm{Cos}[3\,\pi X]-1833\,\lambda^2\,\mathrm{Cos}[4\,\pi X]\Big)\Big)$$

In[64]:=
```
DelP4 = FullSimplify[-∫_{-1}^{1} dC5dX dX, Assumptions → {λ ∈ Reals, 1 > λ > -1, λ ≠ 0}]
(* eq 29 *)
```

Out[64]=
$$-\frac{8\pi^4\left(-428\left(-1+\sqrt{1-\lambda}\right)+214\left(-2+\sqrt{1-\lambda}\right)\lambda+53\lambda^2\right)}{175\sqrt{1-\lambda}}$$

In[65]:=
```
(* If using the compact equation 28 provided in the text: *)
dC5dXTextSol = C5'[X] → (3/14 ∂{X,4}(H[X]^-3) H[X]^4 - 3/5 ∂{X,4}(H[X]^-2) H[X]^3 -
      (∂{X,2}(H[X]^3 ∂{X,2}(H[X]^-3)) - 2 ∂{X,2}(H[X]^2 ∂{X,2}(H[X]^-2))) H[X] +
      3/10 ∂{X,3}(C3[X]) H[X]^2 - 1/2 ∂{X,2}(H[X] C3'[X]) H[X]) /.
    {C3'[X] → C3Peq, C3''[X] → ∂{X,1}(C3Peq), Derivative[3][C3][X] → ∂{X,2}(C3Peq)};
```

In[66]:=
```
dC5dXText = FullSimplify[
  C5'[X] /. dC5dXTextSol /. {H[X] → Shape, H'[X] → ∂{X,1}(Shape), H''[X] → ∂{X,2}(Shape),
    Derivative[3][H][X] → ∂{X,3}(Shape), Derivative[4][H][X] → ∂{X,4}(Shape)}]
```

Out[66]=
$$\frac{1}{5600\,(-2+\lambda+\lambda\,\mathrm{Cos}[\pi X])^3}\pi^4\lambda\left(2\,(-2+\lambda)\,(1136+\lambda\,(-1136+651\lambda))\,\mathrm{Cos}[\pi X]+\lambda\left(35\,(112+\lambda\,(-112+19\lambda))-48\,(153+\lambda\,(-153+35\lambda))\,\mathrm{Cos}[2\pi X]-4150\,(-2+\lambda)\,\lambda\,\mathrm{Cos}[3\pi X]-1833\lambda^2\,\mathrm{Cos}[4\pi X]\right)\right)$$

In[67]:=
```
DelP4Text =
  FullSimplify[-∫_{-1}^{1} dC5dXText dX, Assumptions → {λ ∈ Reals, 1 > λ > -1, λ ≠ 0}]
```

Out[67]=
$$-\frac{8\pi^4\left(-428\left(-1+\sqrt{1-\lambda}\right)+214\left(-2+\sqrt{1-\lambda}\right)\lambda+53\lambda^2\right)}{175\sqrt{1-\lambda}}$$

In[68]:=
```
Simplify[DelP4 - DelP4Text]
```

Out[68]= 0

ΔP_0, ΔP_2, and ΔP_4 for the shape function

In[69]:=
```
Plot[{DelP0, DelP2, DelP4}, {λ , 0, 1}, PlotLegend → {"ΔP0", "ΔP2", "ΔP4"} ,
  LegendShadow → None, LegendBorder → None, LegendTextSpace → 0.7,
  LegendSpacing → 0.1, LegendPosition → {-0.6, 0.02}, LegendSize → 0.55,
  PlotStyle → {{Thick, Black}, {Thick, Red}, {Thick, Blue}}, FrameLabel → {λ, ΔP},
  Frame → True, FrameStyle → {{Directive[Thick, Black], FontSize → 18},
   {Directive[Thick, Black], FontSize → 18}, {Directive[Thick, Black],
    FontSize → 18}, {Directive[Thick, Black], FontSize → 18}}, ImageSize → Large]
```

Out[69]=

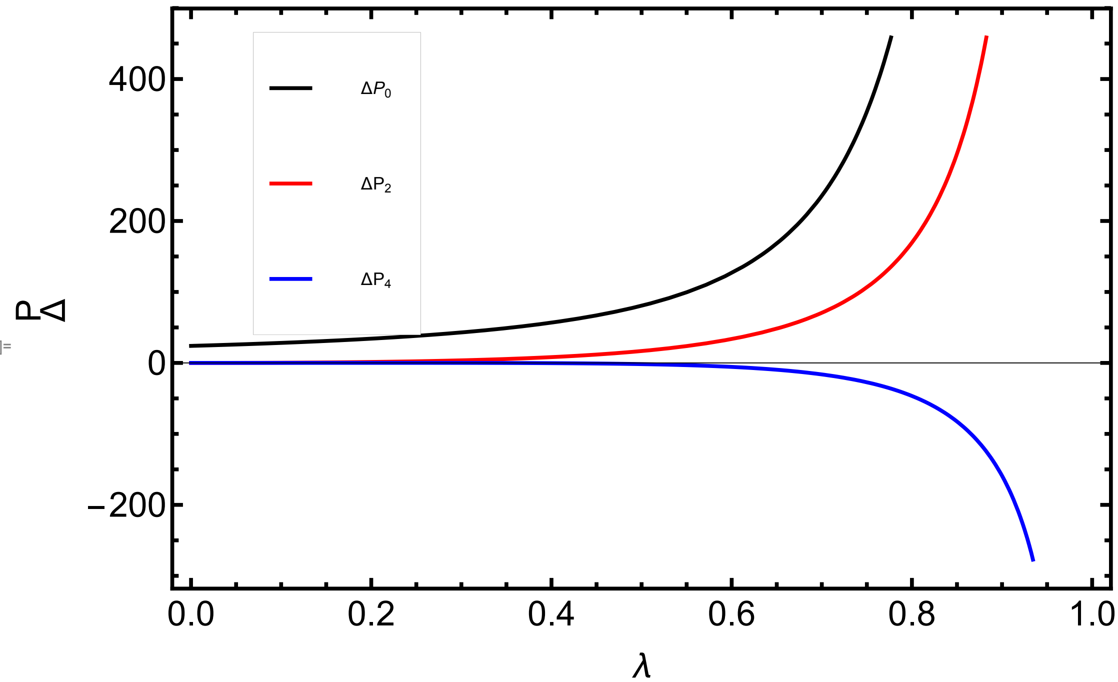

$\Delta P_{2n} = \sum_{i=0}^{2n} \Delta P_i$ and $Q_{2n} = C / \Delta P_{2n}$

In[70]:=
```
ΔP0 = DelP0
ΔP02 = DelP0 + d^2 DelP2
ΔP024 = DelP0 + d^2 DelP2 + d^4 DelP4
Plot[{ΔP0 /. d → 1, ΔP02 /. d → 1, ΔP024 /. d → 1}, {λ , 0, 1},
 PlotStyle → {{Thick, Black}, {Thick, Red}, {Thick, Blue, Dashed}},
 FrameLabel → {"λ", "ΔP"}, Frame → True,
 FrameStyle → {{Directive[Thick, Black], FontSize → 18},
   {Directive[Thick, Black], FontSize → 18}, {Directive[Thick, Black],
    FontSize → 18}, {Directive[Thick, Black], FontSize → 18}}, ImageSize → Large]
```

Out[70]= $$\frac{3\left(8-8\lambda+3\lambda^2\right)}{(1-\lambda)^{5/2}}$$

Out[71]= $$\frac{12\,d^2\pi^2\lambda^2}{5\,(1-\lambda)^{3/2}}+\frac{3\left(8-8\lambda+3\lambda^2\right)}{(1-\lambda)^{5/2}}$$

Out[72]= $$\frac{12\,d^2\pi^2\lambda^2}{5\,(1-\lambda)^{3/2}}+\frac{3\left(8-8\lambda+3\lambda^2\right)}{(1-\lambda)^{5/2}}-\frac{8\,d^4\pi^4\left(-428\left(-1+\sqrt{1-\lambda}\right)+214\left(-2+\sqrt{1-\lambda}\right)\lambda+53\lambda^2\right)}{175\sqrt{1-\lambda}}$$

Out[73]=

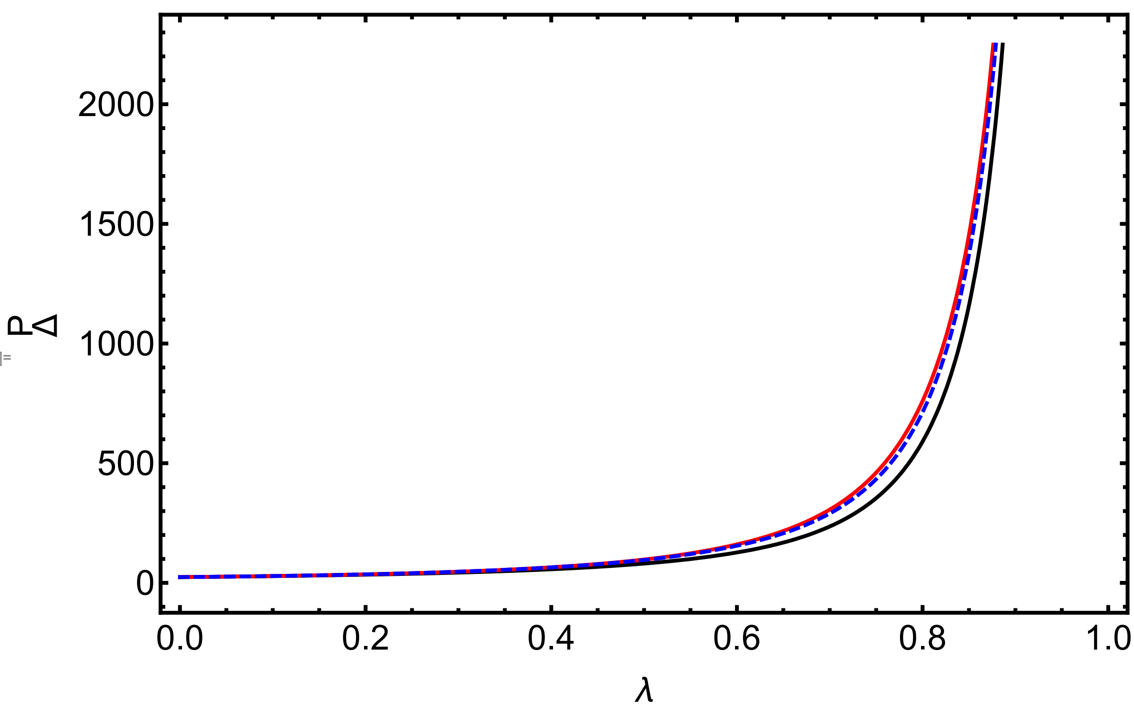

In[74]:=

```
Plot[{24/ΔP_0 /. d → 1, 24/ΔP_02 /. d → 1, 24/ΔP_024 /. d → 1},
 {λ , 0, 1}, PlotRange → {{0, 1}, {0, 1}},
 PlotStyle → {{Thick, Black}, {Thick, Red}, {Thick, Blue, Dashed}},
 FrameLabel → {"λ", "Q/Q_c"}, Frame → True,
 FrameStyle → {{Directive[Thick, Black], FontSize → 18},
   {Directive[Thick, Black], FontSize → 18}, {Directive[Thick, Black],
    FontSize → 18}, {Directive[Thick, Black], FontSize → 18}}, ImageSize → Large]
```

Out[74]=

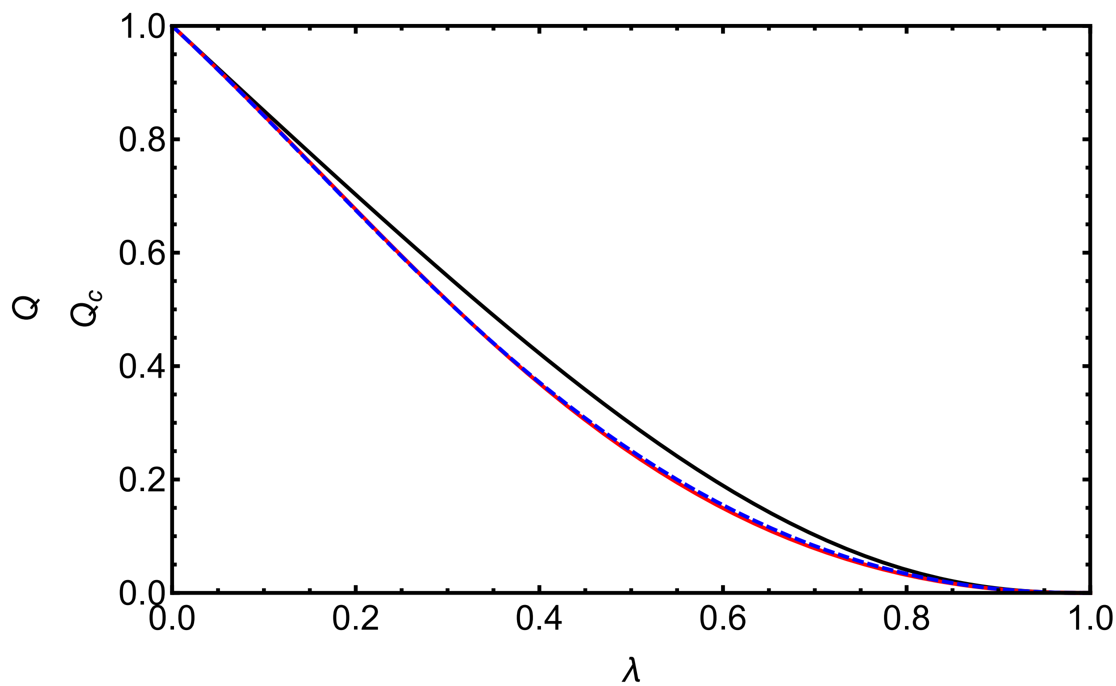

Shape function with negative λ

In[75]:=
```
Plot[{Shape /. λ → -1, Shape /. λ → -0.75, Shape /. λ → -0.50, Shape /. λ → -0.25,
  Shape /. λ → 0, Shape /. λ → 0.25, Shape /. λ → 0.5, Shape /. λ → 0.75, Shape /. λ → 1},
 {X, -1, 1}, PlotStyle → {Thickness[0.002], Thickness[0.002],
   Thickness[0.002], Thickness[0.002], Thickness[0.002], Thickness[0.002],
   Thickness[0.002], Thickness[0.002], Thickness[0.002]}, Frame → True,
 Axes → False, FrameStyle → {{Directive[Thick, Black], FontSize → 18},
   {Directive[Thick, Black], FontSize → 18}, {Directive[Thick, Black],
    FontSize → 18}, {Directive[Thick, Black], FontSize → 18}},
 FrameLabel → {"X", "Y"}, ImageSize → Large]
```

Out[75]=

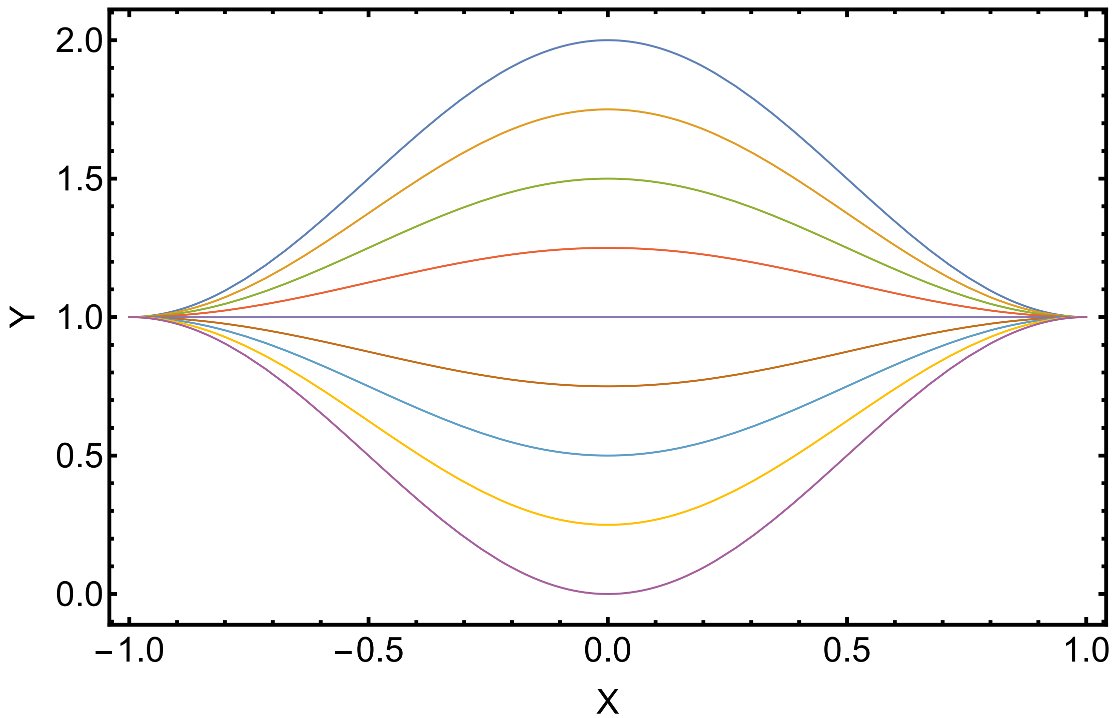

In[76]:=
```
Plot[{ΔP0 /. d → 1, ΔP02 /. d → 1, ΔP024 /. d → 1}, {λ , -1, 0},
  PlotStyle → {{Thick, Black}, {Thick, Red}, {Thick, Blue, Dashed}},
  FrameLabel → {"λ", "ΔP"}, Frame → True,
  FrameStyle → {{Directive[Thick, Black], FontSize → 18},
    {Directive[Thick, Black], FontSize → 18}, {Directive[Thick, Black],
     FontSize → 18}, {Directive[Thick, Black], FontSize → 18}}, ImageSize → Large]
```

Out[76]=

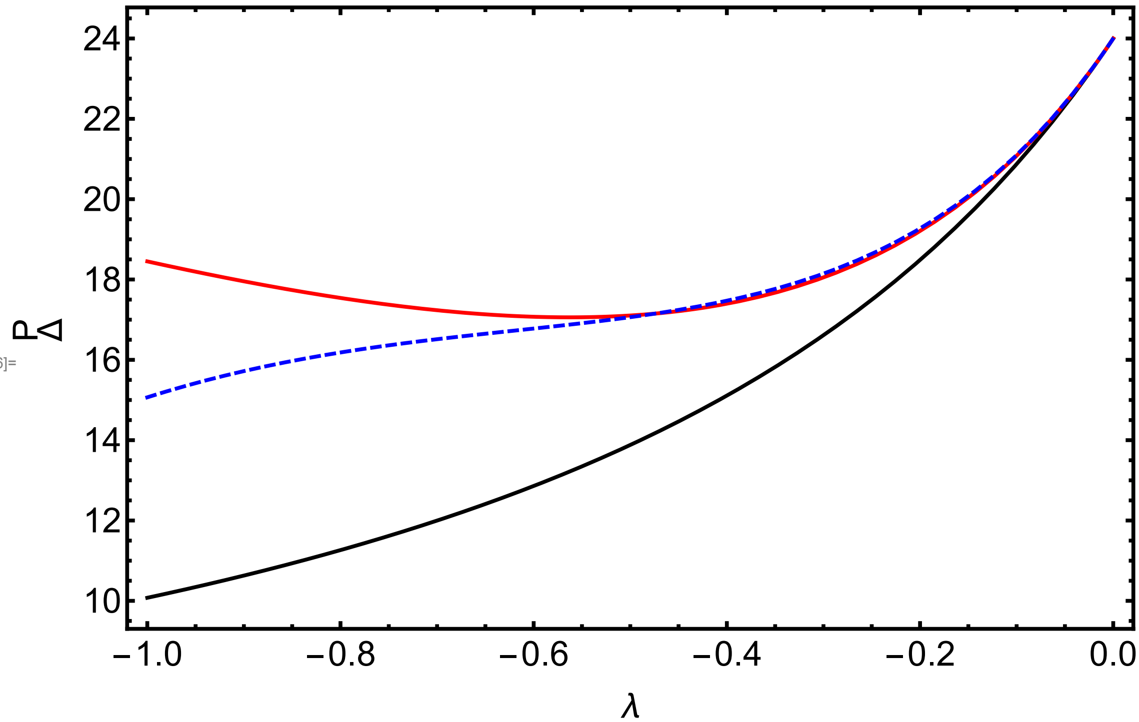

In[77]:=
```
Plot[{24/ΔP0 /. d → 1, 24/ΔP02 /. d → 1, 24/ΔP024 /. d → 1}, {λ , -1, 0},
 PlotStyle → {{Thick, Black}, {Thick, Red}, {Thick, Blue, Dashed}},
 FrameLabel → {"λ", "Q/Qc"}, Frame → True,
 FrameStyle → {{Directive[Thick, Black], FontSize → 18},
   {Directive[Thick, Black], FontSize → 18}, {Directive[Thick, Black],
    FontSize → 18}, {Directive[Thick, Black], FontSize → 18}}, ImageSize → Large]
```

Out[77]=

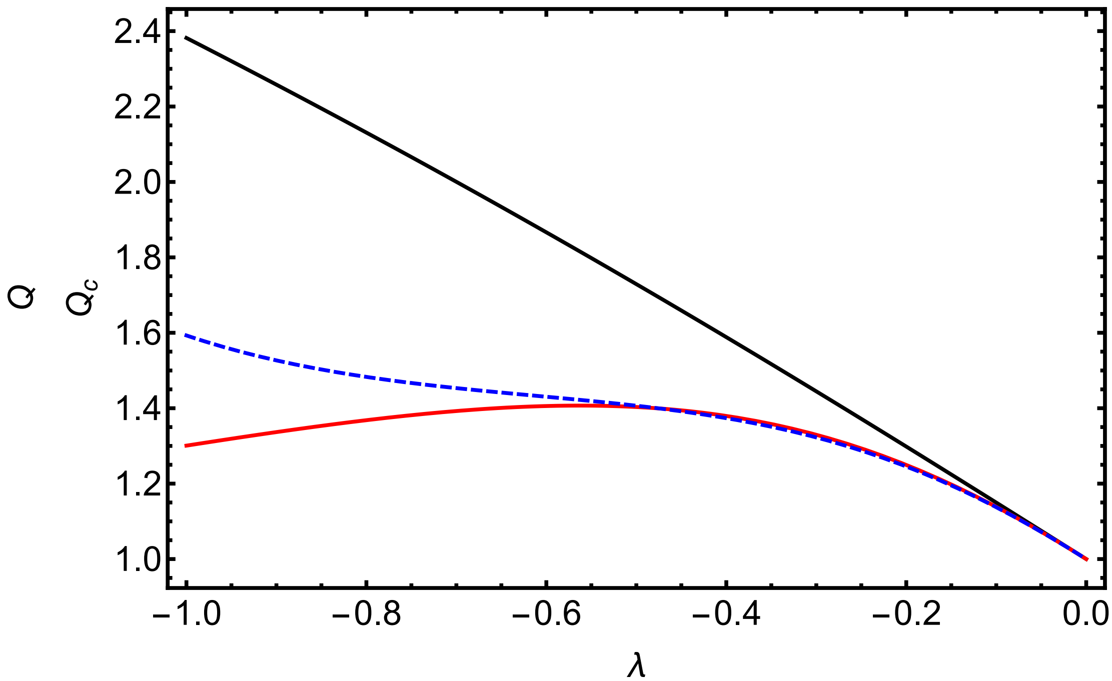

In[78]:=
```
datalistneg0 = Table[{λ , f0[λ ]}, {λ , -0.99, 0.99, 0.01}];
datalistneg02 = Table[{λ , f02[λ , 2.0], f02[λ , 1.0], f02[λ , 0.1], f02[λ , 0.01]},
   {λ , -0.99, 0.99, 0.01}];
datalistneg024 = Table[{λ , f024[λ , 2.0], f024[λ , 1.0], f024[λ , 0.1], f024[λ , 0.01]},
   {λ , -0.99, 0.99, 0.01}];
Export["datalistneg0.xlsx", datalistneg0]
Export["datalistneg02.xlsx", datalistneg02]
Export["datalistneg024.xlsx", datalistneg024]
```

Out[81]= datalistneg0.xlsx

Out[82]= datalistneg02.xlsx

Out[83]= datalistneg024.xlsx

In[84]:=
```
SystemOpen[DirectoryName[AbsoluteFileName["datalistneg024.xlsx"]]]
```